
Application of the chiral forces to electroweak processes

Vitalii Urbanevych

Ph.D. thesis written under the supervision of dr. hab Roman Skibiński
at the Jagiellonian University, Faculty of Physics, Astronomy
and Applied Computer Science, Kraków,
Sunday 26th February, 2023



CONTENTS

1	Introduction	1
2	Formalism & numerical methods	7
2.1	Deuteron bound state	7
2.2	2N scattering state	10
2.2.1	The Lippmann-Schwinger equation	10
2.3	3N bound state	12
2.4	3N scattering state	14
2.5	Photodisintegration transition amplitude for Nd state	15
2.6	Nuclear electromagnetic current	15
2.7	Theoretical uncertainties	15
3	Results	19
3.1	Deuteron photodisintegration	19
3.1.1	Cross section	19
3.1.2	Polarisation observables	26
3.2	Helium photodisintegration	40
3.2.1	3N photodisintegration	40
3.2.2	D-n photodisintegration	47
3.3	Pion absorption from the lowest atomic orbital	48
3.3.1	Pion absorption in ^3He	48
3.3.2	$\pi^- + ^3\text{H} \rightarrow n + n + n$	59

Abstract

Lorem ipsum dolor sit amet, consectetur adipiscing elit, sed do eiusmod tempor incididunt ut labore et dolore magna aliqua. Ut enim ad minim veniam, quis nostrud exercitation ullamco laboris nisi ut aliquip ex ea commodo consequat. Duis aute irure dolor in reprehenderit in voluptate velit esse cillum dolore eu fugiat nulla pariatur. Excepteur sint occaecat cupidatat non proident, sunt in culpa qui officia deserunt mollit anim id est laborum.

CHAPTER 1

INTRODUCTION

Why we study few nucleon systems

The study of light nuclei and their reactions for the decades has been serving as an easiest way to investigate particles in nuclei and forces between them. Convenient way to proceed may be to study an interaction of nucleus with other nucleus, particles or electromagnetic probes as electrons photons, muons, pions, neutrinos, hyperions etc. In most cases study of elastic or inelastic scattering is possible. Whis can be done both theoretically or by performing relevant experiments to test if theory works. People take into account that interactions may be caused by different forces and therefore should be described in different ways. It can be either strong, weak or electromagnetic interaction. It depends on the type of particle being scattered and the target which reaction it is.

In past many experimental efforts have been undertaken and electromagnetic reactions in light nuclei have been a point of interest for experimentalists for decades. There are experimental data from the second half of XX century (e.g. [?], [?], [?], [?]) which is still useful when it comes to checking theory with results of measurements. There are a number of facilities providing a source of gamma rays (both low- and high-energetic) and other particles which have been operating over decades and still allow to perform experiments. There are among other such groups and collaborations as TUNL [?], MAMI [?], NIKHEF [?], HI γ S [?] and others. In order to describe the nuclear reactions properly many components should be taken into account. The most important are nucleon interactions and nuclear current. First of all, different forces may act on the participants.

The strong nuclear force appear inside the nuclei and, among others, bound neutrons and protons together. The description of strong interactions is extremely difficult as it deals not only with nucleon, but with their constituents: quarks and gluons. Quantum chromodynamics (QCD) is a modern theory describing strong interactions, but, at the moment, it is not applicable at low energies ($Q^2 \lesssim 1\text{GeV}^2$). In our situation various approaches are coming into the scene. The most advanced are chiral effective theory, lattice calculation and others [?], [?], [?].

Starting the study of three- (and more) nucleon systems it was found that strong 2N force is not enough to describe the system and 3N force was introduced. The first applications of such a force showed that it brings sufficient contribution and cannot be ignored [?]. Contribution of the 3NF can be examined comparing binding energies of light nuclei calculated with and without this part with respect to experimental values. For

example, binding energy for ${}^3\text{H}$ calculated with Argonne V18 (AV18) potential without 3NF gives $E_b({}^3\text{H}) = -7.628 \text{ MeV}$ [?]. There are different models that might add a 3NF contribution to AV18 (or other potential). Using the Tucson-Melbourne(TM) model [?] results in $E_b({}^3\text{H}) = -8.478 \text{ MeV}$ and Urbana IX [?] 3NF provide us with $E_b({}^3\text{H}) = -8.484 \text{ MeV}$. Looking at the experimental value $E_b({}^3\text{H}) = -8.482 \text{ MeV}$, it is clear that 3NF contribution makes prediction much closer to the measurement. Nevertheless the Urbana IX 3NF in this case was fitted by the experimental value for ${}^3\text{H}$ so there is no surprise in good agreement. One can check the binding energy for other atoms, which were not used for fitting. The 2NF binding energy for ${}^3\text{He}$ (calculated with AV18) is $E_b({}^3\text{He}) = -6.917 \text{ MeV}$, TM contribution makes it $E_b({}^3\text{He}) = -7.706 \text{ MeV}$, Urbana IX - $E_b({}^3\text{He}) = -7.739 \text{ MeV}$, while experimental value is $E_b({}^3\text{He}) = -7.718 \text{ MeV}$. Once more we can see the importance of 3NF contribution on the α -particle's (${}^4\text{He}$) binding energy: pure AV18 gives $E_b({}^4\text{He}) = -24.25 \text{ MeV}$, AV18 + TM - -28.84 MeV , AV18 + Urbana IX - -28.50 MeV and experimental value is -28.30 MeV .

Whereas the first applications included only early simplified "realistic" 3N potential, the latter investigations, based on more advanced models, only confirmed this statements [?, ?]. It was also used to construct four-nucleon (4N) bound state [?].

Electromagnetic force appears between charged particles like protons, electrons or pions. Also, the force is transferred between charged particles and a photon, so in photon- and electron- scatterings on the nuclei an electromagnetic force is necessary component of a description. Arenhövel [?] studied electromagnetic process - deuteron photodisintegration, applying different approaches and comparing the results with experimental data.

The weak force...

...

Models of strong interaction used in the thesis

In order to model the nuclear potential, physicists often use phenomenological or semi-phenomenological approaches. It allows them to combine theoretical knowledge about processes and experimental data.

One of such models, which was used in current thesis is the Argonne V18 (AV18) [?]. In order to construct nucleon-nucleon (NN) force, authors combine one-pion-exchange parts with phenomenological one and supplement them by electromagnetic corrections. Free parameters were fitted to the Nijmegen partial-wave analysis of pp and np data [?]. Authors showed, that AV18 potential delivers good results in the description of nucleon scattering data ($\chi^2/data = 1.08$ for around 4000 pp and np scattering datasets) as well as deuteron properties (estimated binding energy is $2.2247(35) \text{ MeV}$ vs experimental $2.224575(9) \text{ MeV}$).

In the early 1990-ies Weinberg [?, ?] introduced an idea of using the most general Lagrangian satisfying assumed symmetry principles and in particular spontaneously broken chiral symmetry to describe nuclear interactions at low energies. This idea together with effective field theory (EFT) of QCD led to the development of the Chiral Effective Field Theory (χEFT) which nowadays has become one of the most advanced approach to low-energy nuclear physics. While in χEFT it is possible to study processes or bound states directly, it is also possible to describe nuclear potential, which can be next used in quantum equations, e.g. Schrödinger equation.

For the EFT it is very important to define a quantity, which powers will determine a

perturbation order. In the χ EFT there are two natural scales: so-called soft scale $Q \sim M_\pi$ - the mass of pion and the hard scale - $\Lambda_\chi \sim 0.7 \text{ GeV}$ - chiral symmetry breaking scale. The ratio between these two scales Q/Λ_χ is being used as an expansion parameter in χ EFT with power ν : $(Q/\Lambda_\chi)^\nu$.¹

Possibility of deriving nuclear potential is an important feature of χ EFT. The potential, as occurs in an Lagrangian, is a perturbation expression of the same parameter Q/Λ_χ . Considering so-called irreducible diagrams (which cannot be split by cutting nucleon lines), Weinberg [?, ?] came to the expression for the powers ν_W of such diagrams

$$\nu_W = 4 - A - 2C + 2L + \sum_i \Delta_i, \quad (1.1)$$

where i specifies a vertex number and

$$\Delta_i \equiv d_i + \frac{n_i}{2} - 2. \quad (1.2)$$

In Eq. (1.1), C is a number of pieces which are connected, L - the number of loops in the graph and A is a number of nucleons in the diagram. In Eq. (1.2), n_i is a number of nucleon field operators, d_i - the number of insertions (or derivatives) of M_π .

The further analysis of Eq. (1.1) revealed some problems which occur for particular values of parameters in the equation, namely negative values of ν_W are possible while the order has to take integer values from 0 to infinity. In order to deal with that, Eq. (1.1) was slightly modified adding $3A - 6$ to it [?, ?]:

$$\nu = \nu_W + 3A - 6 = -2 + 2A - 2C + 2L + \sum_i \Delta_i \quad (1.3)$$

In χ EFT the first order, "leading order" (LO, $\nu = 0$) is followed by next-to-leading order (NLO, $\nu = 2$)², next-to-next-to-leading order (next-to-next-to-leading order (N²LO), $\nu = 3$) and so on. At each chiral order, new interaction diagrams complete the potential. At LO there is a diagram which consists of 2 contact terms and the diagram implying one-pion exchange. Both diagrams reflect only 2NF as well as diagrams at NLO, where more contact terms are introduced together with two-pion exchange topologies. Each subsequent order includes more and more sophisticated diagrams describing nucleons interaction via multiple pion exchanges and various contact vertexes. 3NF appears at N²LO while 4NF contributions are occurring at next-to-next-to-next-to-leading order (N³LO). This establishes for the first time a systematic way to include all the forces from the simplest diagrams at LO and gradually adding more and more terms. It is also beneficial in the way that one can obtain results using chiral potential at different orders and track which one gives larger or smaller contribution to the final prediction. The highest order for which there is a derived term in potential is next-to-next-to-next-to-next-to-leading order (N⁴LO) at the moment. Nevertheless leading F-wave contact interactions from N⁵LO are included in the next-to-next-to-next-to-next-to-leading order plus contributions from following order (N⁴LO⁺) potential, which is currently regarded as a best possible potential within the model. The progression of the chiral orders is reflected in a χ^2/datum . Leading order has only $\chi^2/\text{datum} = 73$ (with neutron-proton data with

¹Note that exact values of some parameters are still under discussion [?]. We follow here approach described by E.Epelbaum and collaborators, see e.g. [?]

²The $\nu = 1$ order is completely vanished due to parity and time-reversal invariance, so next-to-leading order stands for the second order of expansion.

$E_{lab} = 0 - 100\text{MeV}$). Each subsequent order has better and better results: NLO has $\chi^2/datum = 2.2$, $N^2\text{LO} - \chi^2/datum = 2.2$ and the final $N^4\text{LO}^+$ has $\chi^2/datum = 1.08$ [?]. Similar progression is observed for larger energies, e.g for $E_{lab} = 0 - 300\text{MeV}$ $\chi^2/datum$ is 75, 14, 4.2, 2.01, 1.16 and 1.06 at LO, NLO, $N^2\text{LO}$, $N^3\text{LO}$, $N^4\text{LO}$ and $N^4\text{LO}^+$ respectively. The proton-proton data description has similar trend, so $\chi^2/datum$ is 1380, 91, 41, 3.43, 1.67, 1.00 for the same energy bin and chiral orders. At $N^4\text{LO}^+$ $\chi^2/datum$ for proton-proton data stands similar value (close to 1) as for neutron-proton, but the convergence comes a bit later and leading order has way worse description. In my work I will use chiral potentials from LO to $N^4\text{LO}^+$.

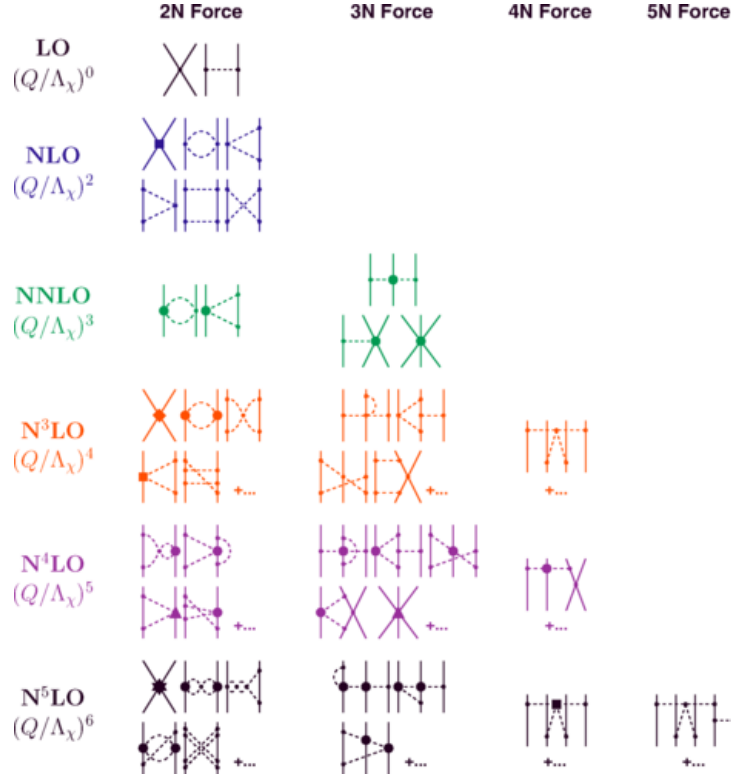


Figure 1.1: *Make own diagrams, e.g. with JaxoDraw or PyFeyn [?]*

The general scheme outlined above was developed mainly by the Bochum-Bonn and Moscow-Idaho groups. Both groups have similar approaches and were independently and almost simultaneously developing own chiral potentials. In 1998 Epelbaum and colleagues from Bochum-Bonn group presented a first version of their NN chiral potential [?, ?]. Developing a more and more sophisticated versions with higher chiral orders, authors presented $N^3\text{LO}$ potential in 2005 [?] which included a 3NF contributions. Authors were further developing their model, taking into account more Feynmann diagrams coming to a higher chiral orders. Another problem Bochum-Bonn group faced with was a potential regularization. An important point was when authors started using a semi-local regularisation in the coordinate space (semilocal coordinate-space regularized (SCS) potential) [?] and later similar regularisation, but in the momentum space, resulting in a most advanced chiral potential at the moment up to $N^4\text{LO}^+$ chiral order [?] (the semilocal momentum-space regularized (SMS) potential).

On the other side of the planet, in Idaho, Machleidt and his group from Moscow were also developing a chiral potential. Their results from 2003 [?], following with later

investigations [?, ?, ?] were introducing very similar to Bochum-Bonn model with minor technical differences.

There are a number of another approaches within χ EFT utilized. The group of Piarulli is using quite similar approach, including the same chiral potentials with minor differences [?, ?].

Machleidt, Ekström, pion-less EFT, Lattice EFT(Mesissner), Girlanda, Piarulli

Technically the chiral potential may be derived both in coordinate and momentum spaces. Nevertheless in both cases it requires regularization which cuts low coordinate values in order to avoid infinities (or high momentum values - in momentum space). The SMS potential is being regularized semilocally. It means that in its pion propagators both local and nonlocal regularizations are being applied for different parts of the potential. In [?, ?] and later in [?, ?] the non-local regularisator was applied to both short- and long-range parts of the potential. This regularization is applied directly to the potential matrix elements in the coordinate space:

$$V_\pi(\vec{r}) \rightarrow V_{\pi,R}(\vec{r}) = V_\pi(\vec{r}) (1 - \exp(-r^2/R^2)), \quad (1.4)$$

where the cutoff R was chosen in the range of $R = 0.8, \dots, 1.2$ fm.

In the current work the potential from [?] is mainly regarded. In this potential, regularization is being applied in the momentum space:

$$V_\pi(\vec{p}', \vec{p}) \rightarrow V_\Lambda(\vec{p}', \vec{p}) = V_\pi(\vec{p}', \vec{p}) \exp \left[-(p'/\Lambda)^{2n} - (p/\Lambda)^{2n} \right], \quad (1.5)$$

with $\Lambda = \frac{2}{R}$ and n being adjusted with respect to the considered chiral order.

The other part of regularization, local, is applied to the propagator operator, during the derivation of potential. Namely, the Gaussian form factor $F(\vec{l}^2)$ is being used :

$$\int_{-\infty}^{\infty} \frac{\rho(\mu^2)}{\vec{l}^2 + \mu^2} d\mu^2 \rightarrow \frac{F(\vec{l}^2)}{\vec{l}^2 + \mu^2} \quad (1.6)$$

with

$$F(\vec{l}^2) = e^{-\frac{\vec{l}^2 + M_\pi^2}{\Lambda^2}}, \quad (1.7)$$

where M_π is an effective pion mass and Λ - is a cutoff parameter and l is a four-momentum of the exchanged pion. The form factor from Eq. (1.7), being used together with Feynman propagator, ensures that long-range part of the forces has no singularities.

The cut-off parameter Λ is not fixed and usually calculations are being performed with different values. The comparison of such results may reveal stronger or weaker dependance and in perfect case, which is expected at $\nu \gg 1$, one will come up with such a potential, were the cut will not affect results at all. One of aims of my thesis is to test how big cut-off dependency of predictions is observed for currently available forces. In Fig. 1.2 I show values of the matrix elements for 2N potential $\langle \vec{p} | V | \vec{p}' \rangle$ as a function on the momentum $|\vec{p}|$ with fixed value $|\vec{p}'| = 0.054 \text{ fm}^{-1}$.

The potential may be transformed from coordinate to momentum space (or vice versa), but it is important at which frame the regularization was performed and what was a regularization function. That's why there are different versions of chiral potential. One is the SCS potential [?] and another one is similar, but with regularization applied in momentum space (SMS potential) [?].

Yet another regularisation function is used by R. Machleidt, D.R. Entem and A. Nogga,

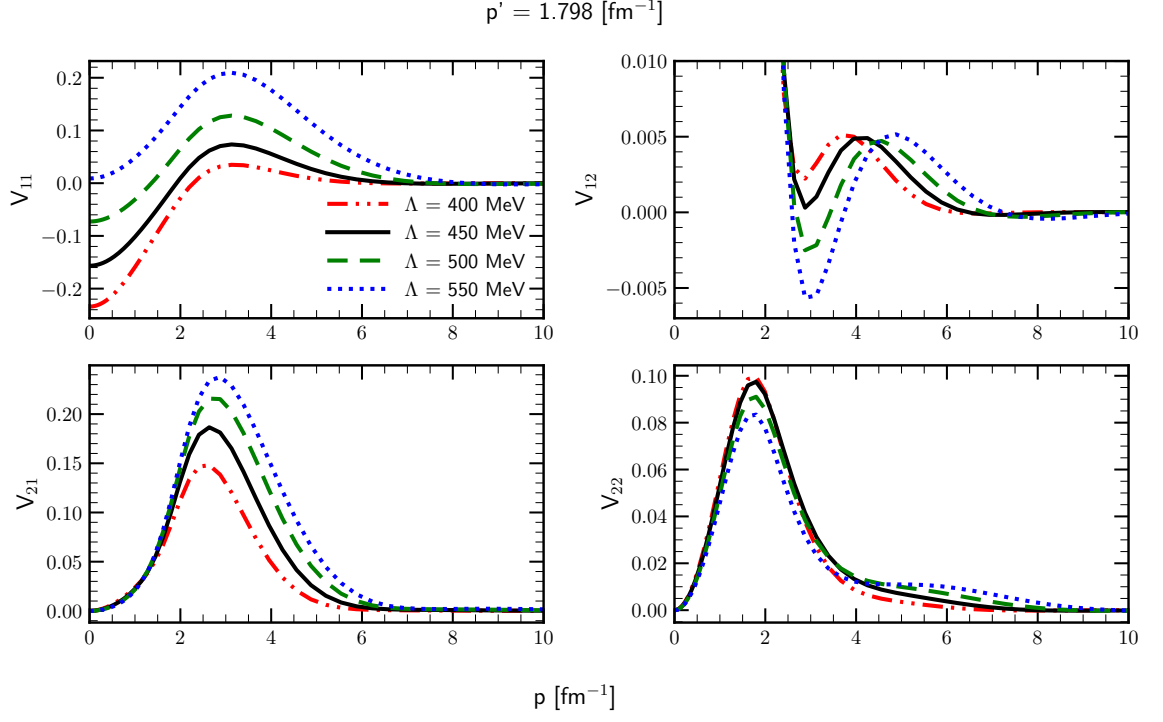


Figure 1.2: Potential components in case of coupled partial waves $3S_1 - 3D_1$ as a function on the momentum p with fixed value of the momentum $p' = 1.798 \text{ fm}^{-1}$.

when regulating matrix elements of the potential in momentum space with non-local regulator only.

Currents

CHAPTER 2

FORMALISM & NUMERICAL METHODS

Despite the deuteron problem was solved long time ago, I will describe it briefly in order to introduce the notation and formalism. With that, for more complex 3N case only slight extension will be needed.

In order to calculate any observable for the deuteron photodisintegration, one has to find a nuclear matrix elements:

$$N^\mu = \langle \Psi_{final} | J^\mu | \Psi_{internal} \rangle, \quad (2.1)$$

with $\Psi_{internal} = \Psi_{deuteron}$ and J^μ is a four-vector current operator which acts between initial and final two-nucleon states.

2.1 Deuteron bound state

Let's find a deuteron bound state wave function $|\phi_d\rangle$. The time-independent Schrödinger equation for two particles exposes as:

$$(H_0 + V) |\phi_d\rangle = E_d |\phi_d\rangle, \quad (2.2)$$

with a kinetic energy H_0 and potential V . The kinetic energy H_0 can be represented in terms of relative and total momenta of the particles:

$$H_0 = \frac{\vec{p}_1^2}{2m_1} + \frac{\vec{p}_2^2}{2m_2} = \frac{\vec{p}^2}{2\mu} + \frac{\vec{P}^2}{2M}, \quad (2.3)$$

where relative and total momenta are defined as follows:

$$\vec{p} = \frac{(m_1 \vec{p}_1 - m_2 \vec{p}_2)}{m_1 + m_2} \quad (2.4)$$

$$\vec{P} = \vec{p}_1 + \vec{p}_2 \quad (2.5)$$

and $M = m_1 + m_2$ is a total mass, $\mu = \frac{m_1 m_2}{M}$ is a relative mass of two nucleons, \vec{p}_i is a momentum of i-th particle.

Potential V is assumed to depend on the relative degrees of freedom, so Eq. (2.2) may be decomposed into two separated equations:

$$\frac{\vec{p}^2}{2\mu} \langle \vec{p} | \Psi_{int} \rangle + \langle \vec{p} | V | \Psi_{int} \rangle = (E_d - E_{c.m.}) \langle \vec{p} | \Psi_{int} \rangle \quad (2.6)$$

$$\frac{\vec{P}^2}{2M} \langle \mathcal{P} | \Psi_{c.m.} \rangle = E_{c.m.} \langle \mathcal{P} | \Psi_{c.m.} \rangle, \quad (2.7)$$

with $\langle \vec{p}, \vec{\mathcal{P}} | H_0 | \phi_d \rangle = \frac{\vec{p}^2}{2\mu} \langle \vec{p} | \Psi_{int} \rangle + \frac{\vec{P}^2}{2M} \langle \mathcal{P} | \Psi_{c.m.} \rangle$. So $\Psi_{c.m.}$ is a component of total wave function, which reflects a deuteron as a single object with momentum \vec{P} while Ψ_{int} is an internal wave function describing interaction between nucleons. Basis state $|\vec{p}\rangle$ obeys a completeness equation:

$$\int d^3\vec{p} |\vec{p}\rangle \langle \vec{p}| = \mathbb{1} \quad (2.8)$$

Eq.(2.6) is basically a Schrödinger equation for one particle with mass μ in potential V and Eq.(2.7) can be regarded as a Schrödinger equation for particle with mass M in a free motion. Assuming that deuteron is at rest ($E_{c.m.} = 0$) we can stick to the Eq.(2.6) only. Using completeness relation 2.8 we get:

$$\frac{\vec{p}^2}{2\mu} \langle \vec{p} | \Psi_{int} \rangle + \int d\vec{p}' \langle \vec{p} | V | \vec{p}' \rangle \langle \vec{p}' | \Psi_{int} \rangle = E_d \langle \vec{p} | \Psi_{int} \rangle \quad (2.9)$$

Working in 3 dimensional space is difficult (especially numerically) so I follow a standard path and introduce the partial-wave representation (PWD) of the momentum state, adding spin and isospin degrees of freedom in the following form:

$$|p\alpha\rangle \equiv |p(ls)jm_j\rangle |tm_t\rangle, \quad (2.10)$$

where quantum numbers l, s, j, t are orbital angular momentum, total spin, total angular momentum and total isospin respectively. m_j and m_t are total angular isospin momentum and isospin projections, respectively.

States $|p(ls)jm_j\rangle$ can be further decomposed to simpler states than it is in (2.10), separating spin part as

$$|p(ls)jm_j\rangle = \sum_{m_l} c(ls j; m_l, m_j - m_l, m_j) |plm_l\rangle |s m_j - m_l\rangle. \quad (2.11)$$

Spin(isospin) states can be represented via single-nucleon spin(isospin) states:

$$|sm_s\rangle = \sum_{m_1} c(\frac{1}{2} \frac{1}{2} s; m_1, m_s - m_1, m_s) \left| \frac{1}{2} m_1 \right\rangle \left| \frac{1}{2} m_s - m_1 \right\rangle, \quad (2.12)$$

$$|tm_t\rangle = \sum_{\nu_1} c(\frac{1}{2} \frac{1}{2} t; \nu_1, m_t - \nu_1, m_t) \left| \frac{1}{2} \nu_1 \right\rangle \left| \frac{1}{2} m_t - \nu_1 \right\rangle. \quad (2.13)$$

In Eqs.(2.11) -(2.13), $c(\dots)$ are Clebsh-Gordon coefficients. Nucleons are spin $\frac{1}{2}$ particles, and also we treat proton and neutron as the same particle in different isospin states, so that isospin is $\nu_1 = \frac{1}{2}$ for proton and $\nu_1 = -\frac{1}{2}$ for neutron.

The states $|plm_l\rangle$ from Eq.(2.11) are orthogonal, so that

$$\langle p'l'm'_l | plm_l \rangle = \frac{\delta(p - p')}{p^2} \delta_{ll'} \delta_{m_l m'_l} \quad (2.14)$$

and also satisfy the completeness relation:

$$\sum_{l=0}^{\infty} \sum_{m_l=-l}^l \int dp p^2 |plm_l\rangle \langle plm_l| = \mathbb{1} \quad (2.15)$$

Projection of $\langle \vec{p}' |$ states to $|plm_l\rangle$ leads to

$$\langle \vec{p}' | plm_l \rangle = \frac{\delta(|\vec{p}'| - p)}{p^2} Y_{lm_l}(\hat{p}'), \quad (2.16)$$

where $Y_{lm_l}(\hat{p}')$ is a spherical harmonic and 'hat' denotes a unit vector in direction of \vec{p} :

$$\vec{p} \equiv |\vec{p}| \hat{p} \equiv p \hat{p}. \quad (2.17)$$

Nucleons are fermions so exchanging them leads to antisymmetry of the wave function. In PWD it results in additional requirement on quantum numbers which is:

$$(-1)^{l+s+t} = -1. \quad (2.18)$$

In general, nuclear NN force conserves spin and parity so

$$\langle p' \alpha' | V | p \alpha \rangle = \delta_{jj'} \delta_{mm'} \delta_{tt'} \delta_{m_t m_{t'}} \delta_{ss'} V_{ll'}^{sjtm_t}(p', p) \quad (2.19)$$

which introduces restrictions for particular sets of quantum numbers. The channels, where $l \neq l'$ are coupled and for the deuteron bound state one can find only one possible PWD state combination: two coupled channels which are commonly denoted as 3S_1 and 3D_1 (the naming stands for ${}^{2s+1}l_j$). They correspond to $l = 0$ and $l = 2$ respectively (with $s = j = 1$ and $t = m_t = 0$). We will call wave functions for these channels as $\phi_l(p)$ with $l = 0, 2$, such that:

$$\phi_l(p) = \langle p(ls)jm_j | \langle tm_t | \Psi_{int} \rangle = \langle p(l1)1m_d | \langle 00 | \Psi_{int} \rangle; l = 0, 2. \quad (2.20)$$

So with a new basis Eq.(2.9) takes a form:

$$\frac{\vec{p}^2}{2\mu} \phi_l(p) + \sum_{l'=0,2} \int dp' p'^2 \langle p(l1)1m_d | \langle 00 | V | 00 \rangle | p'(l'1)1m_d \rangle \phi_{l'}(p') = E_d \phi_l(p), \quad (2.21)$$

for $l = 0, 2$. In case one does not have a matrix elements for the potential $\langle plm_l | V | p'l'm_l' \rangle$ in analytical form, but only values for some grid of points, there is still one complication in the Eq.(2.21) - integration, which has to be discretized. In order to get rid of the integral I use a Gaussian quadrature method of numerical integration [?]. It allows to replace an integral by the weighted sum: $\int_a^b f(x) dx = \sum_{i=1}^n \omega_i f(x_i)$ In current work I used $N = 72$ points in the interval from 0 to 50 fm^{-1} . Using this method, Eq.(2.21) becomes

$$\frac{p_i^2}{2\mu} \phi_l(p_i) + \sum_{l'=0,2} \sum_{j=0}^{N_P} \omega_j p_j^2 \langle p_i(l1)1m_d | \langle 00 | V | 00 \rangle | p_j(l'1)1m_d \rangle \phi_{l'}(p_j) = E_d \phi_l(p_i). \quad (2.22)$$

In practical computations, the same grid points p_i and p_j are used in order optimize computational time. I solve this equation as an eigenvalue problem $M\Psi = E_d\Psi$ and

in that way find simultaneously wave function values in grid of p points and binding energy E_d . The binding energy E_d calculated with potentials of different chiral orders is presented on the Fig. 2.1.

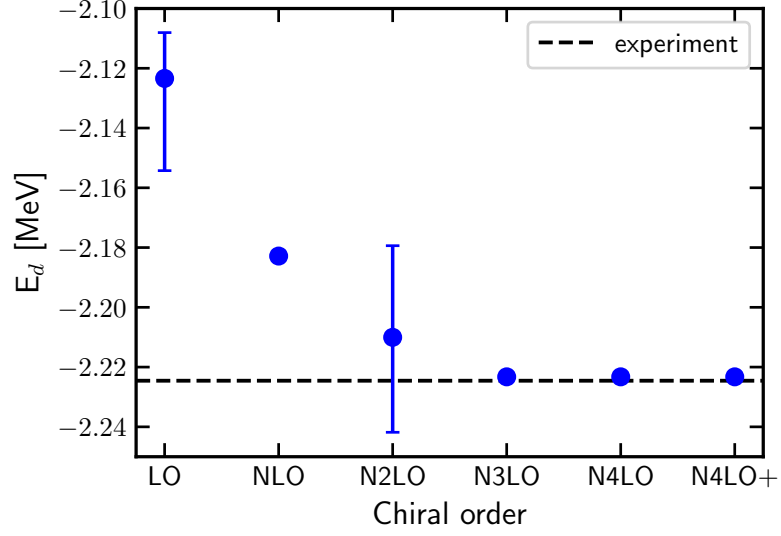


Figure 2.1: Deuteron binding energy calculated using chiral potential with different chiral orders as a mean value over all cutoffs. Error bands represent a spread the calculated binding energy with respect to the cutoff parameter Λ (minimal and maximal values). Experimental data is taken from [?]

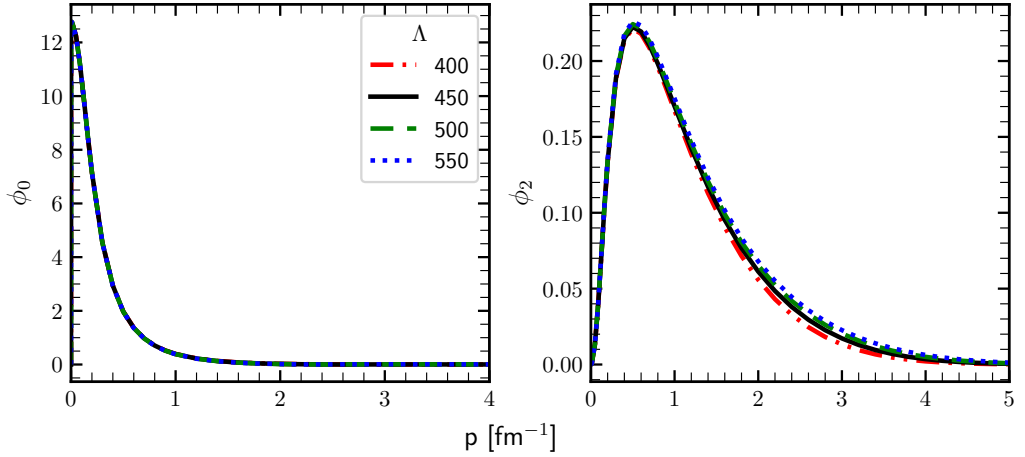


Figure 2.2: Wave function ϕ_l for $l=0$ ($3S_1$ partial wave) - left figure and $l=2$ ($3D_1$) - right figure.

2.2 2N scattering state

2.2.1 The Lippmann-Schwinger equation

Let us start from the time-independent formulation of the scattering process. In such a case Hamiltonian is:

$$H = H_0 + V, \quad (2.23)$$

where again H_0 is a kinetic energy operator $H_0 = \frac{p^2}{2m}$ and V is a nucleon-nucleon interaction. For a free particle motion, V will be absent and we will denote an energy eigenstate as $|\vec{p}_0\rangle$ - a free particle state. The scattering state $|\psi\rangle$ fulfills similar Schrödinger equation as $|\vec{p}_0\rangle$, with the same energy eigenvalue, but with potential presented:

$$\begin{cases} H_0 |\vec{p}\rangle &= E |\vec{p}\rangle \\ (H_0 + V) |\psi\rangle &= E |\psi\rangle \end{cases} \quad (2.24)$$

We are interested in solution for Eq. (2.24), so that $|\psi\rangle \rightarrow |\vec{p}\rangle$ as $V \rightarrow 0$ and both $|\psi\rangle$ and $|\vec{p}\rangle$ have the same energy eigenvalues E . As we have scattering process, the energy spectra for both operators H_0 and $H_0 + V$ are continuous.

From Eq. (2.24) follows that

$$|\psi\rangle = \frac{1}{E - H_0} V |\psi\rangle + |\vec{p}\rangle, \quad (2.25)$$

which guarantees that application of the operator $(E - H_0)$ to the (2.25) results in the second equation from the system (2.24).

In order to deal with a singular operator $\frac{1}{E - H_0}$ in Eq. (2.25), the well-known technique is to make such an operator complex by adding small imaginary number to the denominator so Eq.(2.25) becomes

$$|\psi\rangle = G_0(E \pm i\epsilon) V |\psi\rangle + |\vec{p}\rangle, \quad (2.26)$$

where G_0 is a free propagator:

$$G_0(z) = \frac{1}{z - H_0} \quad (2.27)$$

Solution with $G_0(E - i\epsilon)$ corresponds to the incoming spherical wave, while $G_0(E + i\epsilon)$ - to the outgoing one. Since we are interested in the scattering process, only the (+) sign survives.

Eq. (2.26) is known as the Lippmann-Schwinger equation (LSE) and defining the transition operator t :

$$t |\vec{p}\rangle = V |\psi\rangle \quad (2.28)$$

we can rewrite it as

$$|\psi\rangle = (1 + G_0(E + i\epsilon)t) |\vec{p}\rangle \quad (2.29)$$

With substitution of Eq. (2.26) into Eq. (2.28) we can find an explicit form of the t operator:

$$\begin{aligned} t |\vec{p}\rangle &= V G_0(E + i\epsilon) V |\psi\rangle + V |\vec{p}\rangle = \\ &= V G_0(E + i\epsilon) t |\vec{p}\rangle + V |\vec{p}\rangle \end{aligned} \quad (2.30)$$

Getting rid off the initial state $|\vec{p}\rangle$ in the Eq. (2.30) we can get a LSE for the transition operator in the iterative form:

$$\begin{aligned}
 t &= V + VG_0t = \\
 &= V + VG_0V + VG_0VG_0V + \dots,
 \end{aligned} \tag{2.31}$$

which constitutes an infinite series of subsequent NN interactions and free propagator of nucleons.

In the partial-wave representation, LSE Eq. (2.30) expresses as:

$$\begin{aligned}
 \langle p'(l's')j'm_{j'} | \langle t'm_{t'} | t(E) | tm_t \rangle | p(ls)jm_j \rangle &= \langle p'(l's')j'm_{j'} | \langle t'm_{t'} | V | tm_t \rangle | p(ls)jm_j \rangle + \\
 &+ \sum_{\alpha''} \int_0^\infty dp'' p''^2 \langle p'(l's')j'm_{j'} | \langle t'm_{t'} | V | t''m_{t''} \rangle | p''(l''s'')j''m_{j''} \rangle \\
 &\times \frac{1}{E + i\epsilon - p''^2/m} \langle p''(l''s'')j''m_{j''} | \langle t''m_{t''} | t(E) | tm_t \rangle | p(ls)jm_j \rangle, \tag{2.32}
 \end{aligned}$$

which after using symmetries of potential matrix elements reduces to

$$\begin{aligned}
 \langle p'(l's')jt | t(E) | p(ls)jt \rangle &= \langle p'(l's')jt | V | p(ls)jt \rangle + \\
 &+ \sum_{l''} \int_0^\infty dp'' p''^2 \langle p'(l's')jt | V | p''(l''s)jt \rangle \\
 &\times \frac{1}{E + i\epsilon - p''^2/m} \langle p''(l''s)jt | t(E) | p(ls)jt \rangle. \tag{2.33}
 \end{aligned}$$

Using Eq. (2.29) we can write Eq. (2.1) as

$$N^\mu = \langle \phi m_p m_n | (1 + G_0(E + i\epsilon)t) \frac{1}{e} J^\mu(0) | \Psi_i \vec{P}_i \rangle \tag{2.34}$$

2.3 3N bound state

The 3N bound state is described by the Schrödinger equation for 3N system and its total wave function obeys the following equation:

$$|\Psi\rangle = G_0(E + i\epsilon) \sum_{j=1}^3 (V_j + V_4^j) |\Psi\rangle, \tag{2.35}$$

where G_0 is a free propagator from Eq. (2.27), V_j - is a two-body potential acting between nucleons k and l (j, k and l - numerate nucleons, $j, k, l \in 1, 2, 3$ and $j \neq k \neq l$) and V_4^j is a component of three-body potential $V_4 = \sum_{j=1}^3 V_4^j$ symmetrical under exchange of nucleons k and l , E - is a binding energy.

Eq. (2.35) can be split into 3 independent equations for so-called Faddeev components $|\psi_j\rangle$

$$|\Psi\rangle = \sum_{j=1}^3 |\psi_j\rangle, \tag{2.36}$$

which fulfills separately

$$|\psi_j\rangle = G_0(E + i\epsilon)(V_j + V_4^j) |\Psi\rangle. \quad (2.37)$$

Next, I introduce a permutation operator P , which is a combination of operators P_{jk} :

$$P = P_{12}P_{23} + P_{13}P_{32}. \quad (2.38)$$

The operator component P_{jk} acting on the state interchange the momenta and quantum numbers of the nucleons j and k .

Using definitions 2.38 and 2.36, one can rewrite Eq. (2.37) as:

$$|\psi_j\rangle = G_0(E + i\epsilon)t_j P |\psi_j\rangle + (1 + G_0(E + i\epsilon)t_j)G_0(E + i\epsilon)V_4^j(1 + P) |\psi_j\rangle, \quad (2.39)$$

where t_j is a two-body t-operator which obeys Eq. (2.30) for corresponding two-body potential V_j .

The partial wave representation of the Eq. (2.39) is obtained using following states:

$$|p, q, \alpha_{J, M_J}\rangle = \left| p, q, (ls)j, (\lambda, \frac{1}{2})I(jI)JM; (t\frac{1}{2})TM_T \right\rangle_1, \quad (2.40)$$

where index 1 states the choice of the Jakobi momenta, such that p is a relative momentum of the nucleons 2 and 3. Values l , s and j are quantum numbers in the two-body subsystem consisted of nucleons 2 and 3. λ is the orbital angular momentum of the first particle which spin is $\frac{1}{2}$ and total angular momentum I . J and M_J are the total angular momentum of the 3N system and its projection on the z-axis respectively. y is a total isospin of the 2-3 subsystem whereas T and MT are the total isospin of the 3N system and its projection on the z-axis.

Using states defined in Eq. (2.40), we can write a partial-wave representation of the

Eq. (2.39):

$$\begin{aligned}
 \langle p, q, \alpha_{J,M_J} | \psi_i \rangle = & \frac{1}{E - \frac{p^2}{m} - \frac{3q^2}{4m} + i\epsilon} [\\
 & \sum_{\alpha', \alpha''} \int_0^\infty dq'' q''^2 \int_{-1}^1 dx t_{\alpha, \alpha'}^+ \left(p, \pi_1(q, q'', x), E - \frac{3q^2}{4m} \right) \\
 & * \frac{\tilde{G}_{\alpha', \alpha''}(q', q'', x)}{\pi_1' \pi_2'''} \left\langle \pi_2, q'', \alpha_{J'', M_{J''}} | \psi_i \right\rangle \\
 & + \sum_{\alpha''} \int_0^\infty dp'' p''^2 \int_0^\infty dq'' q''^2 V_{\alpha, \alpha''}^4(p, q, p'', q'') \left\langle p'', q'', \alpha_{J'', M_{J''}} | \psi_i \right\rangle \\
 & + \sum_{\alpha', \alpha''} \int_0^\infty dq' q'^2 \int_0^\infty dq'' q''^2 \int_{-1}^1 dx V_{\alpha, \alpha'}^4(p, q, \pi_1(q', q'', x), q') \\
 & + \frac{\tilde{G}_{\alpha', \alpha''}(q', q'', x)}{\pi_1' \pi_2'''} \left\langle \pi_2, q'', \alpha_{J'', M_{J''}} | \psi_i \right\rangle \\
 & + \sum_{\alpha', \alpha''} \int_0^\infty dp' p'^2 \int_0^\infty dp'' p''^2 \int_0^\infty dq'' q''^2 t_{\alpha, \alpha'}^+ \left(p, p', E - \frac{3q^2}{4m} \right) \frac{1}{E - \frac{p'^2}{m} - \frac{3q^2}{4m} + i\epsilon} \\
 & * V_{\alpha', \alpha''}^4(p', q, p'', q'') \left\langle p'', q'', \alpha_{J'', M_{J''}} | \psi_i \right\rangle \\
 & + \sum_{\alpha', \alpha'', \alpha'''} \int_0^\infty dp' p'^2 \int_0^\infty dq'' q''^2 \int_0^\infty dq' q'^2 \int_{-1}^1 dx t_{\alpha, \alpha'}^+ \left(p, p', E - \frac{3q^2}{4m} \right) \\
 & * \frac{1}{E - \frac{p'^2}{m} - \frac{3q^2}{4m} + i\epsilon} V_{\alpha', \alpha'''}^4(p', q, \pi_1(q', q'', x), q') \\
 & * \frac{\tilde{G}_{\alpha''', \alpha''}(q', q'', x)}{\pi_1''' \pi_2'''} \left\langle \pi_2, q'', \alpha_{J'', M_{J''}} | \psi_i \right\rangle \Big],
 \end{aligned} \tag{2.41}$$

where

$$V_{\alpha, \alpha'}^4(p, q, p', q') \equiv \left\langle p, q, \alpha_{J, M_J} \left| V_4^{(1)} \right| p', q', \alpha_{J', M_{J'}} \right\rangle \tag{2.42}$$

2.4 3N scattering state

As in Sec. 2.5, one can write an equation for the 3-nucleone scattering state:

$$|\Psi^{(-)}\rangle^{3N} = \frac{1}{\sqrt{3}} \left| \Psi_j^{(-)} \right\rangle^{3N} \tag{2.43}$$

with a set of corresponding equations for $\left| \Psi_j^{(-)} \right\rangle^{3N}$

$$\left| \Psi_j^{(-)} \right\rangle^{3N} \equiv \lim_{\epsilon \rightarrow 0} i\epsilon G(E_{3N} - i\epsilon) \left| \Phi_j^{3N} \right\rangle \quad (2.44)$$

$$\left| \Phi_j^{3N} \right\rangle \equiv \frac{1}{\sqrt{2}} (1 - P_{kl}) |\vec{p}(kl) \vec{q}(j)\rangle \quad (2.45)$$

$$E_{3N} = \frac{|\vec{p}|^2}{m} + \frac{3|\vec{q}|^2}{4m}, \quad (2.46)$$

2.5 Photodisintegration transition amplitude for Nd state

Analogously to the bound state, one can express a nucleon-deuteron scattering state using a permutation operator Eq. (2.38).

$$\left| \Psi^{(-)} \right\rangle^{Nd} = \frac{1}{\sqrt{3}} (1 + P) \left| \Psi_1^{(-)} \right\rangle^{Nd} \quad (2.47)$$

Further a scattering state $\left| \Psi_1^{(-)} \right\rangle^{Nd}$ can be expressed in terms of asymptotic state $\left| \Phi_1^{Nd} \right\rangle$, in which particles 2 and 3 form a deuteron and the third particle (nucleon 1) propagates freely with a relative momentum \vec{q}_0 with respect to the deuteron:

$$\left| \Psi_1^{(-)} \right\rangle^{Nd} \equiv \lim_{\epsilon \rightarrow 0} i\epsilon G(E_{Nd} - i\epsilon) \left| \Phi_1^{Nd} \right\rangle \quad (2.48)$$

$$\left| \Phi_1^{Nd} \right\rangle \equiv \left| \Phi_{d(2,3)} \right\rangle |\vec{q}_0\rangle, \quad (2.49)$$

where $\left| \Phi_{d(2,3)} \right\rangle$ is a deuteron wave function and $|\vec{q}_0\rangle$ - a free particle state. E_{Nd} is a total energy of the 3N system:

$$E_{Nd} = E_d + \frac{3|\vec{q}_0|^2}{4m}, \quad (2.50)$$

where E_d is the deuteron binding energy and m denotes nucleon mass.

The full propagator $G(E_{Nd})$ in this case takes a form:

$$G(z) = \frac{1}{z - (H_0 + \sum_{i=1}^4 V_i)} \quad (2.51)$$

2.6 Nuclear electromagnetic current

2.7 Theoretical uncertainties

Truncation error

As it was mentioned above, each subsequent order of the chiral expansion provides us with more and more sophisticated potential which is expected to increase accuracy of data description. Starting from the leading order (LO) and coming next to N2LO, N3LO etc., we take into account more topologies (equivalents of Feynmann diagrams) and in result potential is expected to provide us with more precise predictions for the regarded

process and observables. However, the chiral expansion (as any expansion) in principle can be continued up to the infinity, improving the resulting series. In practice we are limited to a finite, rather small, order and we would like to find out the uncertainty appearing from cutting off remaining part of the expansion. That type of theoretical uncertainty is called a truncation error. Various methods to estimate its value have been proposed [?, ?, ?, ?, ?]. Typically predictions at lower orders serve as input information to get truncation error at given order. It is worth adding that Bayesian analysis is also used for truncation error estimation

We use the method proposed in [?] which was shown to be equivalent to Bayesian approach. Let's regard some prediction $X^i(p)$ for observable x which is calculated at i -s order of chiral expansion with expansion parameter Q ($i = 0, 2, 3, \dots$)¹. Here p specifies a momentum scale of the current reaction in the center of mass frame (in the case of photodisintegration it would be a photon's momentum).

If we define a difference between observable at each subsequent orders as:

$$\Delta X^{(2)} = |X^{(2)} - X^{(0)}|, \Delta X^{(i>2)} = |X^{(i)} - X^{(i-1)}|, \quad (2.52)$$

then chiral expansion for X can be written as:

$$X = X^{(0)} + \Delta X^{(2)} + \Delta X^{(3)} + \dots + \Delta X^{(i)}. \quad (2.53)$$

The truncation error at i -th order, $\delta X^{(i)}$, is estimated using actual and expected values of the observable at higher orders as following:

$$\delta X^{(0)} = Q^2 |X^{(0)}|, \quad (2.54)$$

$$\delta X^{(i)} = \max_{2 \leq j \leq i} (Q^{i+1} |X^{(0)}|, Q^{i+1-j} |\Delta X^{(j)}|). \quad (2.55)$$

Additionally, following the [?] I use also the actual high-order predictions (if known) in order to specify uncertainties so that:

$$\delta X^{(i)} \geq \max_{j,k} (|X^{j \geq i} - X^{k \geq i}|) \quad (2.56)$$

and to be conservative I use additional restriction:

$$\delta X^{(i)} \geq Q \delta X^{(i-1)}. \quad (2.57)$$

All the conditions above assume that we use the whole available information at hand. In [?] [????](#) it was shown that such method is equivalent to Bayesian approach of [?].

Cutoff dependency

Another theoretical uncertainty comes from the choice of the cutoff parameter's value of regulator described in chapter [?????? put link](#).

The free parameters of SMS potential have been obtained from data for four values of the cutoff parameter Λ : 400, 450, 500 and 550 MeV [?]. Using each of these values, one obtains different predictions which of course can further differ from actual (experimental) value. Therefore the choice of Λ value may affect a quality of the prediction.

¹We do not have a first order of expansion because this term in chiral expansion is always vanished and NLO corresponds to the quadratic term (number 2)

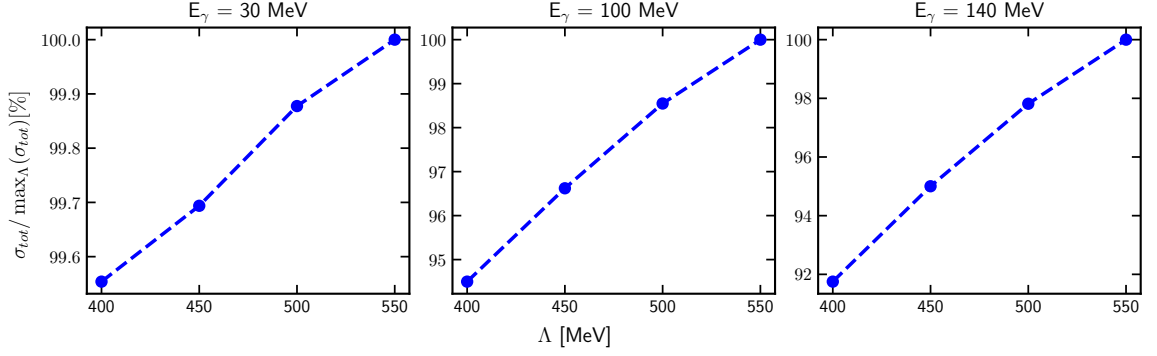


Figure 2.3: Total cross section of the deuteron photodisintegration process (normalized to the maximal cross section among all Λ) as a dependance on the cutoff parameter Λ for three photon energy E_{γ} values: 30, 100 and 140 MeV.

To study that I also use the same four values of the Λ parameter, obtaining in that way four predictions each time. That is exemplified in Fig. 2.3 for the deuteron photodisintegration cross section for the photon's energy $E_{\gamma} = 30$ MeV, 100 MeV and 140 MeV. The SMS model at $N^4\text{LO}^+$ is used. Each subfigure shows a predictions for the total cross section as a function of the cutoff parameter, normalized to the maximum value among all cross sections obtained with various Λ . As we can see, for that observable there is almost linear dependance with positive linearity coefficient value: with higher Λ the cross section value increases as well. Note that with higher photon's energy, the cutoff dependance becomes stronger: for $E_{\gamma} = 30$ MeV the maximal difference between predictions is around 0.5 % while for 140 MeV it increases to more than 8 %. This results are generally within our expectations that our model works better at smaller energies and is less sensitive to the Λ value. Let us remind that Λ governs the behavior of the potential at small internucleon distances and only higher energy transfer probes that distances.

Other theoretical uncertainies

There are obviously more sources of theoretical uncertainties. Our model has a number of either intrinsic limitations in precision or some simplifications which may be improved with further developments of the model.

Nuclear currents At the moment we have only a single nucleon current consistent with the model available. In most cases it is not enough to proper describe regarded processes which will be confirmed in Chapter 3. We deal with this problem applying the Siegert theorem which allows to include some contribution from the 2N current, which is still not complete.

Nonrelativistic approach All the results presented here does not include relativistic corrections. At the lower energies the relativistic contribution might not be crucial, but at the region with higher energy we may see a lack of precision. This well be also confirmed and discussed regarding the total cross section for the deuteron photodisintegration Fig. 3.2.

Uncertainties in the potential free parameters ????

Uncertainties from the numerical method All the results include numerical calculations, so we can come up with a lot of places where numerical methods with limited precision come into the scene. Our approach is based on the partial wave decomposition which supposes that limited number of partial waves are included (usually for 2N scattering we use $j^{max} = 4$ which corresponds to 18 partial waves). For 3N calculations we use $J^{max} = 5$ which corresponds to 40 partial waves. In addition, we with some grid of points which is used for the calculation of potential, wave function, numerical integration etc. The choice of grid affect a final results' precision. Usually, we use a grid *of ... values* which was proven to make resulting uncertainty small.

Model choice We focus on the SMS potential, but using another model of interaction leads to different predictions. That difference is also a theoretical uncertainty thus we use predictions obtained with AV18 model in order to compare these predictions.

Machine precision Finally every computer calculations include limited numerical machine precision which can be noticeable for a complex calculations. We perform our calculation via CPU machine where particular choice of the processor and memory card may lead to numerical uncertainty. Nevertheless this uncertainty is much smaller than other discussed above.

CHAPTER 3

RESULTS

In this chapter I will show results of my calculations. I start from the deuteron photodisintegration process (Section 3.1), presenting predictions and discussing the cross (subsection 3.1.1) and polarization observables (subsection 3.1.2). Next, in Section 3.2 I will present my predictions of the observables for ^3He photodisintegration. ... Finally in Section 3.3 I will discuss results of the calculations for pion absorption from the lowest atomic orbital.

3.1 Deuteron photodisintegration

3.1.1 Cross section

In this section I will show the results of my calculation starting from the deuteron photodisintegration process. One of the most studying observable is obviously the cross section. There is a number of papers which present measurement results for both differential and total cross section [?, ?, ?, ?, ?, ?, ?, ?] and it seems interesting to compare our predictions with experimental results.

In Fig. 3.1 and Fig. 3.2 I present predictions for the total cross section σ_{tot} [μb] which I obtained using the chiral SMS potential at the N^4LO^+ order and with the cutoff parameter $\Lambda = 450\text{ MeV}$. From Fig. 3.1, we see that at low photon energies (below 50 MeV) predictions which include 2N contributions to the electromagnetic current via the Siegert approach, describe experimental results quite well. We can suppose that the difference with experimental data may come from the statistical uncertainty of the data itself, as my predictions are often in between the data from different experiments. Moreover, even at such low energies the 1N current is clearly not enough to describe cross section - dashed pink line has much lower values and the difference becomes even larger with increasing photon energies. At 5 MeV the difference between 1N predictions and 1N + Siegert is $297.54\ \mu\text{b}$ (10.8%), increasing energy to 10 MeV it is $304.28\ \mu\text{b}$ (20.4%) and at 20 MeV it is $229.50\ \mu\text{b}$ (39.2%). From Fig. 3.1 we see that the gap between these predictions continues increasing even more with larger energies. This tells us that Siegert approach works quite well as no additional 2N contributions are taken into account. The cross section predictions corrected via Siegert 2N contribution reproduce experimental data to some extend.

Here and later the relative difference between set of predictions (x_1, x_2, \dots, x_N) is calculated using the formula:

$$\Delta = \frac{\max(x) - \min(x)}{\frac{1}{N} \sum_{i=1}^N x_i} \cdot 100\%, \quad (3.1)$$

so in the specific case of comparison the data with 1N current and "1N + Siegert" we calculate relative difference as $\Delta = \frac{|\sigma^{1N+Siegert} - \sigma^{1N}|}{0.5(\sigma^{1N+Siegert} + \sigma^{1N})}$.

While my main goal is to describe deuteron photodisintegration at low energies, where predictions seem to be well describing experimental data at $E_\gamma \lesssim 50$ MeV, it is also interesting to check how present theory works at higher energies. At the higher energies (above $E_\gamma = 50$ MeV, Fig. 3.2) we can notice that the discrepancy with experimental data is not only quantitative, but also qualitative. This starts already above $E_\gamma = 50$ MeV and is especially pronounced at peak around 300 MeV seen in the experimental data from [?] which is not reflected in predictions. The reason of such discrepancy is most likely coming from the relativistic effects which we do not take into account within this work. It is also confirmed by the calculations in [?] where authors discuss different potentials applying to the deuteron photodisintegration. Despite authors use a much simpler potentials that used in this thesis, their predictions obtained with including some relativistic effects show, that such a peak appears in predictions.

The higher energies region is presented in order to investigate how far the predictions are from experimental results and what should be improved in the future (e.g. include relativistic part).

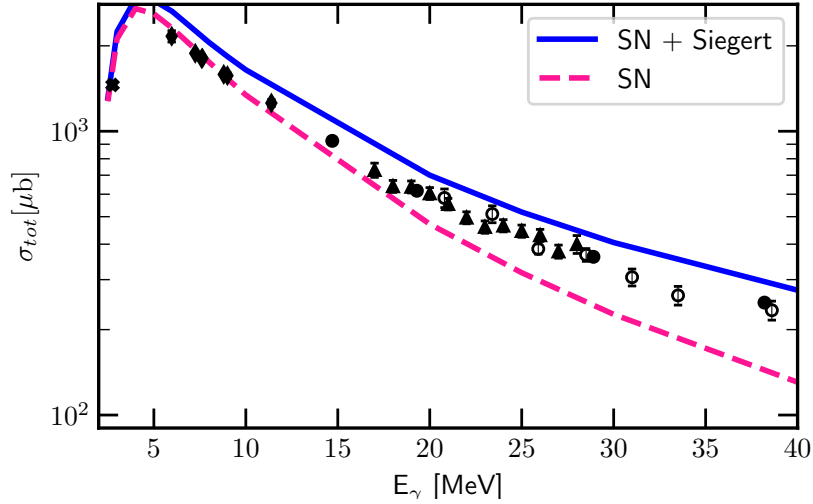


Figure 3.1: Total cross section σ_{tot} for the deuteron photodisintegration process as a function of the photon's energy E_γ . Solid blue line presents results obtained with SN+Siegert and dashed pink line - predictions based on the SN current. In both cases the SMS N^4LO^+ $\Lambda = 450$ MeV force is used. The experimental data are from [?] (black filled circles), [?] (empty circles), [?] (triangles), [?] (bold cross "X") and [?] (diamonds).

In Fig. 3.3 I present the total cross-section for the deuteron photodisintegration at three photon energy values: 30, 100 and 140 MeV as a function of the chiral order. Error bands show truncation errors calculated using Eq. 2.54 - 2.57. One can see that truncation

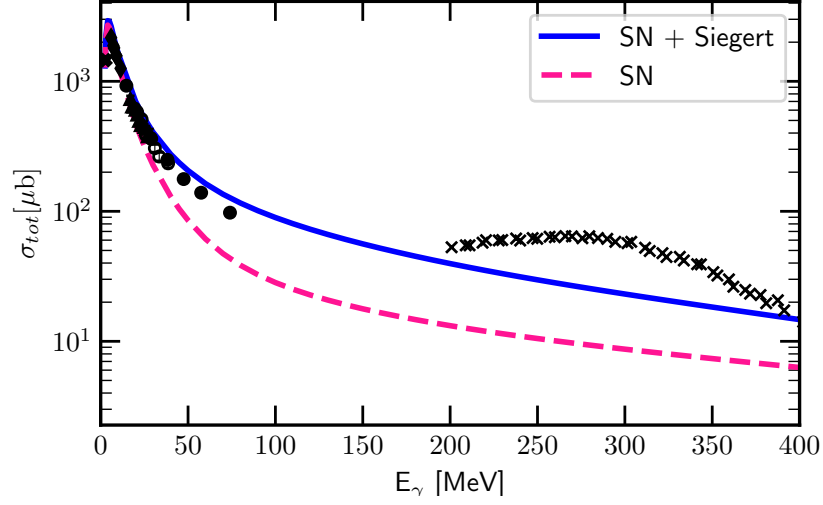


Figure 3.2: The same as in Fig. 3.2 but for the energy range 2.5 - 400 MeV. The experimental data are the same plus data above $E_\gamma = 200$ MeV from [?] (crosses).

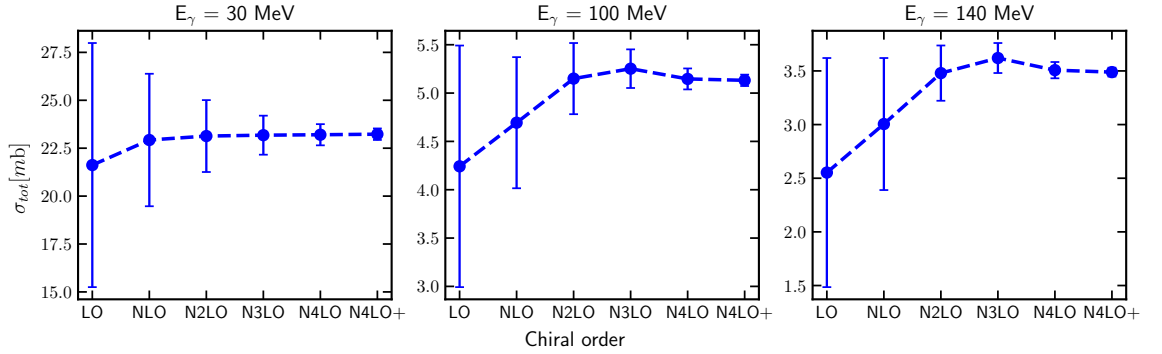


Figure 3.3: Total cross section of the deuteron photodisintegration process as a dependence on the chiral order for three photon energy E_γ values: 30, 100 and 140 MeV. Error bands show an estimated truncation error at each order.

errors are being reduced with each consecutive chiral order. At LO it is the biggest: 29.46 % at $E_\gamma = 30$ MeV, 29.46 % at $E_\gamma = 100$ MeV and 41.82 % at $E_\gamma = 140$ MeV. At N4LO+ it is hardly visible at presented scale and amounts up to 1.3 % for each energy. For each energy the prediction is within the uncertainty range of lower orders. We see that at lower energy σ_{tot} already at NLO reaches value which remains practically unchanged at higher orders. Contrary, at two higher energies, contributions from higher orders are necessary to obtain stable predictions

Figures 3.4 and 3.5 show my predictions for the differential cross section $\frac{d\sigma}{d\Omega}$. In both figures the top, middle and bottom row shows predictions at $E_\gamma = 30$, 100 and 140 MeV, respectively. with 2N current's contributions taken into account via Siegert theorem. If not stated otherwise I use the SMS N⁴LO⁺ potential. The left column of Fig. 3.4 shows the predictions obtained at different chiral orders (from LO to N⁴LO⁺) and with $\Lambda = 450$ MeV. Looking at the best predictions (N⁴LO⁺, $\Lambda = 450$ MeV) for each energy, I conclude that the higher photon's energy is, the larger is difference between the theoretical

predictions and experimental data. At $E_\gamma = 30$ MeV (top panel) my predictions almost perfectly match the data and the difference is almost always within the experimental uncertainties. Moving to $E_\gamma = 100$ MeV (middle row) the description of the data is deteriorating: theoretical predictions still match the data qualitatively, but the gap for proton emission angle θ_p in range ($60^\circ < \theta_p < 130^\circ$) is up to 32 % (of the predicted value) and relative difference is up to 7 % (calculated with Eq. (3.1)). At the highest energy (bottom figure), it is even hard to say about good qualitative description: the general trend of the angular dependence is presented, but the predictions are far from the experimental points. We observe improvements introduced by each subsequent chiral order, but stabilization shows that some ingredients are missing.

Obtained results at each energy confirm the convergence of the predictions with respect to the chiral order. We see that the cross section at LO is far from both experimental data and the best potential's predictions ($N^4\text{LO}^+$) and the higher photon's energy, the larger is this difference. With each subsequent chiral order, the curves are more closer to each other and the difference between $N^4\text{LO}$ and $N^4\text{LO}^+$ is hardly visible at scale used in Fig. 3.3. The relative difference between these two predictions at $E_\gamma = 30$ MeV around the point of maximum ($\theta_p = 80^\circ$) is 0.05 % which is $0.02 \frac{\mu\text{b}}{\text{sr}}$; at 100 MeV and $\theta_p = 107^\circ$ it is 0.79 % ($0.025 \frac{\mu\text{b}}{\text{sr}}$); and at 140 MeV (same angle) it is 1.8 % ($0.043 \frac{\mu\text{b}}{\text{sr}}$). Having such a small differences between predictions from two highest chiral orders, I can conclude that predictions are converged and using NN potential at subsequent chiral orders would rather not bring large contribution to the cross section values. The difference with experimental data is rather systematic and is independent on the chiral order. The relative difference between experimental data and predictions obtained with $N^4\text{LO}^+$ and $\Lambda = 450$ MeV at 30 MeV is less than 13 % and absolute difference is $< 3.07 \frac{\mu\text{b}}{\text{sr}}$. At 100 MeV discrepancy is larger and relative difference reaches 46% with absolute difference up to $1.39 \frac{\mu\text{b}}{\text{sr}}$. Coming to 140 MeV the relative difference increases up to 48.6 % and absolute - $1.93 \frac{\mu\text{b}}{\text{sr}}$. What may be helpful for a better data description is a 2N current and relativistic correction, mentioned earlier.

Predictions obtained with the AV18 potential (dashed-dotted purple line on the Fig. 3.4 left) are very similar to these from the SMS force at lower energies (relative difference at $E_\gamma = 30$ MeV is 0.06 % at the point of maximum - $\theta_p = 80^\circ$) and with increasing energy to 140 MeV it grows to 3.1 % at the same angle. It can be connected with our potential's quality loss, but AV18 can be struggling with high energies as well. Then other components of Hamiltonian become important at that energies.

In the right column of the Fig. 3.4 I compare predictions based on various assumptions on nuclear current and dynamical mechanism. I again use SMS $N^4\text{LO}^+$, $\Lambda = 450$ MeV force. At the lowest energy predictions with plane-wave component only (without rescattering part) has relatively small deviation from the full predictions, but the difference increases at larger energies. With $E_\gamma = 30$ MeV the relative difference is 10 % ($4.03 \frac{\mu\text{b}}{\text{sr}}$) at $\theta_p = 80^\circ$. Difference at 100 MeV and the same angle is 4 % ($0.21 \frac{\mu\text{b}}{\text{sr}}$) and at 140 MeV it is 7 % ($0.21 \frac{\mu\text{b}}{\text{sr}}$). In contrast, predictions without two-body current component (1NC) have much larger gap with full prediction: the difference is 46.5 % ($13.67 \frac{\mu\text{b}}{\text{sr}}$) at 30 MeV, 78.6 % ($2.88 \frac{\mu\text{b}}{\text{sr}}$) at 100 MeV and 77.8 % ($1.68 \frac{\mu\text{b}}{\text{sr}}$) at 140 MeV at the same $\theta_p = 80^\circ$. Obviously 2NC contributions are extremely important in this case, the difference connected with 2NC contributions is much higher than theoretical errors or even rescattering contribution. For other scattering angles, especially $\theta_p = 0^\circ$ or $\theta_p = 180^\circ$, the role of two-body current or FSI is even more pronound.

The Fig. 3.5 (left) presents theoretical truncation uncertainties. That confirms our

expectations that for the regarded photo reaction chiral order N^4LO^+ is able to produce converged predictions: the black band is hardly visible for the $E_\gamma = 30$ MeV (the relative error for N^4LO^+ at 80° is only 0.12 %) and is also quite narrow for larger energies (at 140 MeV the error at the same angle is 1.46 %). At the lower chiral orders, this band is obviously much wider: at N^2LO it is 1.25 % at $E_\gamma = 30$ MeV and 15.0 % at $E_\gamma = 140$ MeV.

Finally, Fig. 3.5 (right) presents a cutoff dependence of the differential cross section. The ideal case is when the dependency is so weak that the choice of the parameter Λ would not make significant changes. In practice the choice of this parameter can be important as it makes a noticeable difference in prediction at higher energies. Namely, while on the top of Fig. 3.5 ($E_\gamma = 30$ MeV) the cutoff dependence is so tiny, that, in fact, all the lines (for different Λ values) overlap each other and we cannot distinguish them with the naked eye: the relative difference at maximum is 0.08 %. This is approximately $\frac{2}{3}$ smaller than truncation error discussed above. However, with increasing photon energy up to 100 MeV and 140 MeV (middle and bottom rows of the right column of Fig. 3.5) the spread becomes bigger: the uncertainty related to the Λ -dependence is 3.35 % at 100 MeV and 5.66 % at 140 MeV (the same θ_p). Thus at two higher energies the cut-off dependence becomes more important than truncation errors. That shows, that proper choice of the Λ is important. However, if I restrict myself to $\Lambda = 450$ MeV and 500 MeV, the dependence drops to 1.98 % at $E_\gamma = 140$ MeV.

On the Fig. 2.3 we saw that the total cross section for the same energies has the cutoff spread around 4.5 % for 100 MeV and 8 % for 140 MeV. For $E_\gamma = 30$ MeV it is below 1 %.

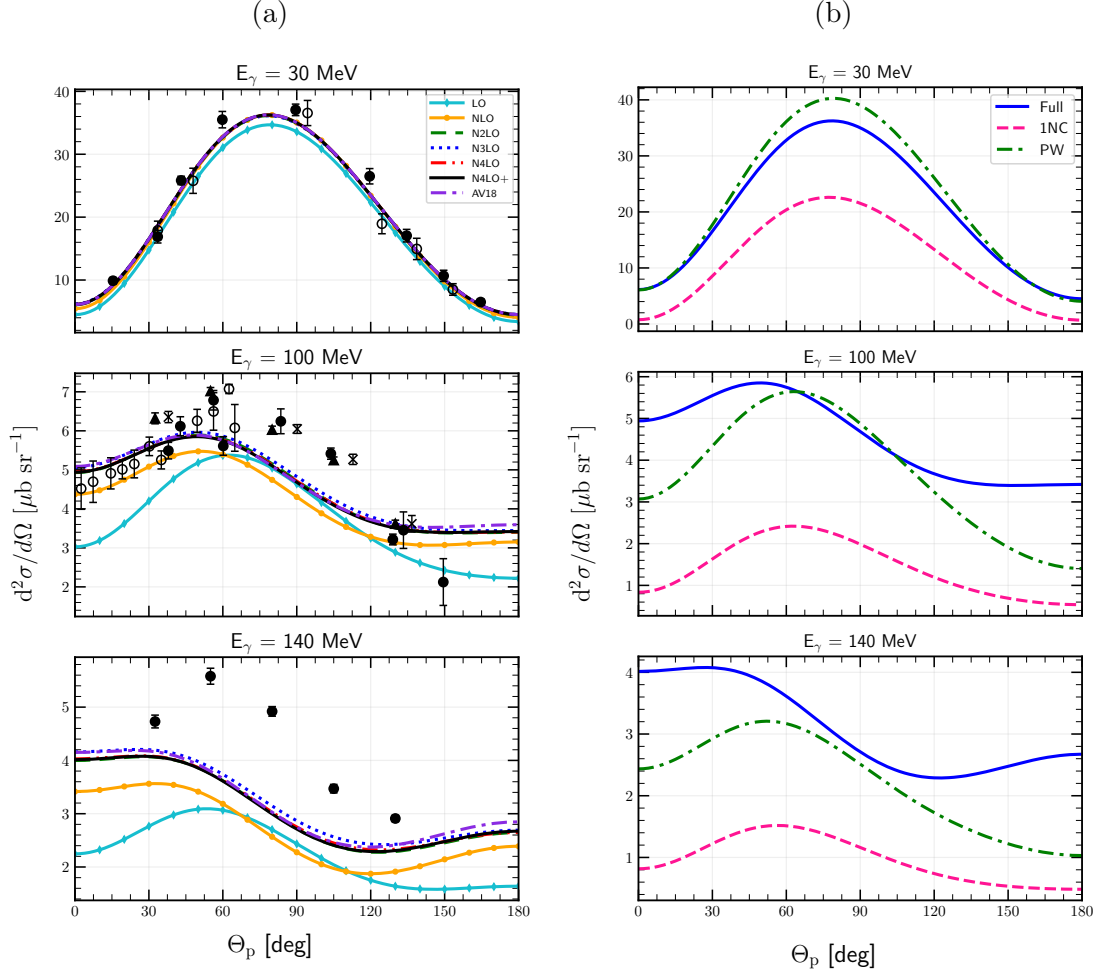


Figure 3.4: Differential cross section $\frac{d^2\sigma}{d\Omega}$ as a function of the outgoing proton momentum polar angle θ_p in the center of mass frame for the photon energy 30 MeV (top), 100 MeV (middle) and 140 MeV (bottom). **(a)** Results obtained using the SMS potential at different chiral orders (from LO to N⁴LO⁺) with the cutoff parameter $\Lambda = 450$ MeV and 2NC contributions taking via the Siegert theorem. For the sake of comparison, predictions obtained with the AV18 potential are shown by dashed-dotted purple line. Data points (filled and empty circles) are from [?] for $E_\gamma = 30$ and 100 MeV and [?] for $E_\gamma = 140$ MeV. **(b)** Predictions obtained with the chiral N⁴LO⁺ potential and $\Lambda = 450$ MeV with various models of nuclear current(1N and 2N) and scattering state. The blue solid curve is plane-wave plus rescattering parts, 1NC + Siegert(the same as N⁴LO⁺ line in (a)). The pink dashed curve shows predictions obtained with the single-nucleon current only (without applying the Siegert theorem) and the green dashed-dotted curve represents predictions with the full current(1N + Siegert) but plane-wave part only.

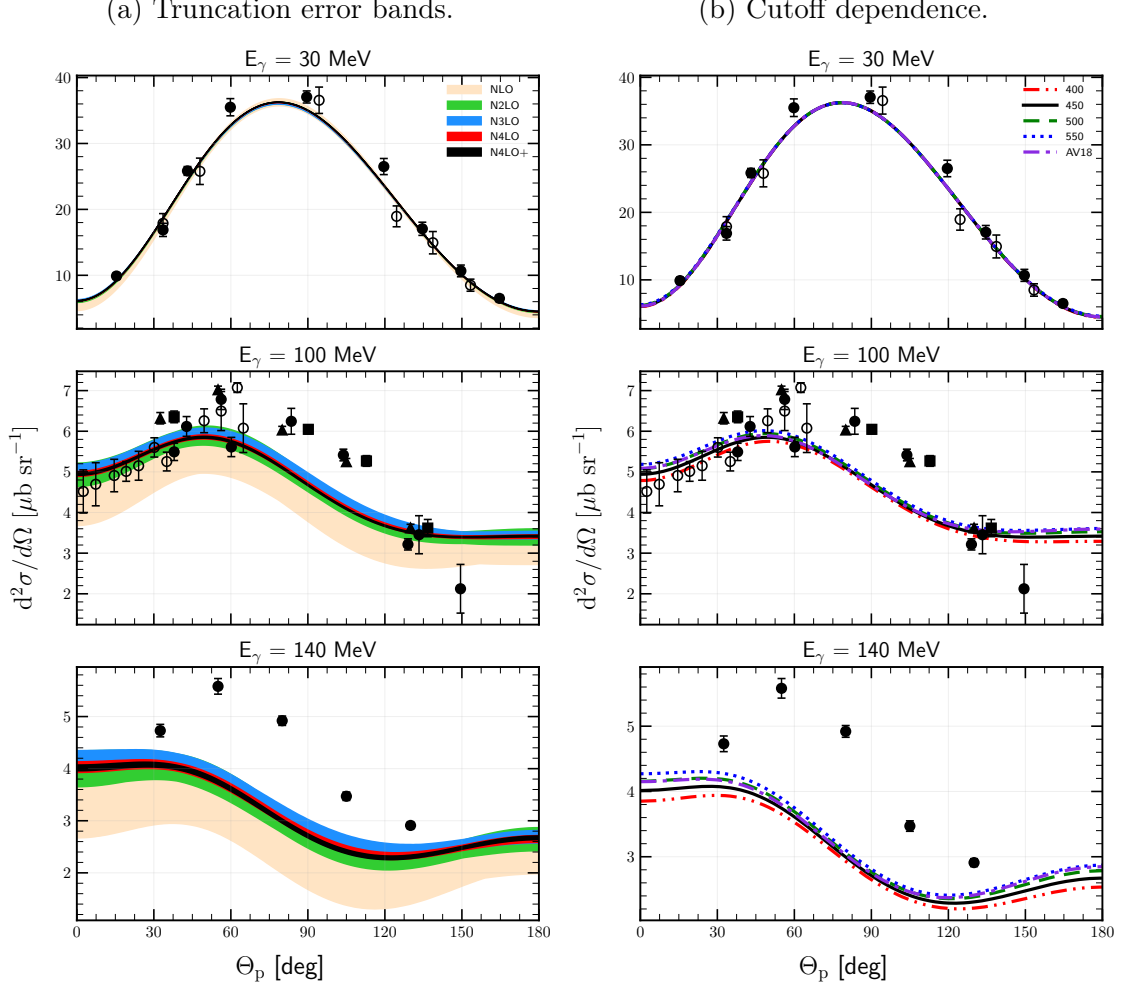


Figure 3.5: Theoretical uncertainties for the differential cross section $\frac{d^2\sigma}{d\Omega}$ as a function of the outgoing proton's momentum polar angle θ_p in the center of mass frame for the photon energy is 30 MeV (top row), 100 MeV (middle row) and 140 MeV (bottom row). **(a)** The truncation error bands for each energy in a corresponding row. Results are obtained using the SMS potential at different chiral orders (from NLO to $N^4\text{LO}^+$) with the cutoff parameter $\Lambda = 450$ MeV and 2NC contributions taking via the Siegert approach. **(b)** Predictions obtained using different values of the cutoff parameter Λ . The double-dotted-dashed red curve, the solid black line, the dashed green line and the dotted blue line represent predictions obtained with $\Lambda = 400, 450, 500$ and 550 MeV respectively and the chiral potential $N^4\text{LO}^+$. Data points are the same as in Fig. 3.4a

3.1.2 Polarisation observables

In this subsection I will present my predictions for selected polarisation observables. I start with deuteron vector iT_{11} and tensor T_{20} , T_{21} and T_{22} analyzing power, which are defined as [?]:

$$iT_{11}(\theta) = -2 \frac{\text{Im } V_{11}}{V_{00}}, \quad (3.2)$$

$$T_{2i}(\theta) = \frac{(2 - \delta_{i0}) \text{Re } V_{2i}}{V_{00}}, i = 0, 1, 2, \quad (3.3)$$

where V_{ij} is *??? all derivation?*.

On the Figures 3.6 (a, b) and 3.7(a,b) I show my predictions at $E_\gamma = 30$ MeV, for the T_{20} , T_{21} , T_{22} and iT_{11} respectively as functions of the outgoing proton angle θ_p in the centre of the mass (CM) frame. Each of them is organized in the similar way: the top panel shows a dependence of the predictions on the chiral order of the potential. The middle subfigure is showing a correspondent truncation error for each of the predictions from a top row (excepting LO, because its uncertainty is too large and will make the readability worse). The last (bottom) panel shows the cutoff dependence at the chiral order $N^4\text{LO}^+$.

All the analyzing powers presented here show excellent convergence upon a chiral order as it is hard to distinguish the predictions from each subsequent order starting from the $N^2\text{LO}$. The relative width of $N^4\text{LO}^+$ truncation band for T_{20} , T_{21} and T_{22} are 0.06 %, 0.05 % and 0.19 % respectively (at $\theta_p = 90^\circ$, 60° and 90° respectively). The slowest convergence is observed for iT_{11} (Fig. 3.7b) where we can recognize $N^2\text{LO}$ band. Still at $N^4\text{LO}^+$ it has only a 0.2 % width truncation band at $\theta_p = 20^\circ$ (maximum point). The cutoff dependency for all regarded observables is weak and predictions for each value of the Λ are hardly separable with the naked eye. The relative spread of the predictions based on various Λ at the same angles as above are 0.87 %, 0.94 %, 3.42 % and 0.68 % for T_{20} , T_{21} , T_{22} and iT_{11} , respectively.

Predictions for the photon energy $E_\gamma = 100$ MeV (Figs. 3.8 and 3.9) preserve similar trends for each observable. Generally, predictions are being converged starting even from the $N^2\text{LO}$ while for iT_{11} we can see that truncation error's bands are noticeably wide even at $N^4\text{LO}$ and $N^4\text{LO}^+$. Cutoff dependence at this energy is a bit stronger compared to those at $E_\gamma = 30$ MeV, especially for T_{22} and iT_{11} analyzing powers (Fig. 3.7), where one can see slightly stronger discrepancy at the stationary points.

Looking at the predictions for the deuteron tensor analyzing powers, we can conclude that cutoff dependence is generally weak and the choice of Λ does not affect predictions much even at that higher energy: the relative spread among all cutoffs for T_{20} is 2.28 % around the point of maximum ($\theta_p = 90^\circ$). For other components of the tensor analyzing power spread is: 0.5 % at $\theta_p = 60^\circ$ for T_{21} ; 4.1 % at $\theta_p = 90^\circ$ for T_{22} ; and for iT_{11} : 11.4 % at $\theta_p = 20^\circ$. We see again that iT_{11} has much larger spread in the maximum and is more sensitive to the cutoff choice.

Turning our attraction to the chiral order convergence, we can observe that predictions are mostly converged after $N^2\text{LO}$ or $N^3\text{LO}$. The relative width of $N^4\text{LO}^+$ truncation band for T_{20} , T_{21} and T_{22} are 0.7 %, 0.7 % and 0.04 % respectively (at the same angles as used above). Another case is iT_{11} , for which this width is much larger: 6.8 % at $\theta_p = 20^\circ$. The truncation uncertainty for all analyzing powers is much lower than one, connected to the

choice of cutoff parameter. Although, iT_{11} seems to be more sensitive both to the choice of the cutoff parameter and to the chiral order than other regarded observables. But even for iT_{11} cutoff spread is almost twice larger than truncation error's band. Standing out of other tensor components, iT_{11} can be useful for the investigation of the cutoff dependence of the model. Of course, we can repeat once more that our model is less accurate at higher energies which is reflected in a stronger cutoff dependence and slower chiral convergence. However we conclude that even at these energies tensor analyzing powers are converged with respect to the chiral order.

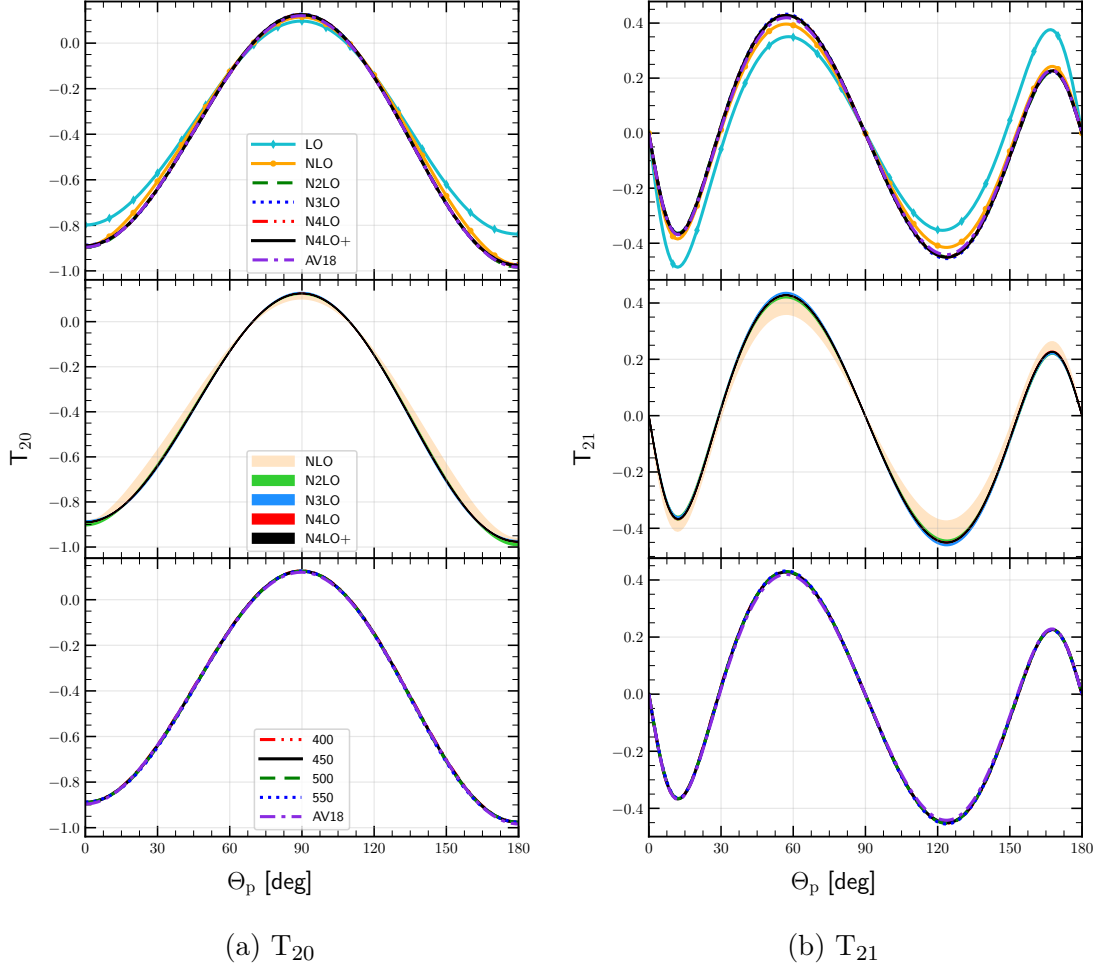


Figure 3.6: Tensor analyzing power T_{20} (a) and T_{21} (b) as a function of the outgoing proton angle in the center of mass frame for the photon's energy 30 MeV. Top row presents results obtained using potential with different chiral orders (from LO to N^4LO^+) with cutoff parameter $\Lambda = 450$ MeV. The middle row shows truncation errors for each chiral order starting from NLO and bottom row presents a cutoff dependency (chiral potential N^4LO^+). For the sake of comparison, predictions obtained with AV18 potential are on figures as well.

In Fig. 3.10 together with best prediction at $E_\gamma = 30$ MeV (N^4LO^+ , $\Lambda = 450$ MeV, Siegert theorem), I show predictions obtained with 1NC only and with plane-wave contribution without rescattering part. In case of deuteron's tensor analyzing power components, the contribution of rescattering part is not that big for T_{20} , T_{21} and T_{22} (up to 20 % in extremum points). Nevertheless, for iT_{11} we see that PW part equals to zero. It may be connected with some features of this particular components, such that plane-

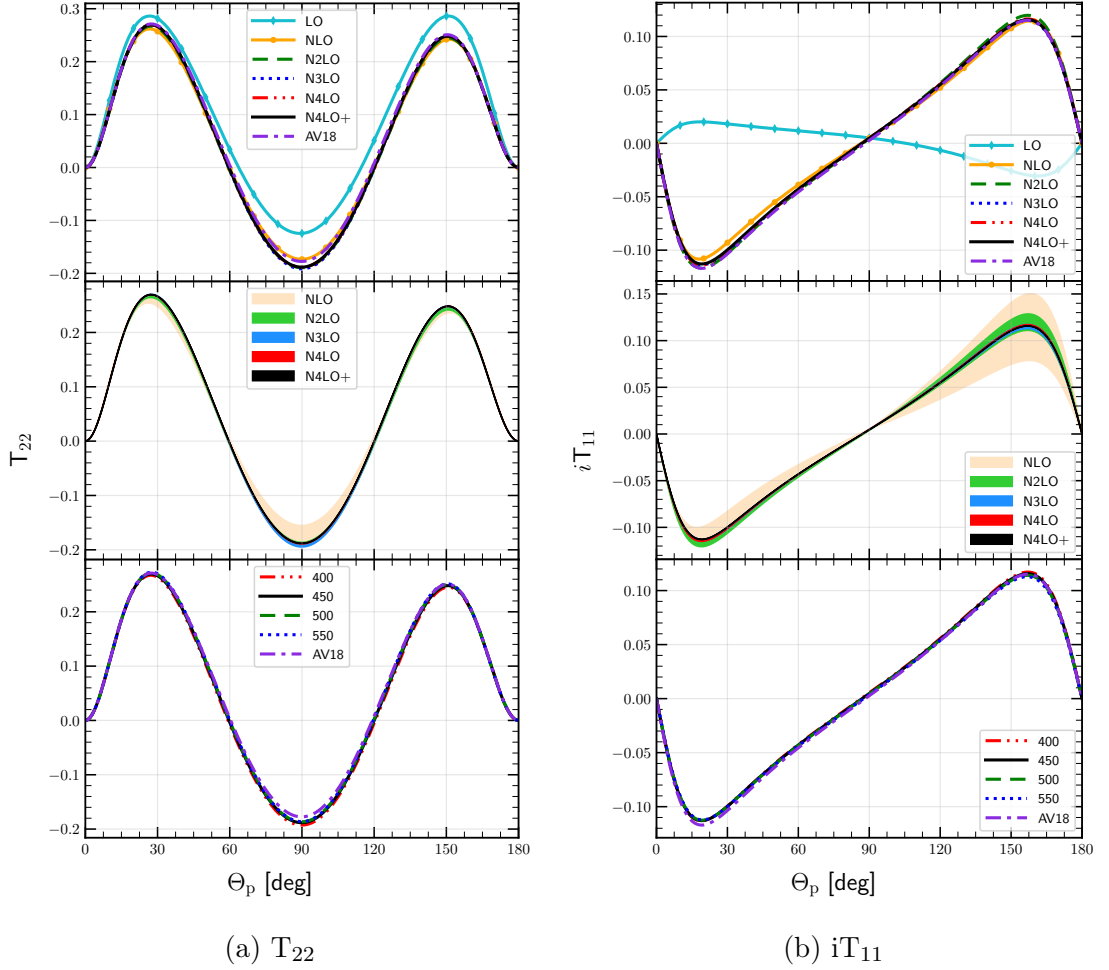


Figure 3.7: The same as on 3.6 but for polarisation observables T_{22} (subfigure (a)) and iT_{11} (subfigure (b)).

wave part cancels out. The 2NC component taken into account via Siegert theorem has a dominant contribution here. We see that 1NC predictions are absolutely away from the Full predictions and in case of iT_{11} does not even reflect total prediction qualitatively.

Fig. 3.11 presents similar results but for $E_\gamma = 30$ MeV and it is interesting that difference between Full and 1NC prediction becomes smaller and it is especially visible for T_{22} . At this energy the relative difference at $\theta_p = 90^\circ$ is 43.6 % comparing to 122.8 % at $E_\gamma = 30$ MeV. Similarly, the difference for T_{20} at $E_\gamma = 30$ MeV ($\theta_p = 90^\circ$) is 91.4 % and at $E_\gamma = 100$ MeV it drops down to 28.8 %. This trend is noticeable looking on Figures (3.12 - 3.18). With

On the next figures, I show the predictions in a similar way as it was done in [?] in order to compare my predictions with the experimental data. On the Figures 3.12 - 3.18 I show an angular dependence of the T_{2i} ($i = 0, 1, 2$) for a specific energy bands. Solid blue line shows an average value of the observable in the specified energy range obtained at N^4LO^+ with $\Lambda = 450$ MeV, while the pink dashed line is a prediction obtained with a same setup but without using a contributions from Siegert approach (single nucleon current only). Bands for each of prediction specify the spread of predictions in regarded energy band.

One can see that the data description is better for the predictions with Siegert contributions and SN current is not able to describe experiment properly. With increasing

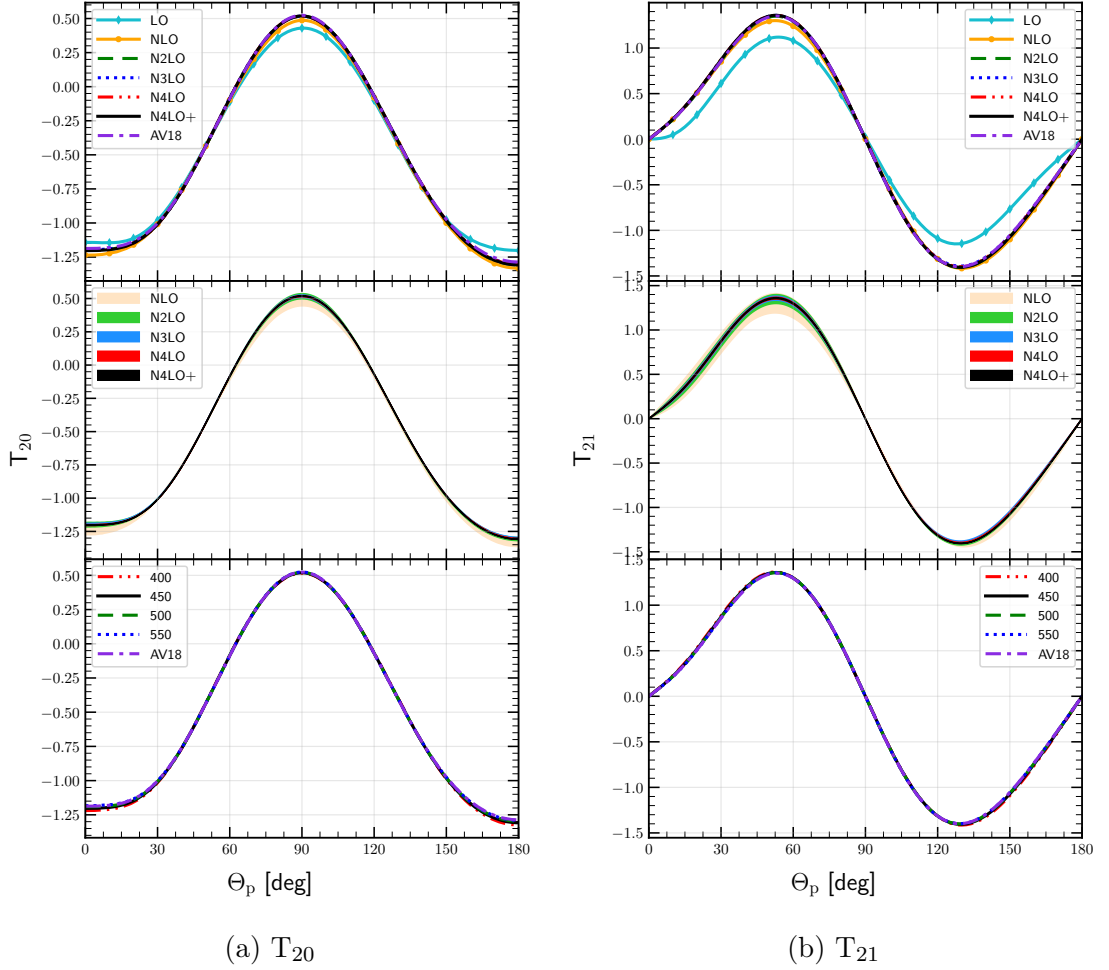


Figure 3.8: Tensor analyzing power T_{20} **(a)** and T_{21} **(b)** as a function of the outgoing proton angle in the center of mass frame for the photon's energy 100 MeV. Top row presents results obtained using potential with different chiral orders (from LO to N^4LO^+) with cutoff parameter $\Lambda = 450$ MeV. The middle row shows truncation errors for each chiral order starting from NLO and bottom row presents a cutoff dependency (chiral potential N^4LO^+). For the sake of comparison, predictions obtained with AV18 potential are on figures as well.

energy (more than 100 MeV), the difference between predicted values and experimental data becomes larger (especially for T_{22}), but the model I use is not meant to be used for high energies and figures are presented out of the curiosity.

On the Figure 3.19 the energy dependence of T_{20} and T_{22} (integrated over all angles) is presented for the energy range 0-400 MeV. I also demonstrate the experimental data from [?] and [?] as well as theoretical calculations from [?] on the figure. For T_{20} the model is able to describe experimental data well even for high energies. On the other hand, T_{22} is not so well described: for the low energies the prediction curve is somehow within uncertainties of experimental data, but further the difference with the data becomes larger. Also it is not reflect the qualitative nature of the data as we can see that after around 150 MeV data points start ascending which is not represented in my predictions. Theoretical predictions from [?] (brown dashed curve) are also not able to describe data quantitatively for T_{22} , but the growth is presented there.

Similar situation is on the Figures 3.20 and 3.21 where I show an energy dependence

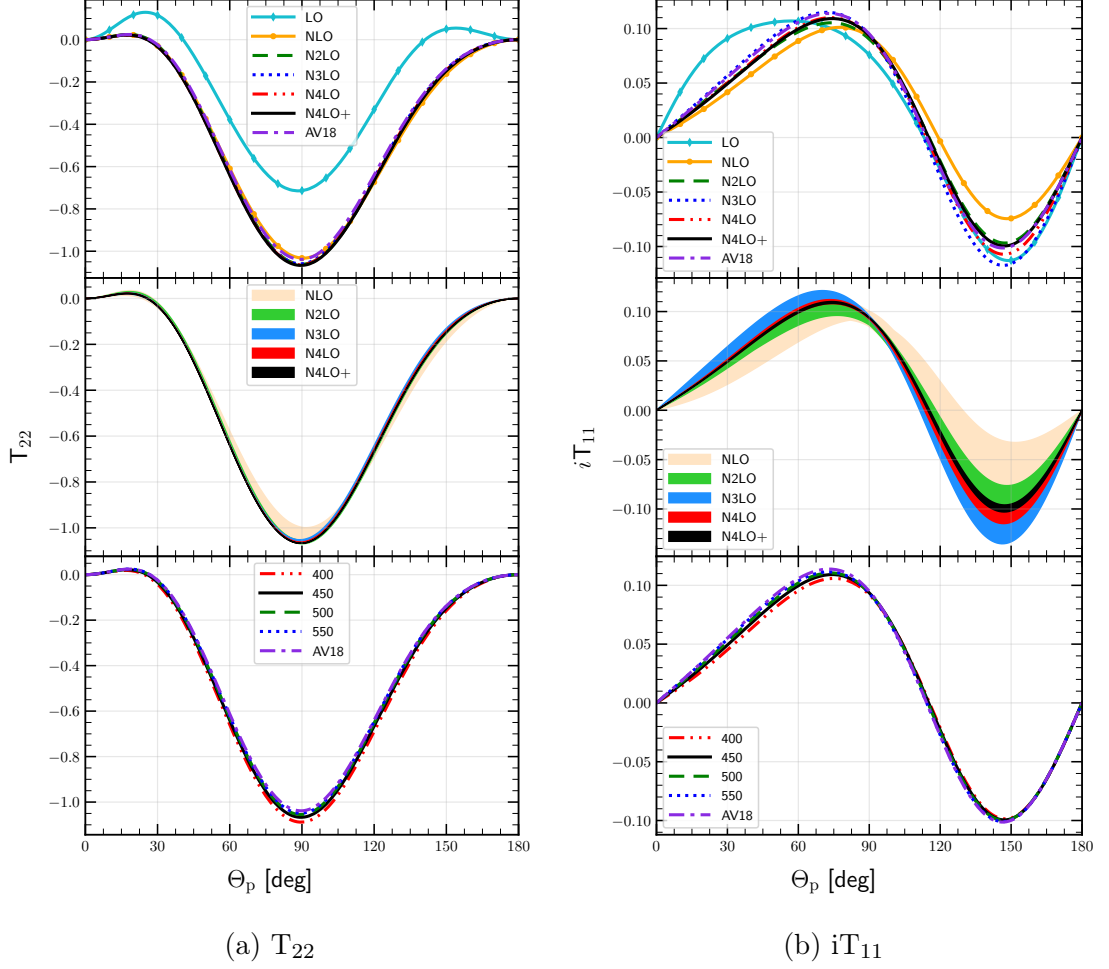


Figure 3.9: The same as on 3.8 but for polarisation observables T_{22} (subfigure (a)) and iT_{11} (subfigure (b)).

of deuteron analyzing power components for specific angular ranges (following the data from [?]). Predictions for T_{20} are able to reflect the experimental results, while for T_{21} and T_{22} predictions are reasonable (quantitative-wise) only for lower energies and difference with data becomes larger when energy increases. Predictions for T_{22} once more confirm an insufficiency of SN and an importance of 2-nucleon current contributions.

On the Fig. 3.22 I demonstrate predictions for the photon asymmetry Σ_γ for the deuteron photodisintegration with $E_\gamma = 20$ MeV (a) and 60 MeV (b) as well as experimental data. Both (a) and (b) figures are organized similarly to the figures I showed earlier for the tensor analyzing power (e.g. Fig. 3.7). That is the top pane is aimed to demonstrate predictions obtained with chiral potential at different orders, the middle one is showing a truncation error bands and the bottom - shows the cutoff dependence. What we can see here is good convergence with respect to the chiral order. For both regarded energies predictions at different orders are very close to each other except for LO and NLO curves. Nevertheless, at 60 MeV we can see that truncation error bands reveal some uncertainty connected with the chiral order and I can assume that even some higher chiral orders would still contribute to the predictions at this energy.

Cutoff dependence is also stronger at 60 MeV. We can clearly see that predictions are different for each value of the Λ . The standard deviation with respect to the cutoff parameter at 20 MeV does not exceed 0.7% of the mean value while at the photon's

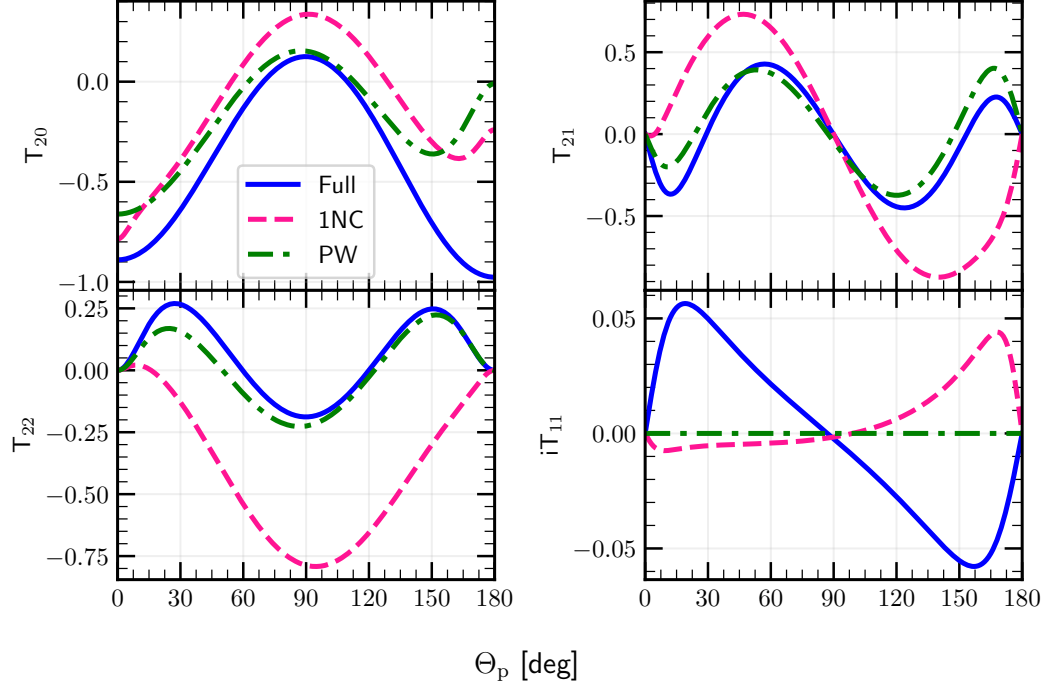


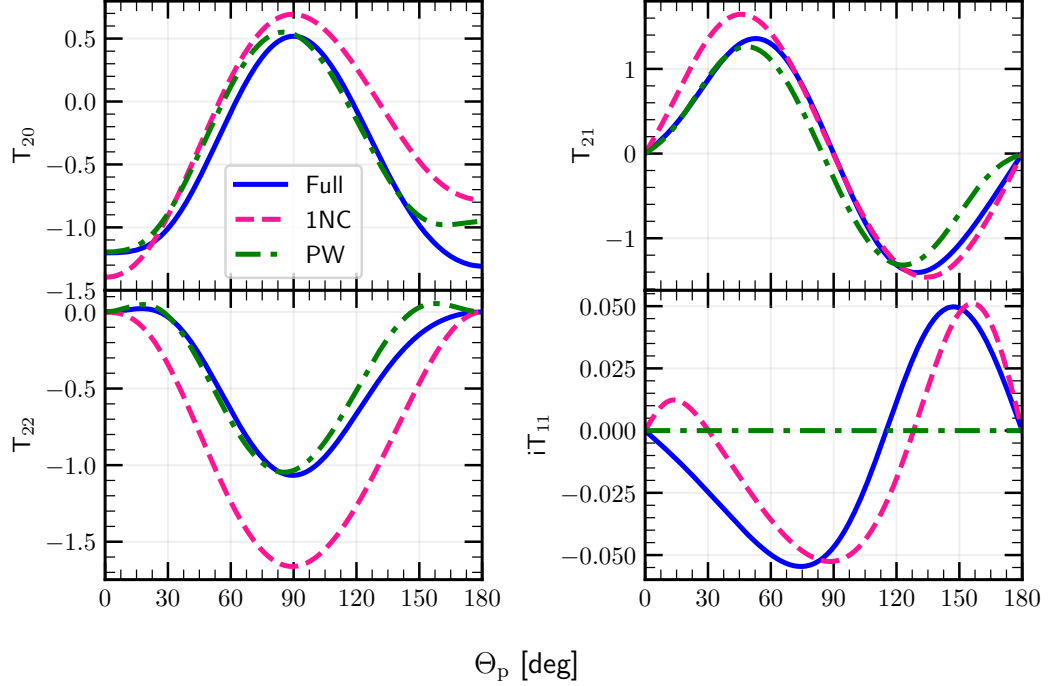
Figure 3.10: Tensor analyzing power components T_{20} , T_{21} , T_{22} and iT_{11} as a functions of the outgoing proton angle θ_p (in the center of mass frame) at $E_\gamma = 30$ MeV. Similarly to Fig. 3.4b predictions obtained with chiral $N^4\text{LO}^+$ potential and $\Lambda = 450$ MeV are presented for each component. Blue solid line is a best predictions we have (plane-wave plus rescattering parts, 1NC + Siegert), pink dashed line shows predictions obtained with single-nucleon current only (without Siegert contributions) and green dashed-dotted line is a prediction with plane-wave part only - without rescattering.

energy 60 MeV the maximum value is around 2.5% (at $\theta = 115^\circ$).

Regarding the correspondance to experimental data, we can clearly see that for the lower energy predictions are almost perfectly overlapping with experimental point (and error bars). Few points are laying outside the predictions but it can be caused by experimental issues. For 60 MeV, experimental data points are constantly below prediction curves (especially in the middle of angles range). It seems that some systematic uncertainty is presented in predictions and multiplication by some factor (presumably less than 1) could help predictions be more similar to experimental data.

On the Fig. 3.23 I present dependence of the asymmetry Σ_γ on the photon's energy with fixed value of the outgoing proton's angle $\theta_p = 90^\circ$ (following the data given at [?] and [?]). It is noticeable that with increasing energy, the prediction curve becomes more and more above the experimental data. This trend was also observed in angular dependence of the asymmetry at 60 MeV so I can assume that within our framework, Σ_γ is sensitive to the initial photon's energy and some contributions are missing in order to prepare good predictions at higher energies. From the Fig. 3.23 we can say that large discrepancy with data starts appearing after 35 MeV.

The proton polarization is demonstrated on the Fig. 3.24 for the photon's energy 30 MeV(a) and 100 MeV(b). In this case even higher energy such as 100 MeV does not reveal neither slower convergence with respect to the chiral order no stronger cutoff dependence. Figures for both energies show that only next-to-leading order brings rela-


 Figure 3.11: The same as on Fig. 3.10 but for $E_\gamma = 100$ MeV

tively high contribution while taking into account each subsequent order does not change predictions largely. In the case of cutoff dependence, we see that curves for each value of Λ are very close to each other. The standard deviation of the predictions with respect to the cutoff parameter has maximal value 1.94% at $E_\gamma = 30$ MeV and 3.2% at 100 MeV. The dependence is slightly stronger for higher energy, but these values are comparable.

Predictions for the neutron polarization at energy 2.75 MeV and 100 MeV are on the Fig. 3.25. The choice of energy is conditioned by the availability of experimental data. In case of $E_\gamma = 2.75$ MeV (Fig. 3.25a), we can see that predictions reflect the behavior of experimental data points qualitatively, having more or less constant offset of the values. Similar offset was obtained also in predictions at [?], where various approaches were presented. Interesting is that predictions clearly show symmetrical form of the curve, while in the experimental data have some deviations from symmetrical form. It can be a sign that some problem with data can be in this case (taking into account also that experiment had been done in 196) as well as inaccuracy in theoretical models.

At the energy $E_\gamma = 100$ MeV (Fig. 3.25b), the difference with experimental data does not look like a systematic shift and deviations look like random. For most of data points, predicted values are within error bars and only some of points (e.g. around 50°) have prediction completely out of measured data. Nevertheless, these data points look like being out of general trend and may be a result of unprecise measurement.

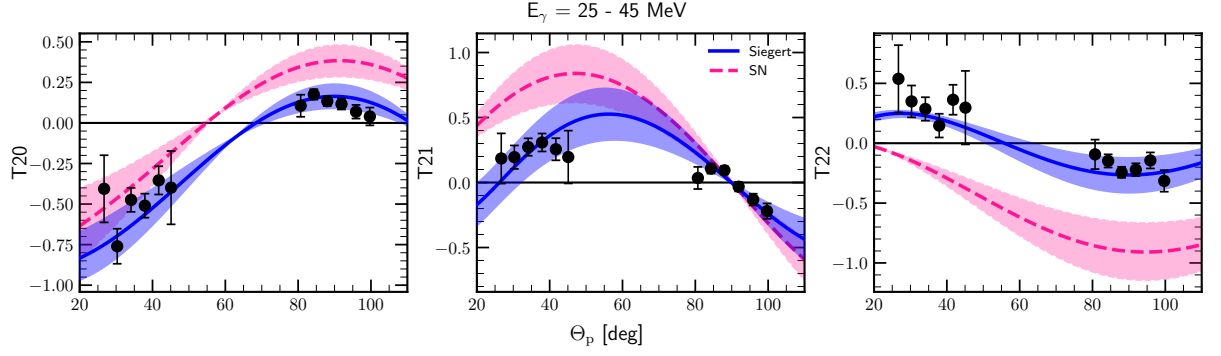


Figure 3.12: Tensor analyzing powers T_{20} , T_{21} and T_{22} as a functions of the outgoing proton angle θ_p (in the center of mass frame). Solid blue line is a mean value of my predictions obtained with a SMS potential at $N^4\text{LO}^+$ chiral order and with $\Lambda = 450$ MeV at energy values from 25 to 45 MeV and where SN current was used together with Siegert approach. Pink dashed line is similar prediction but with SN only. The corresponding bands show the deviation of predictions in the regarded energy region. Filled circles are experimental data from [?] for the analogous energy span.

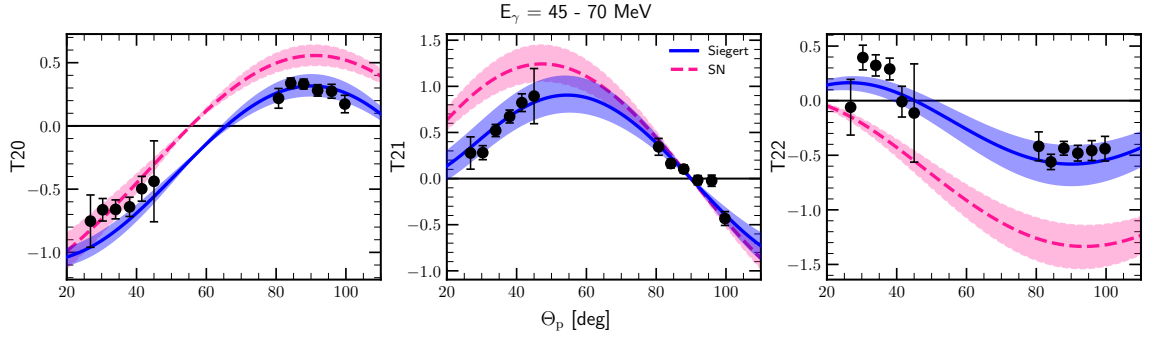


Figure 3.13: The same as on the Fig. 3.12 but for energy bin 45 – 70 MeV

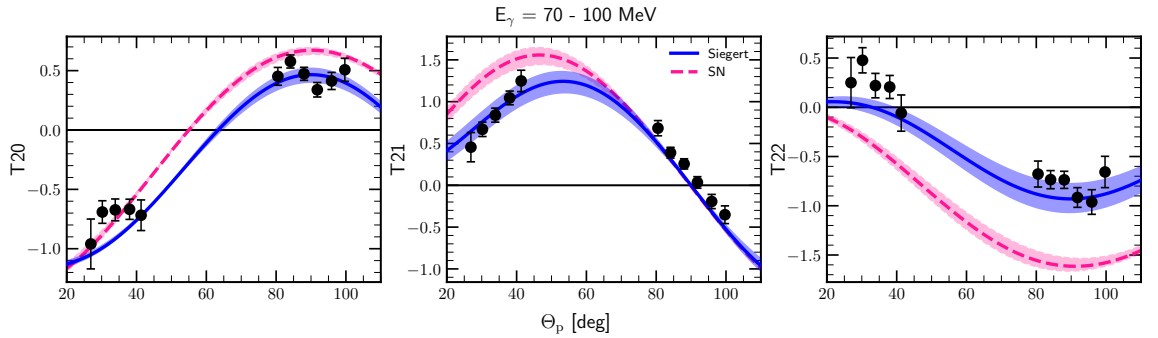


Figure 3.14: The same as on the Fig. 3.12 but for energy bin 70 – 100 MeV

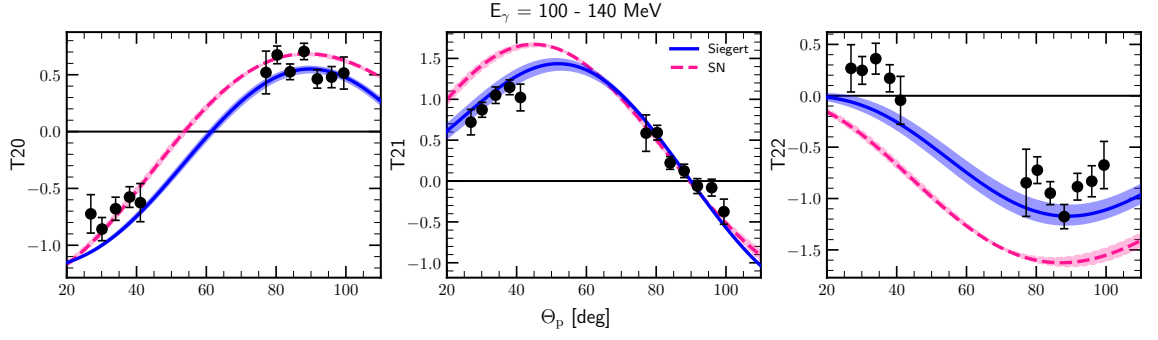


Figure 3.15: The same as on the Fig. 3.12 but for energy bin 100 – 140 MeV

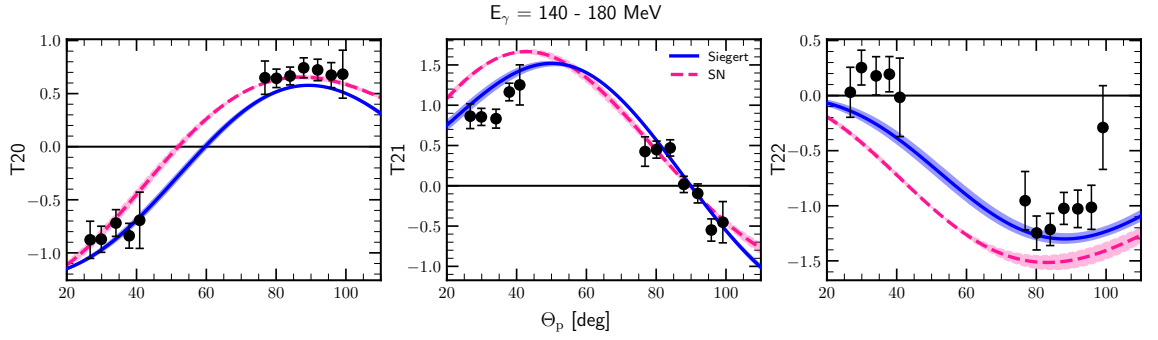


Figure 3.16: The same as on the Fig. 3.12 but for energy bin 140 – 180 MeV

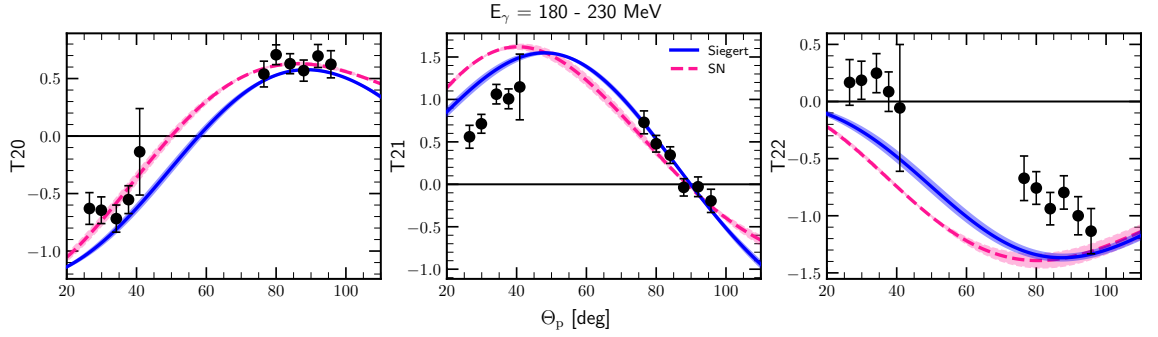


Figure 3.17: The same as on the Fig. 3.12 but for energy bin 180 – 230 MeV

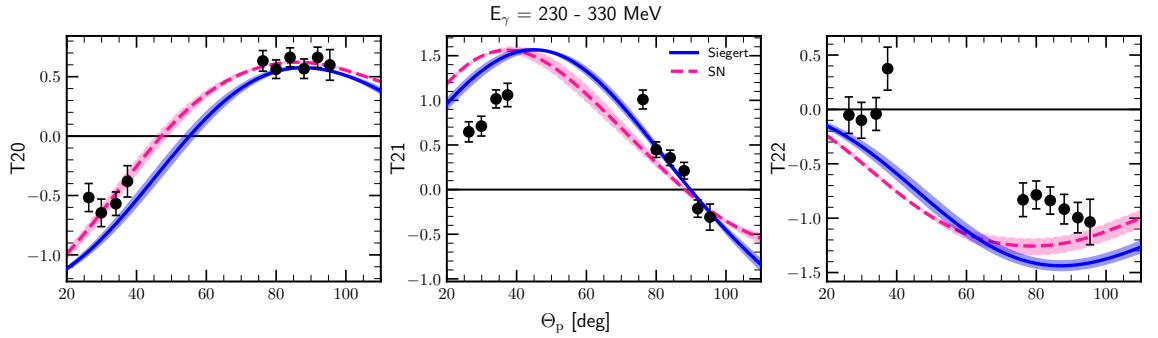


Figure 3.18: The same as on the Fig. 3.12 but for energy bin 230 – 330 MeV

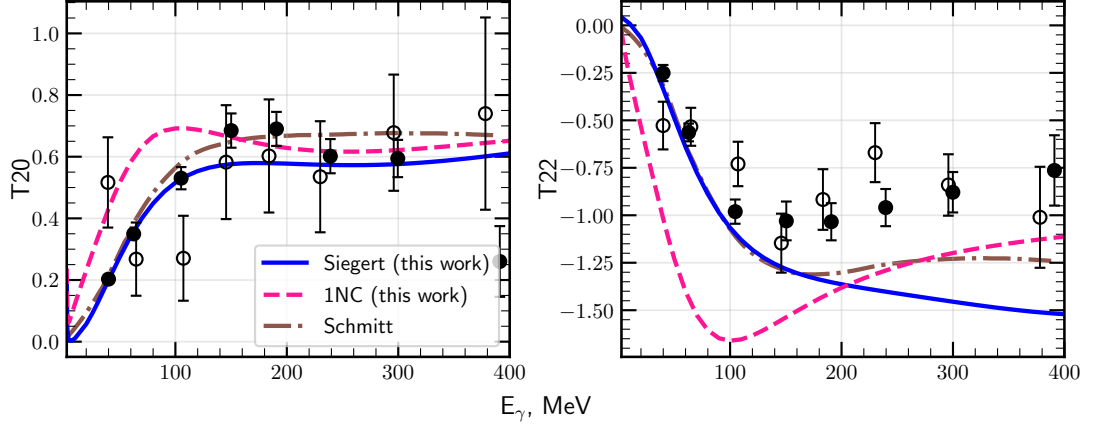


Figure 3.19: Tensor analyzing powers T_{20} and T_{22} as a functions of the photon energy E_γ with fixed outgoing proton angle $\theta_p = 88^\circ$ (in the center of mass frame). My predictions (blue solid line) are obtained with SMS potential at chiral order $N^4\text{LO}^+$ and with cutoff parameter $\Lambda = 450$ MeV with 2NC contributions included via Siegert theorem, dashed pink line show prediction obtained without 2NC contributions. Dashed-dotted brown line presents calculations from [?]. Experimental data is taken from [?] (filled circles) and [?] (empty circles).

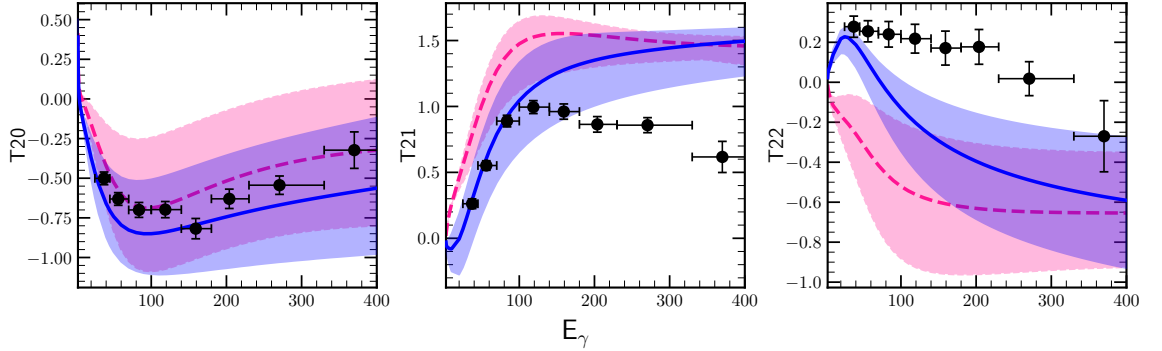


Figure 3.20: Tensor analyzing powers T_{20} , T_{21} and T_{22} as a functions of the photon's energy within the outgoing proton's angle range $24^\circ - 48^\circ$ (in the center of mass frame). Solid blue line is a mean value of my predictions obtained with SMS potential at $N^4\text{LO}^+$ chiral order and with $\Lambda = 450$ MeV at energy values from 25 to 45 MeV within a given angles range and where SN current was used together with Siegert approach. Pink dashed line is similar prediction but with SN only. The corresponding bands show the deviation of predictions in the regarded energy region. Filled circles are experimental data from [?] for the analogous energy span.

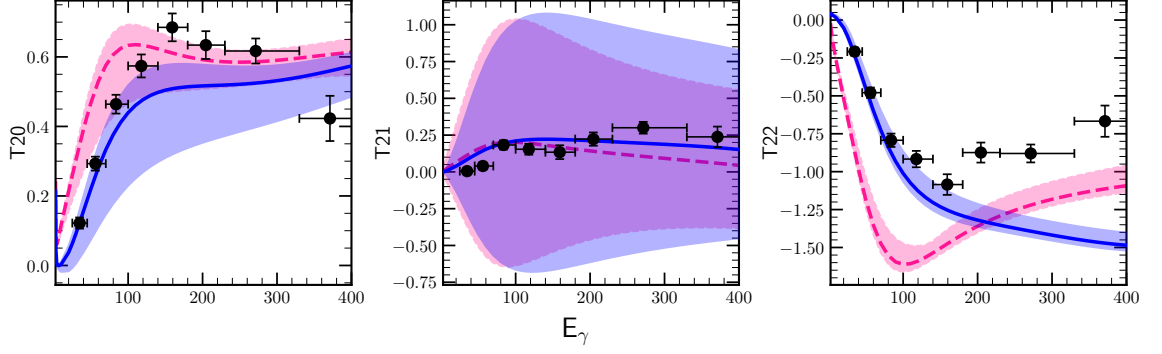
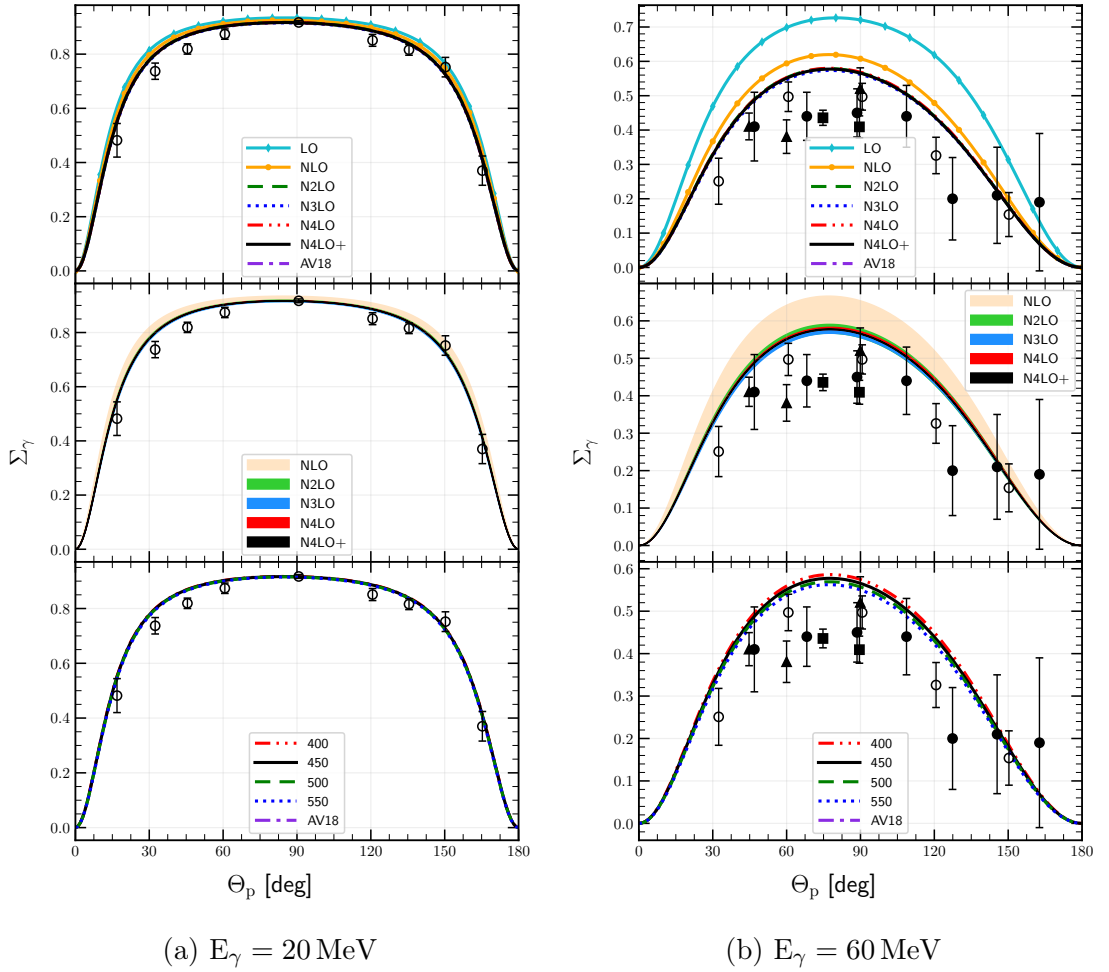

 Figure 3.21: The same as on the Fig. 3.20 but for the angles' range $70^\circ - 102^\circ$.


Figure 3.22: The photon asymmetry Σ_γ as a function of the outgoing proton angle in the center of mass frame for the photon's energy 30 MeV(a) and 100 MeV(b). Top row presents results obtained using potential with different chiral orders (from LO to $N^4\text{LO}^+$) with cutoff parameter $\Lambda = 450 \text{ MeV}$. The middle row shows truncation errors for each chiral order starting from NLO and bottom presents a cutoff dependency (chiral potential $N^4\text{LO}^+$). Filled circles are experimental data from [?], empty circles - from [?], filled squares - from [?] and triangles are from [?]. For the sake of comparison, predictions obtained with AV18 potential are on figures as well.

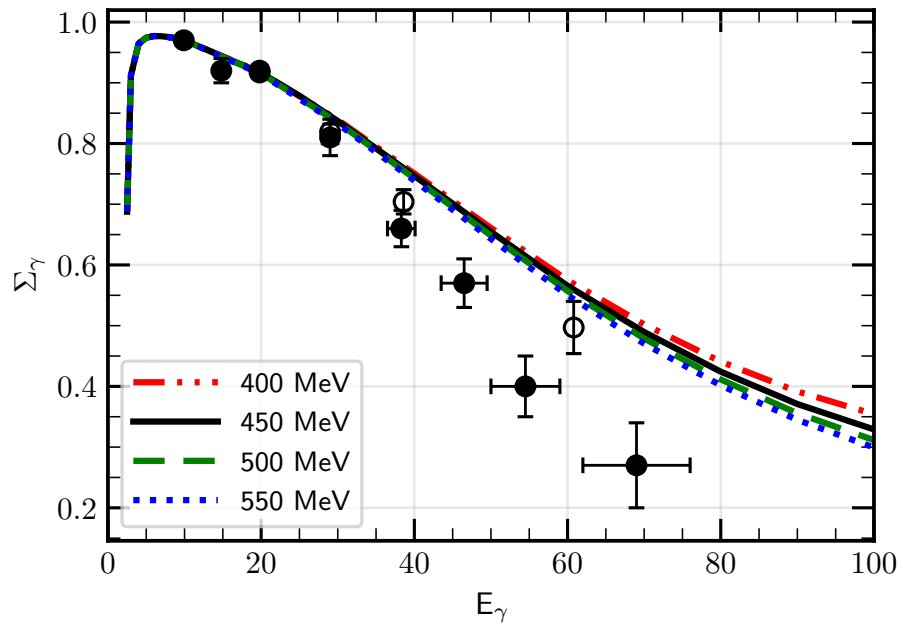


Figure 3.23: The photon asymmetry Σ_γ as a function of the photon energy with fixed outgoing proton angle $\theta_p = 90^\circ$. Each curve corresponds to the particular value of the cutoff parameter and chiral potential used here is $N^4\text{LO}^+$. Filled circles are experimental data from [?], empty circles - from [?].

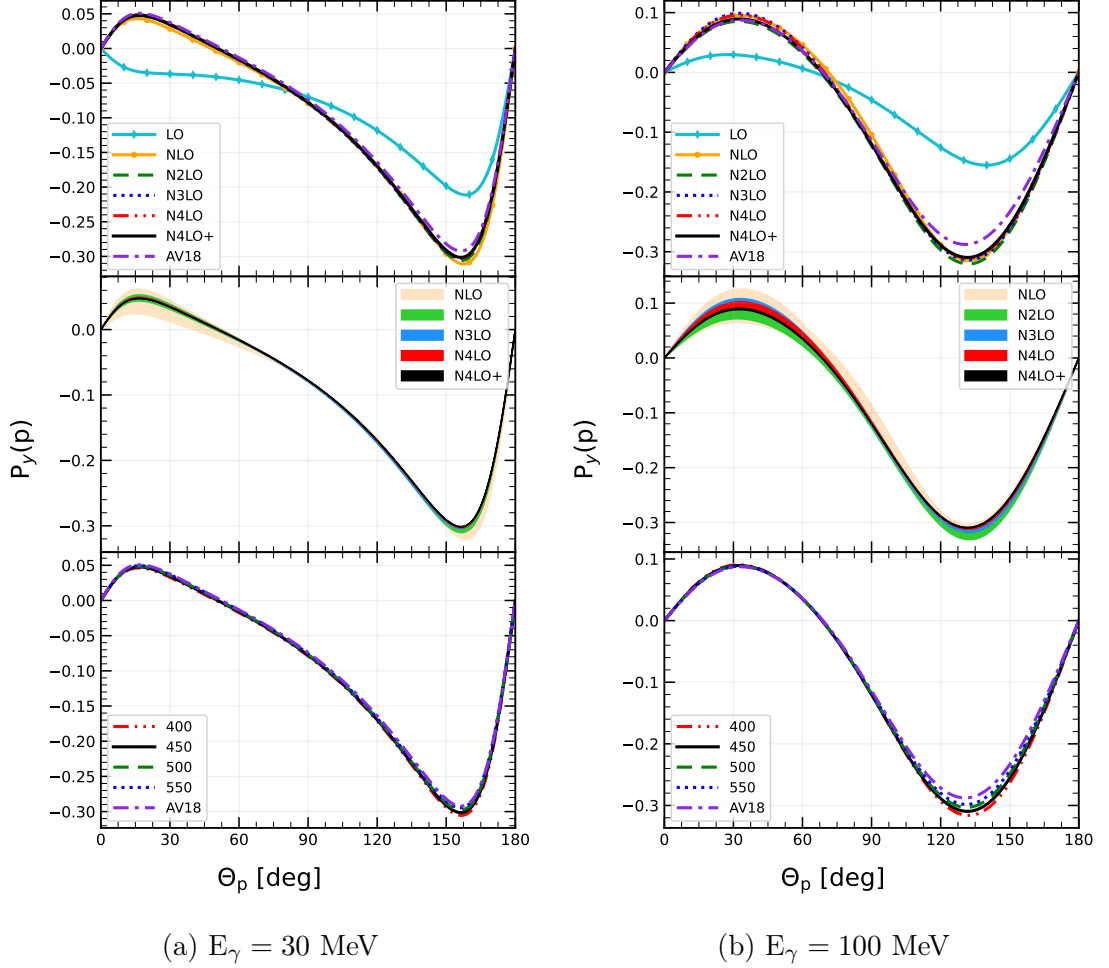


Figure 3.24: Proton polarisation $P_y(p)$ as a function of the outgoing proton angle in the center of mass frame for the photon's energy 30 MeV (a) and 100 MeV (b). Top figure presents results obtained using potential with different chiral orders (from LO to $N^4\text{LO}^+$) with cutoff parameter $\Lambda = 450$ MeV. The middle pane shows truncation errors for each chiral order starting from NLO and bottom figure presents a cutoff dependency (chiral potential $N^4\text{LO}^+$). For the sake of comparison, predictions obtained with AV18 potential are on figures as well.

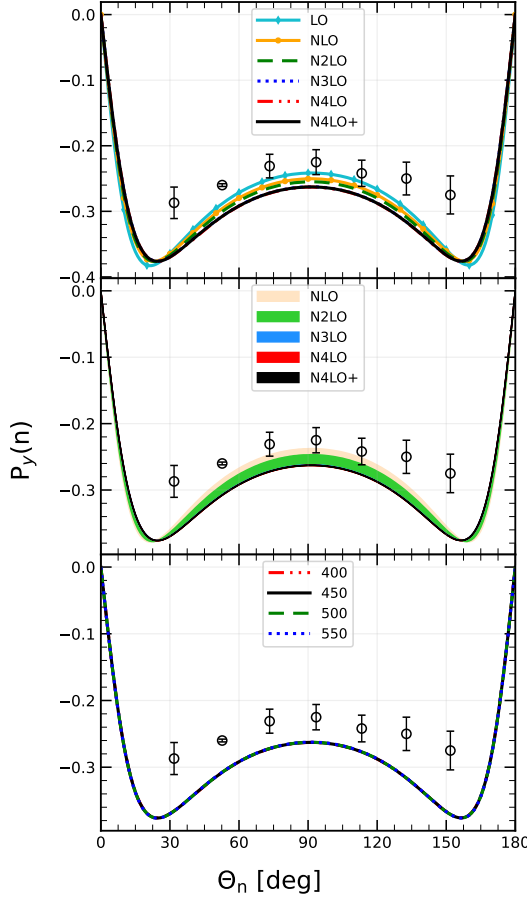
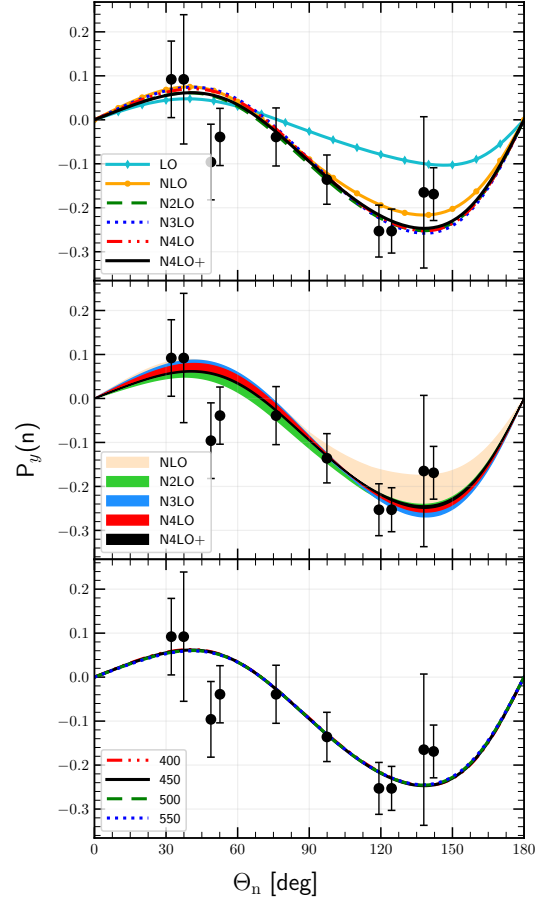

 (a) $E_\gamma = 2.75$ MeV

 (b) $E_\gamma = 100$ MeV

Figure 3.25: Neutron polarisation $P_y(n)$ as a function of the outgoing neutron angle in the center of mass frame for the photon's energy 2.75 MeV(a) and 100 MeV(b). Top row presents results obtained using potential with different chiral orders (from LO to $N^4\text{LO}^+$) with cutoff parameter $\Lambda = 450$ MeV. The middle pane shows truncation errors for each chiral order starting from NLO and bottom figure presents a cutoff dependency (chiral potential $N^4\text{LO}^+$). Experimental data is from [?] (empty circles) and [?] (filled circles).

3.2 Helium photodisintegration

3.2.1 3N photodisintegration

In this section I will demonstrate predictions for observables from ${}^3\text{He} \rightarrow p + p + n$ process.

On the Fig. 3.26 I demonstrate a differential cross section $\frac{d^5\sigma}{d\Omega_1 d\Omega_2}$ as a function of the S curve position. The photon's energy is $E_\gamma = 30$ MeV and the kinematic configuration $\theta_1 = 15^\circ$, $\phi_1 = 0^\circ$, $\theta_2 = 15^\circ$, $\phi_2 = 180^\circ$; predictions have been obtained without 3NF. We see that only NLO and N²LO introduce relatively large truncation error. The maximal width of a band for NLO is 37.6% at $S = 10$ MeV, for N²LO it is 12.4% at the same point and it is gradually decreasing coming to 0.13% at N⁴LO⁺. The cutoff spread around maxima values is less than 3% and it is 0.78% at the minimum point ($S = 10$ MeV).

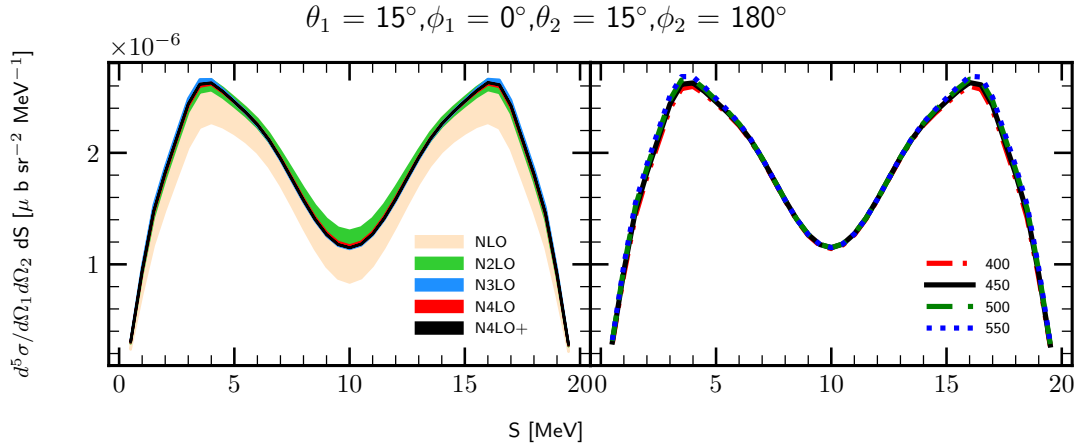


Figure 3.26: The five-fold differential cross section for the photon energy $E_\gamma = 30$ MeV for the kinematic configuration $\theta_1 = 15^\circ$, $\phi_1 = 0^\circ$, $\theta_2 = 15^\circ$, $\phi_2 = 180^\circ$. The left figure presents truncation error bands obtained using potential with different chiral orders (from NLO to N⁴LO⁺) with cutoff parameter $\Lambda = 450$ MeV. The right figure presents a cutoff dependency (chiral potential N⁴LO⁺). Results are obtained with two-nucleon force only.

With larger energy $E_\gamma = 100$ MeV demonstrated on the Fig. 3.27, both truncation error and cutoff spread become larger. The truncation band at the maximum point $S = 10$ MeV for NLO is 55.0% decreasing to 2.2% at N⁴LO⁺ which is around 3 times larger than it was in predictions with $E_\gamma = 30$ MeV. The cutoff spread also becomes larger with increasing energy value: 9.0% at the same (maximum) point which is also ~ 3 times larger than the one we observed for lower energy.

Next I come to other angular configurations for $E_\gamma = 100$ MeV, starting with $\theta_1 = 75^\circ$, $\phi_1 = 75^\circ$, $\theta_2 = 75^\circ$, $\phi_2 = 105^\circ$ demonstrated on Fig. 3.28. Similar predictions but with 3NF contribution is presented on Fig. 3.29. It seems that 3NF does not change much the convergence with respect to the chiral order: truncation error band at the point of maximum $S = 35$ MeV (N⁴LO⁺) is 1.11% and 1.16% with and without 3NF respectively. So it is almost the same, meaning that 3NF contribution does not affect chiral order convergence much.

The cutoff dependence, in turn, is affected by 3NF presence. Predictions with 2NF only have 13.7% spread at the same maximum point, while predictions with 3NF have 1.23%, so the difference is tremendous.

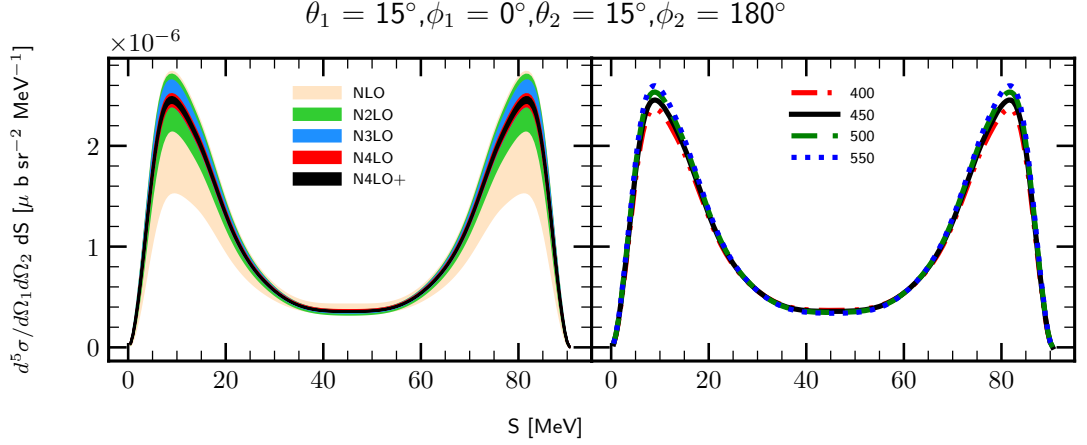
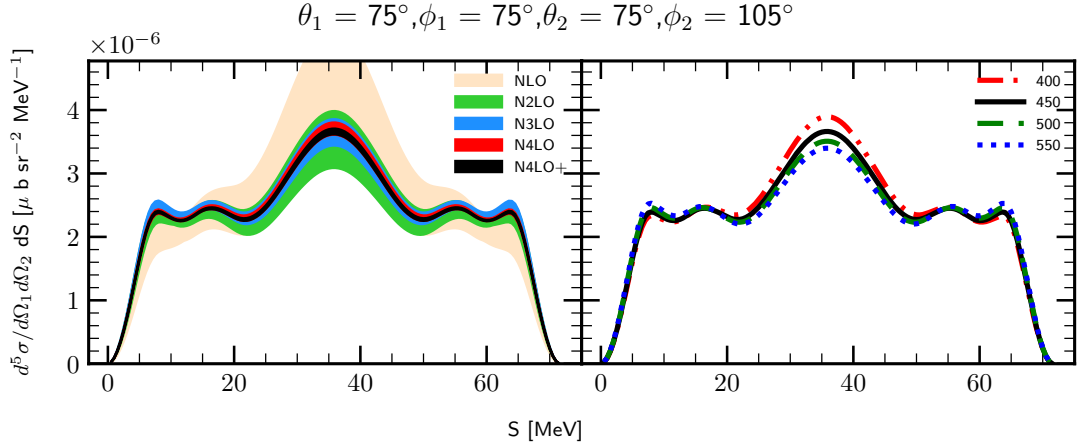

 Figure 3.27: The same as on Fig. 3.26 but for the photon energy $E_\gamma = 100$ MeV


Figure 3.28: The same as on the Fig. 3.27 but for the different kinematic configuration.

Similar trends present in other configurations, demonstrated for the comparison: Figs.3.30 and 3.31, Figs.3.32 and 3.33, Figs.3.34 and 3.35.

The semi-inclusive differential cross section $\frac{d^3\sigma}{d\Omega_p dE_p}$ as a function of the outgoing protons energy E_p is demonstrated on the Fig. 3.36 (for $E_\gamma = 30$ MeV) and Fig. 3.37 (for $E_\gamma = 100$ MeV). Each figure consists of subfigures where each row presents results for a proton angles $\theta_p = 10^\circ, 50^\circ, 90^\circ, 130^\circ$ and 170° . The left part of each subfigure shows a chiral order dependence while the right - cutoff dependence.

At the photon's energy 30 MeV the chiral dependence is relatively weak: at the maximum point ($E_p \simeq 3.8$ MeV) the relative difference varies between 12 % and 28 % at LO for different angles. This difference decreases with each subsequent order resulting in 0.15 % at N^4LO+ . At the energy $E_\gamma = 100$ MeV truncation errors are larger: at the $E_p \simeq 1.46$ MeV the discrepancy is around 40 % (NLO), 15 % (N2LO), coming to 1.5 % at N^4LO+ .

The cutoff uncertainty at $E_\gamma = 30$ MeV is around 2 % and at $E_\gamma = 100$ MeV is around 8 % for all angles and at the same values of E_p as regarded above.

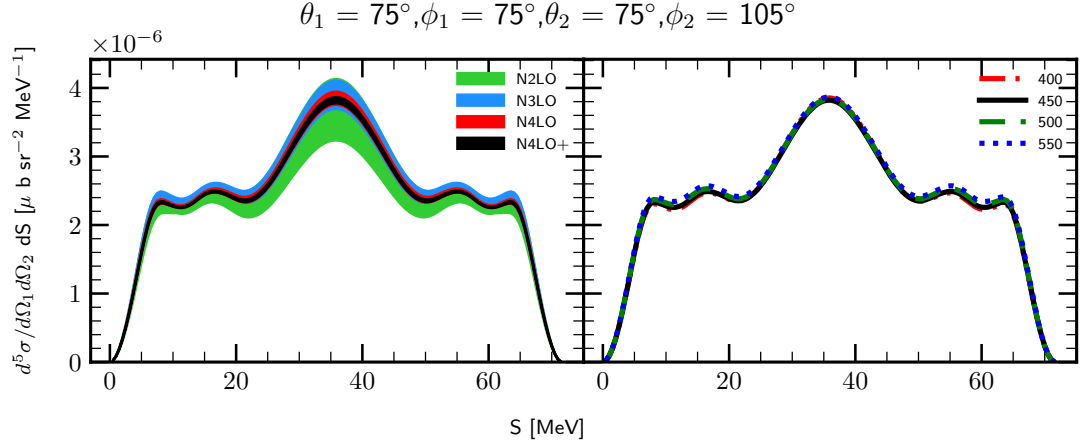


Figure 3.29: The same as on the Fig. 3.28 but with three-nucleon force.

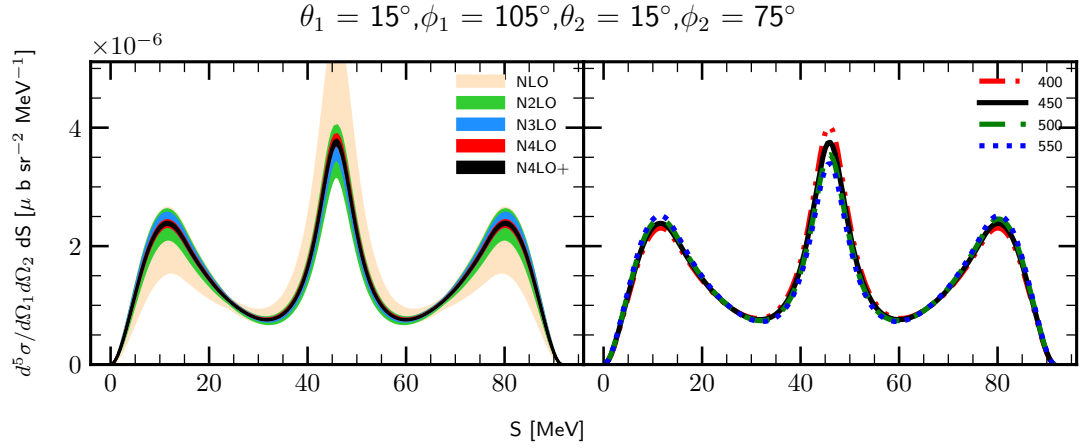


Figure 3.30: The same as on the Fig. 3.28 but for the different kinematic configuration.

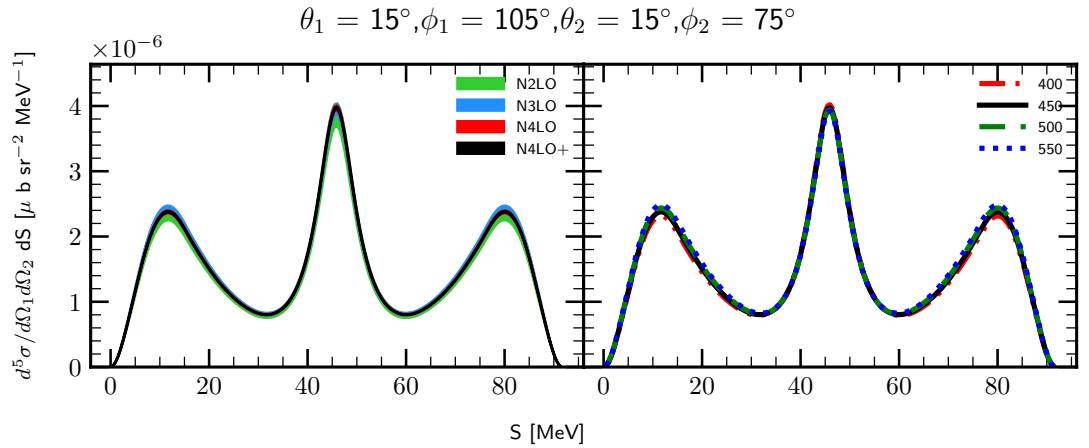


Figure 3.31: The same as on the Fig. 3.30 but but with three-nucleon force.

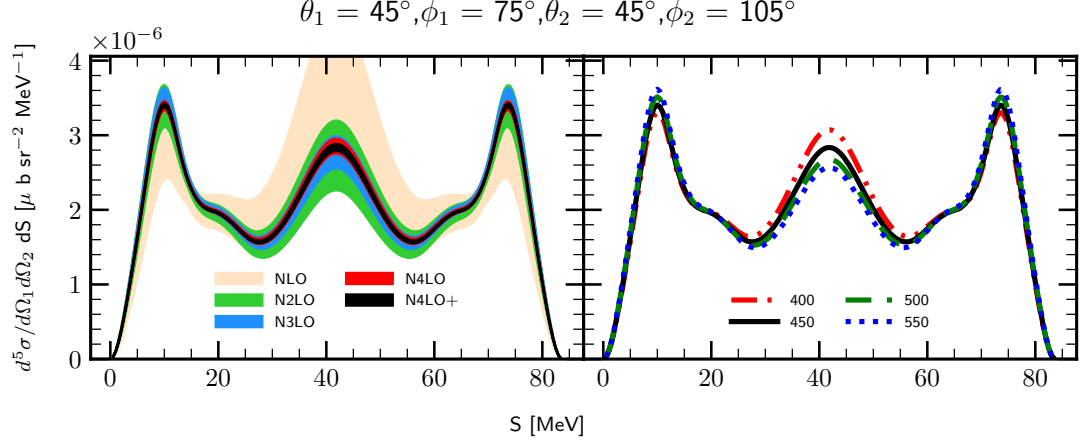


Figure 3.32: The same as on the Fig. 3.30 but for the different kinematic configuration.

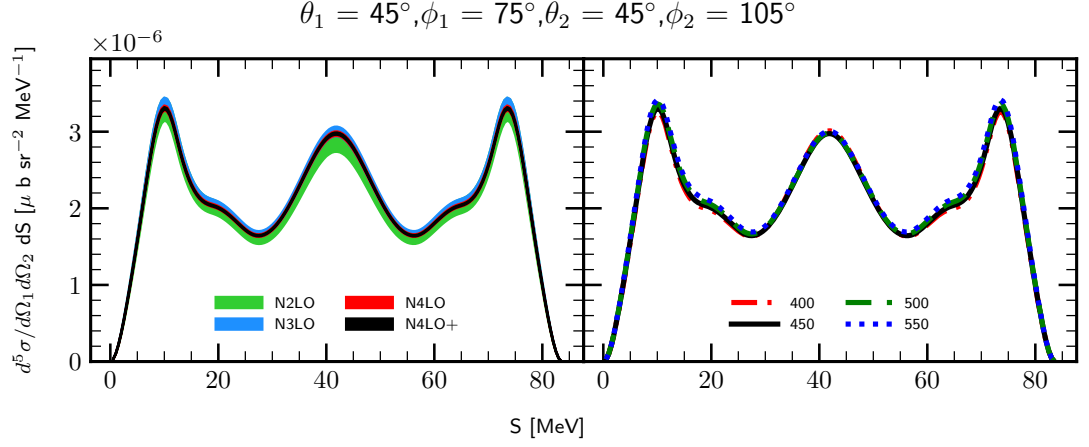


Figure 3.33: The same as on the Fig. 3.32 but but with three-nucleon force.

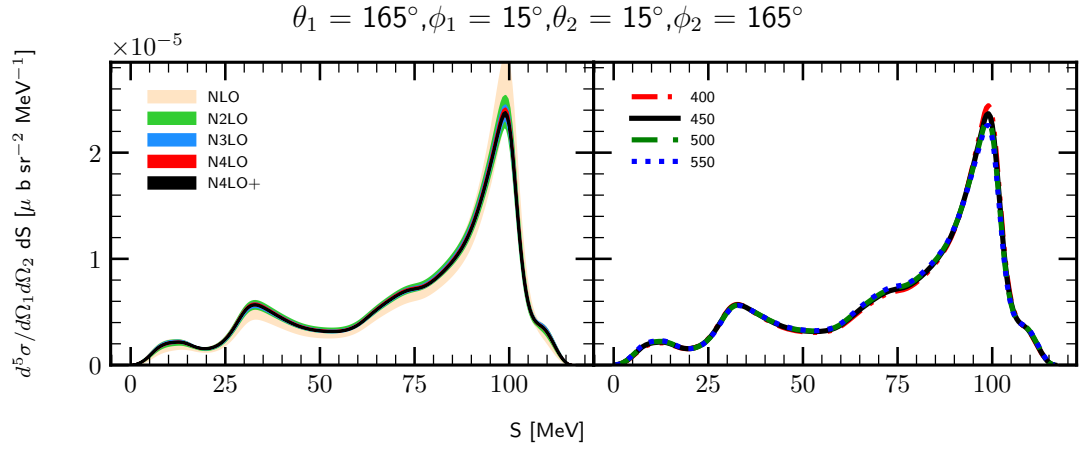


Figure 3.34: The same as on the Fig. 3.32 but for the different kinematic configuration.

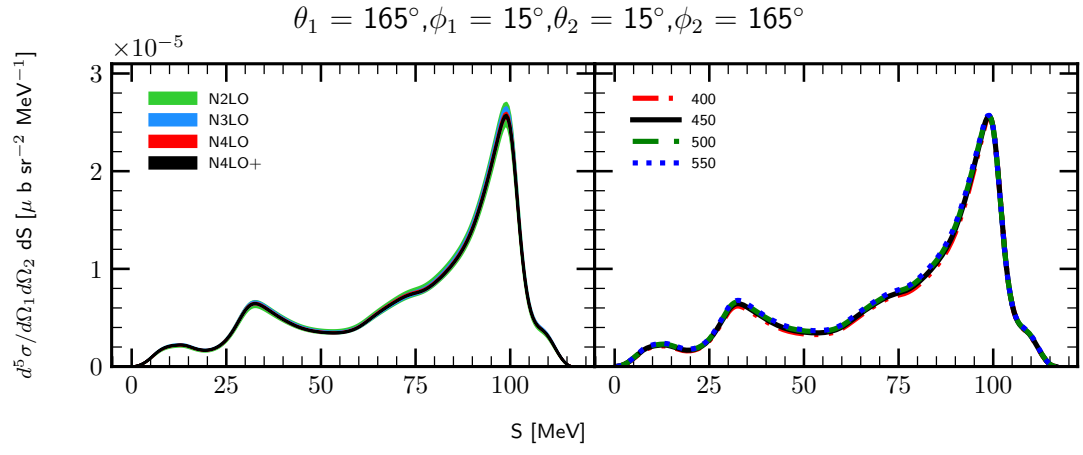


Figure 3.35: The same as on the Fig. 3.34 but but with three-nucleon force.

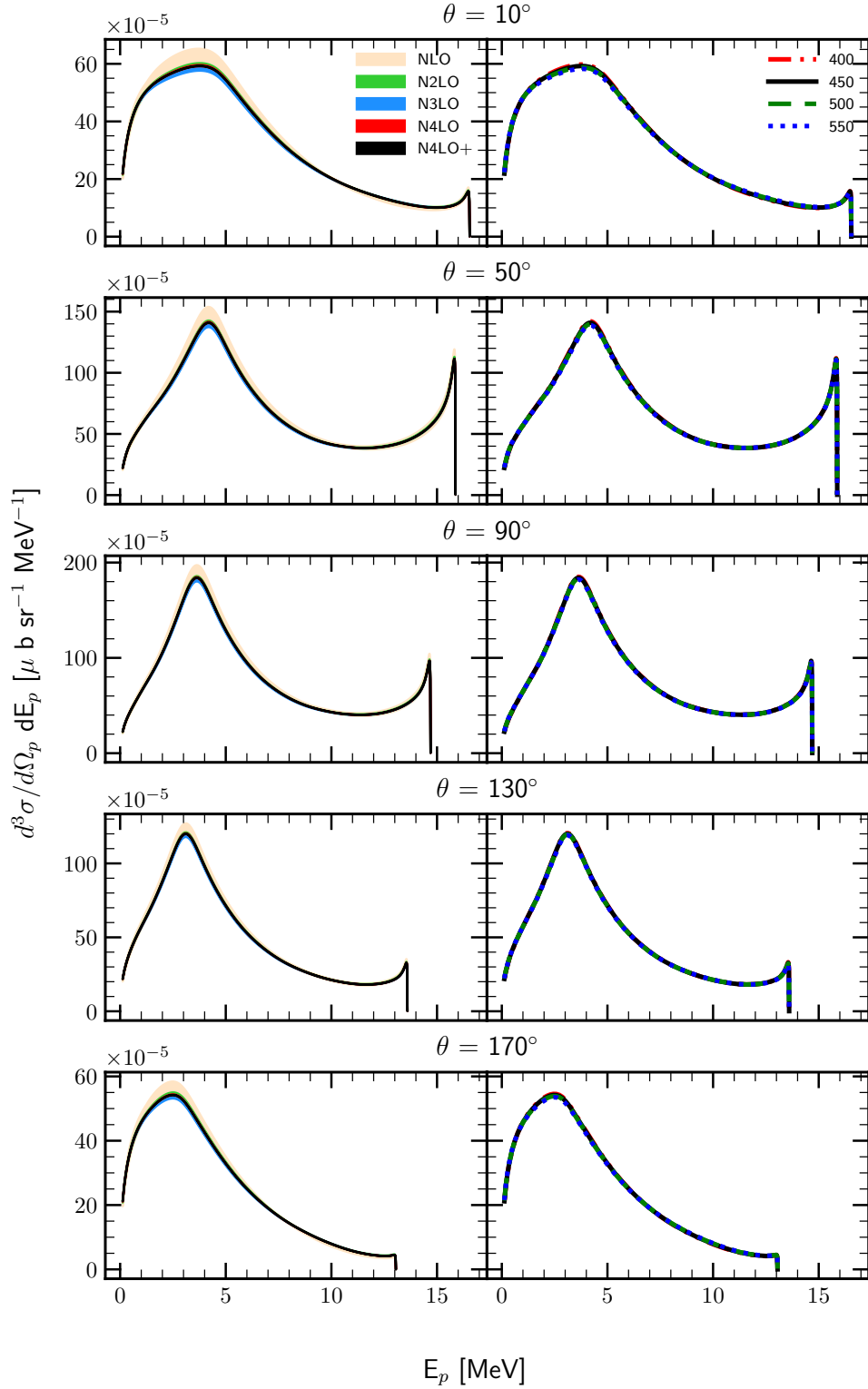
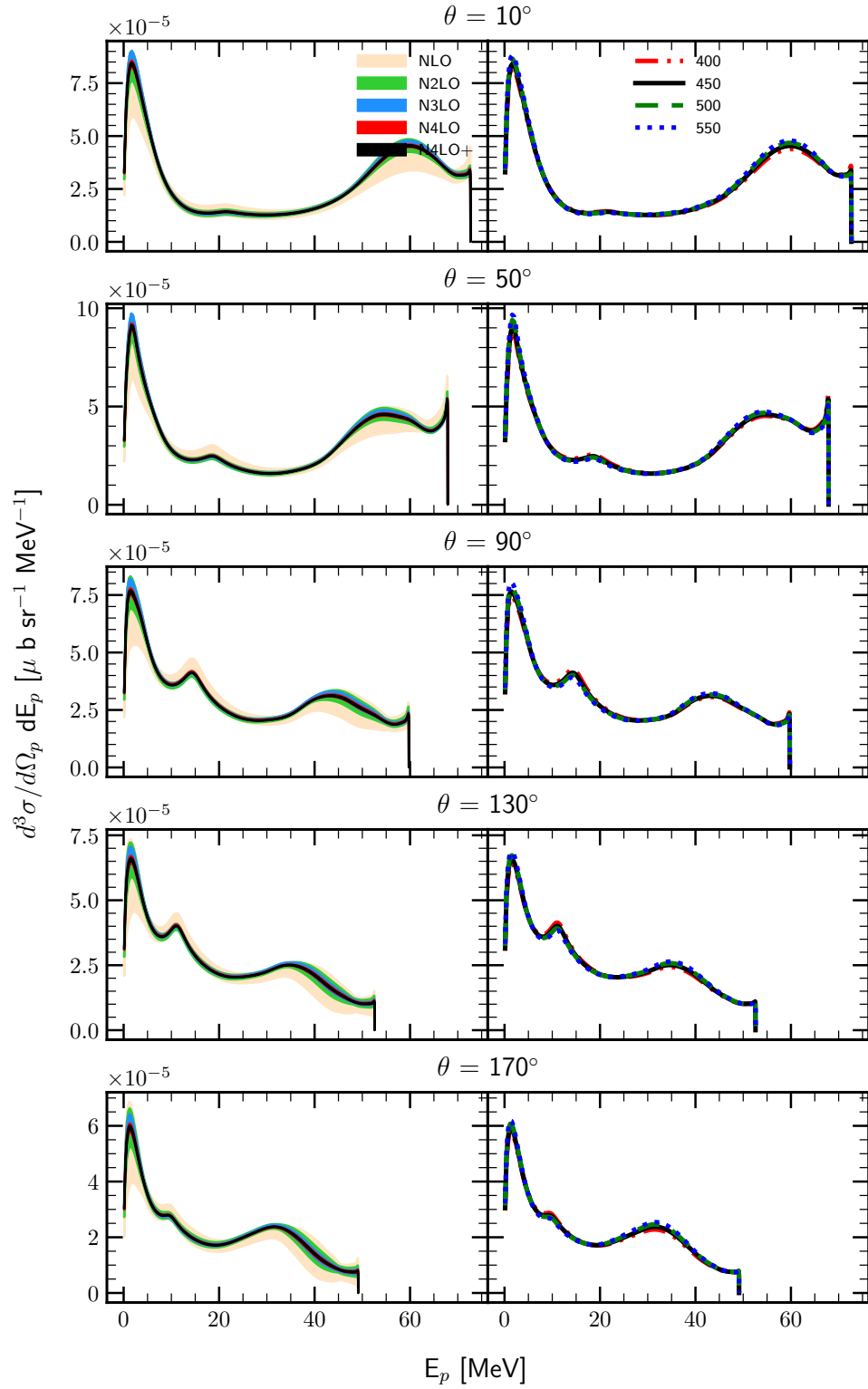


Figure 3.36: The semi-inclusive differential cross section $\frac{d^3\sigma}{d\Omega_p dE_p}$ at $E_\gamma = 30$ MeV as a function of outgoing proton's energy E_p . Each row represent predictions for different values of the outgoing proton's angle θ_p : 10°, 50°, 90°, 130° and 170°. Each column has similar lines and bands definitions as it was for exclusive cross section. Predictions have been obtained without 3NF.


 Figure 3.37: The same as on Fig. 3.36 but for $E_\gamma = 100$ MeV

3.2.2 D-n photodisintegration

The differential cross section $d\sigma/d\Omega_d$ for the ${}^3\text{He} + \gamma \rightarrow d + n$ reaction is presented on the Fig. 3.38 (for the photon's energy $E_\gamma = 30$ MeV) and on the Fig. 3.39 (for the photon's energy $E_\gamma = 100$ MeV). We see that both truncation and cutoff uncertainties are larger with increasing photon's energy. The relative spread of the truncation error at the maximum point ($\theta_p = 105^\circ$) for the lower energy is 0.05 % at N⁴LO⁺, while for the larger energy similar spread is 0.45 % (at N⁴LO⁺, $\theta_p = 120^\circ$).

The cutoff dependence is also stronger for the larger energy: it is 1.45 % at 30 MeV and 4.01 % at 100 MeV (at the points of maximum).

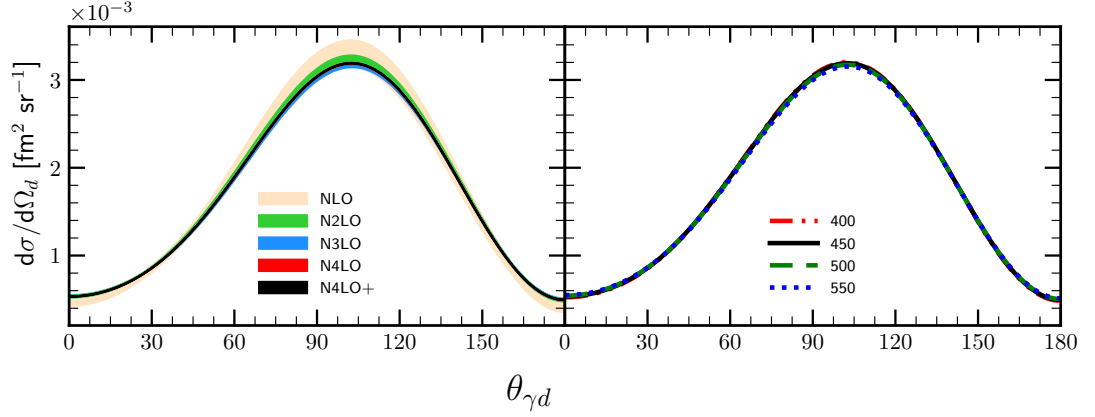


Figure 3.38: Differential cross section for the d-*n* two-body photodisintegration of ${}^3\text{He}$ as a function of the $d\gamma$ angle. The initial photon energy $E_\gamma = 30$ MeV.

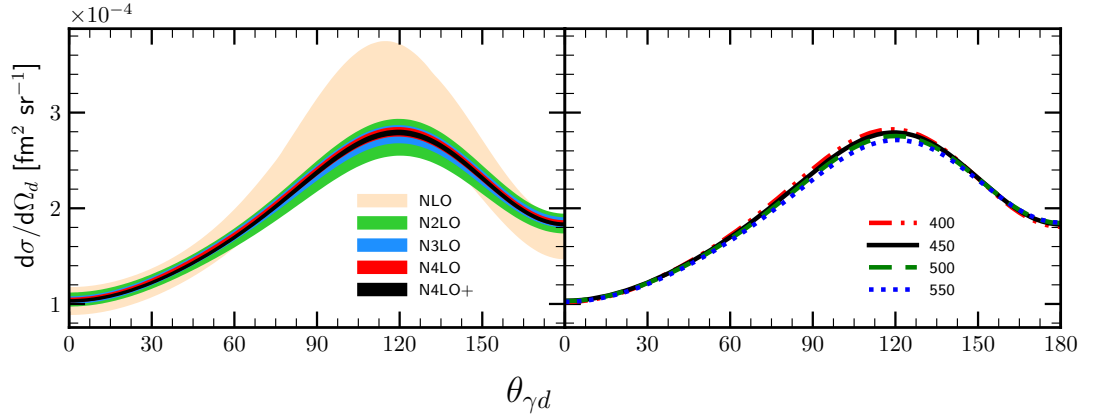


Figure 3.39: The same as on Fig. 3.38 but for the photon energy $E_\gamma = 100$ MeV

3.3 Pion absorption from the lowest atomic orbital

3.3.1 Pion absorption in ${}^3\text{He}$

in Fig. 3.40 and 3.41 the pion absorption rates are presented as a functions of the chiral order with different values of the cutoff parameter (for $\pi^- + {}^3\text{He} \rightarrow p + n + n$ and $\pi^- + {}^3\text{He} \rightarrow n + d$ reactions, respectively). Both figures show that with fixed chiral order the arrangement of values with respect of the cutoff parameter remains the same, namely with increasing Λ , absorption rate decreases. The only exception in both cases appears at N³LO where prediction with $\Lambda = 550$ MeV goes above other predictions. At the next order, N⁴LO, it corrects to the normal arrangement. This behavior may be connected to the 3NF used for the calculation and in order to check that I show a similar figure for a proton radius r_p in Fig. 3.42 calculated with and without 3NF (left and right panels respectively). Results obtained with 3NF show similar deviation at N³LO while data obtained without 3NF does not have that. Nevertheless, the spread of predictions with respect to the cutoff values is much smaller with 3NF and deviation seems to be not crucial as total difference between predictions in this case is very small.

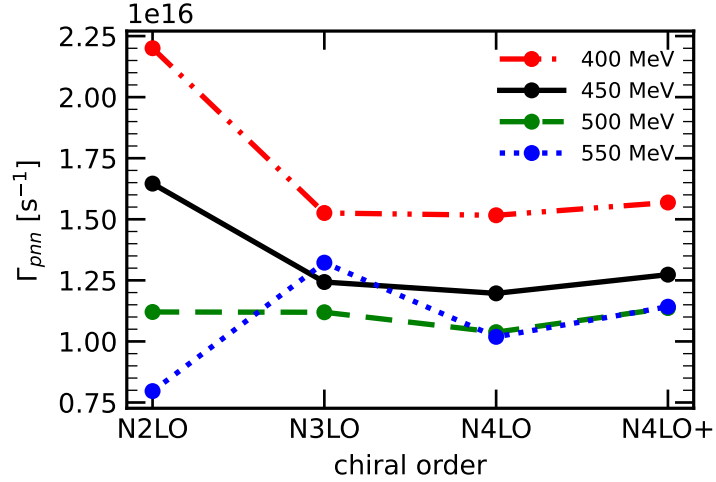


Figure 3.40: Absorption rate for $\pi^- + {}^3\text{He} \rightarrow p + n + n$ reaction as a function of the chiral order with different values of the cutoff parameter Λ . Predictions were obtained with 3NF.

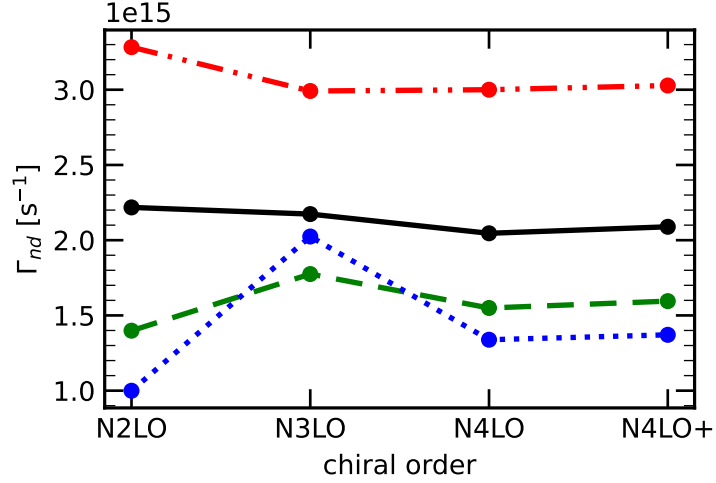
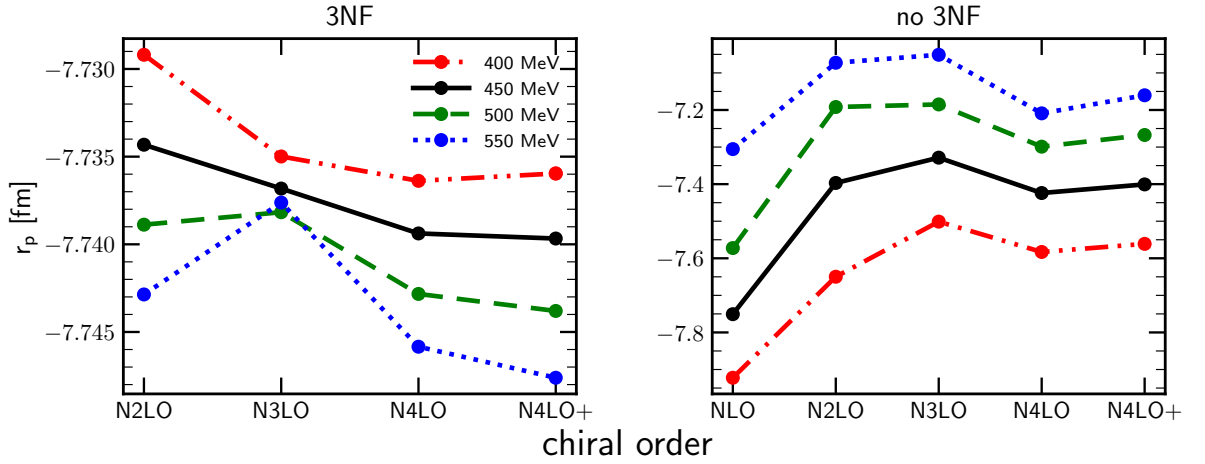
In Figs. 3.43 and 3.44 I show intensity plots for the double differential absorption rates $d^2\Gamma_{pnn}/dE_1dE_2$ for the $\pi^- + {}^3\text{He} \rightarrow p + n + n$ process as functions of the nucleons energies (first nucleon is proton) and of *correct naming* Dalitz coordinates(x and y) respectively.

In Fig. 3.44 coordinates x and y are defined as:

$$\begin{aligned} x &= 3(E_1 + 2E_2 - E)/E, \\ y &= (3E_1 - E)/E, \end{aligned} \tag{3.4}$$

taking the region where $r^2 \equiv x^2 + y^2 \leq 1$.

Each of two figures consists of four panels representing predictions obtained with different values of the cutoff parameter Λ . The difference between predictions which can be noticed with the naked eye - is that area of the central region (corresponding to


 Figure 3.41: The same as in Fig. 3.40, but for $\pi^- + {}^3\text{He} \rightarrow n + d$ reaction.

 Figure 3.42: *check mt3* Proton radius r_p as a function of the chiral order calculated with different values of the cutoff parameter Λ . The radius was calculated with 2NF and 3NF (left panel) and with 2NF only (right panel).

smallest values) becomes larger with increasing Λ . It coheres to what we saw on Fig. 3.40 where total absorption rate was inversely correlated with cutoff parameter. The dominant contribution comes from the region with lowest proton energy values of $E_1 \rightarrow 0$ where both neutrons have similar large values. This is a situation when proton is a spectator while both neutrons share all energy - quasi-free scattering(QFS).

Another region with high absorption rate is neutron-neutron final state interaction (FSI(nn)). It is located at high E_1 when proton gets one third part of total energy while neutrons both get one sixth.

Next I show similar colormaps but for the predictions obtained with plane wave component only (without rescattering part) in Figs. 3.45 and 3.46. Presented plots show that the difference of predictions obtained without rescattering part with full is very large. Predicted values are few times larger and the distribution is completely different. The FSI(nn) region is not presented here in a sense that there is no peak with respect to other values. The QFS region is, on the contrary, It obviously tells us that one has to take into

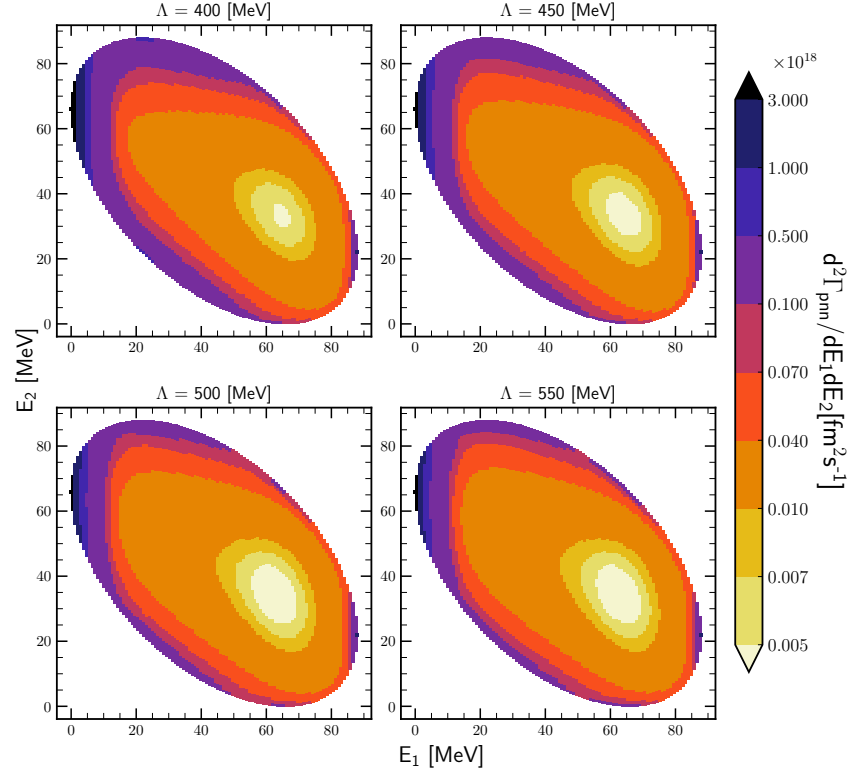


Figure 3.43: Intensity plots for the double differential absorption rates $d^2\Gamma_{pn}/dE_1 dE_2$ for the $\pi^- + {}^3\text{He} \rightarrow p + n + n$ process, obtained using the SMS potential at N^4LO^+ with all contributions possible: plane wave + rescattering, SN + 2N, 2NF+3NF. Each panel present predictions obtained with different values of the cutoff parameter Λ : from 400 MeV (upper left) to 550 MeV (lower right). Nucleon 1 is a proton.

account rescattering pat in order to obtain relevant results.

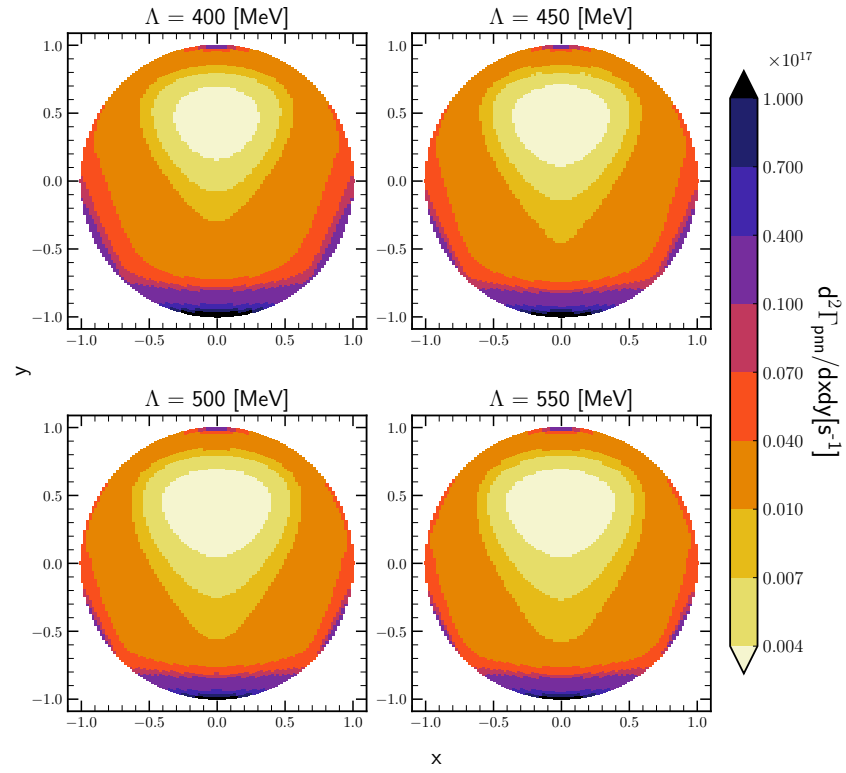


Figure 3.44: The same as in Fig. 3.43 but for the double differential absorption rates $d^2\Gamma_{pn}/dx dy$.

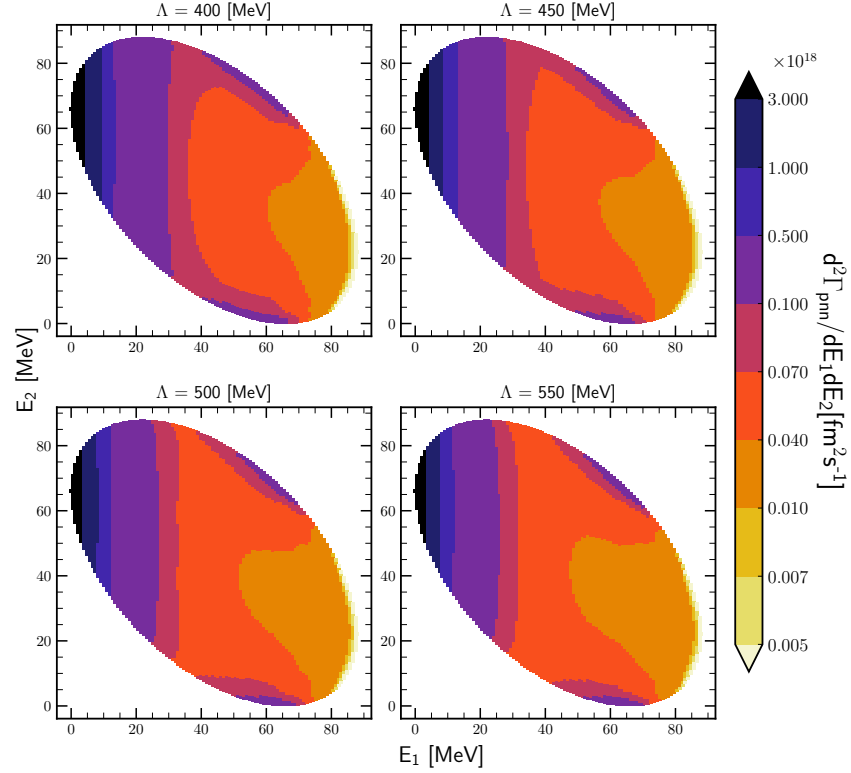


Figure 3.45: Intensity plots for the double differential absorption rates $d^2\Gamma_{pn}/dE_1 dE_2$ for the $\pi^- + {}^3\text{He} \rightarrow p + n + n$ process, obtained using the SMS potential at N^4LO^+ with plane wave part only (without rescattering). All other contributions are the same as in Fig. 3.43: $\text{SN} + 2\text{N}$ and $2\text{NF} + 3\text{NF}$. Each panel present predictions obtained with different values of the cutoff parameter Λ : from 400 MeV (upper left) to 550 MeV (lower right). Nucleon 1 is a proton.

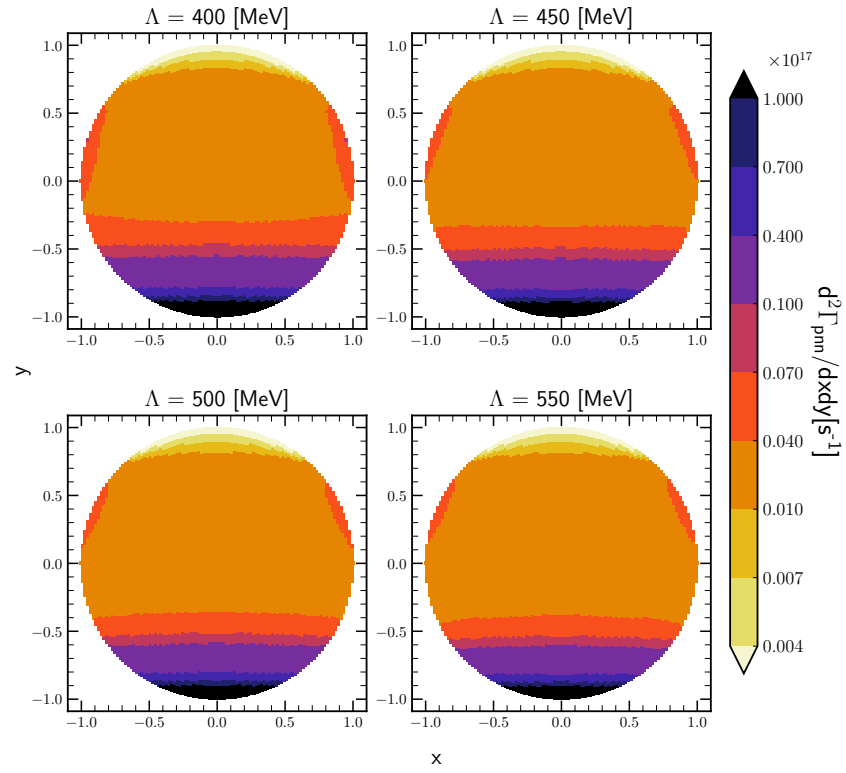


Figure 3.46: The same as in Fig. 3.45 but for the double differential absorption rates $d^2\Gamma_{pnn}/dx dy$.

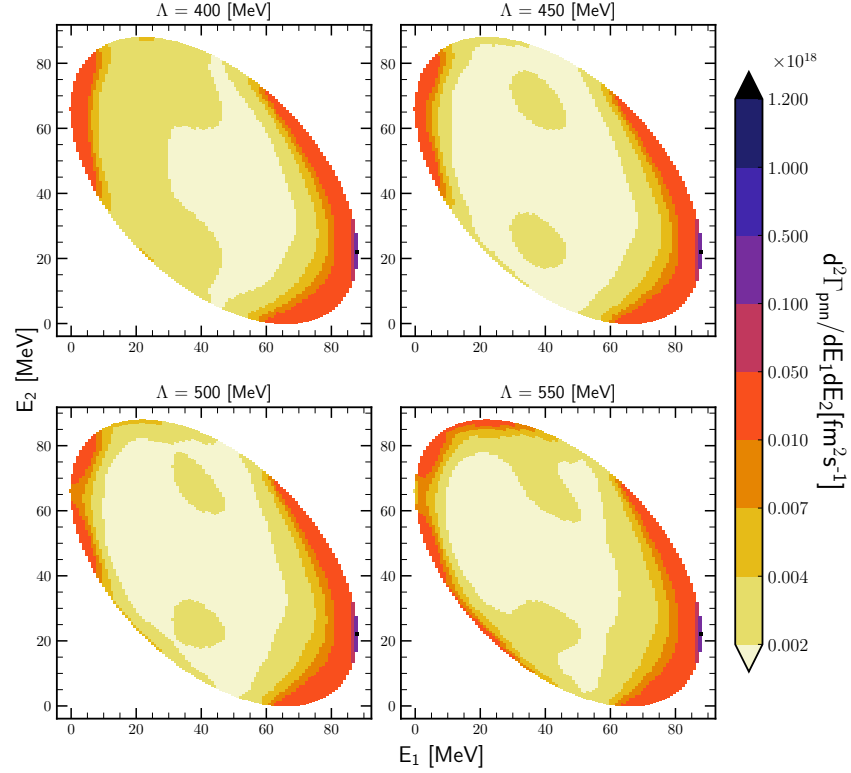


Figure 3.47: Intensity plots for the double differential absorption rates $d^2\Gamma_{pn}/dE_1 dE_2$ for the $\pi^- + {}^3\text{He} \rightarrow p + n + n$ process, obtained using the SMS potential at N^4LO^+ with SN current only (without 2N). All other contributions are the same as in Fig. 3.43: PWIAS+RESC and 2NF+3NF. Each panel present predictions obtained with different values of the cutoff parameter Λ : from 400 MeV (upper left) to 550 MeV (lower right). Nucleon 1 is a proton.

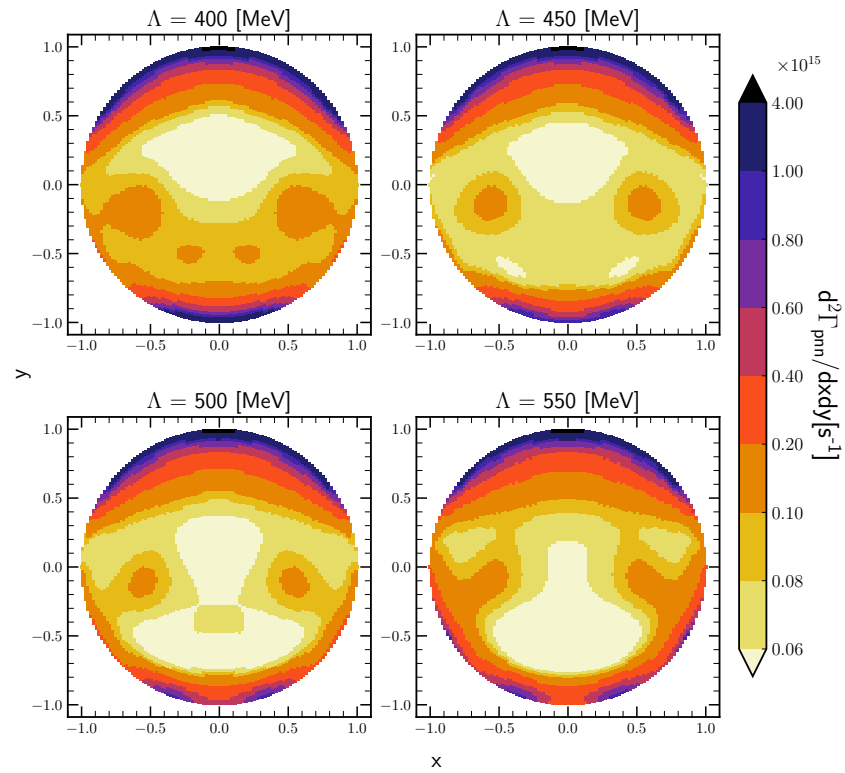


Figure 3.48: The same as in Fig. 3.47 but for the double differential absorption rates $d^2\Gamma_{pnn}/dx dy$.

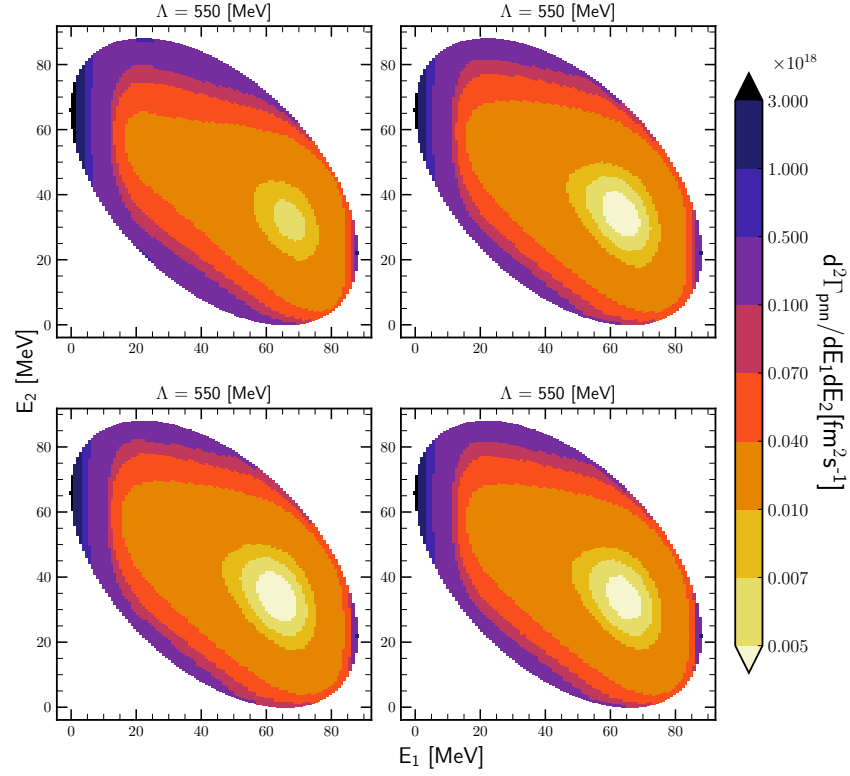


Figure 3.49: Intensity plots for the double differential absorption rates $d^2\Gamma_{pn}/dE_1 dE_2$ for the $\pi^- + {}^3\text{He} \rightarrow p + n + n$ process, obtained using the SMS potential at N^4LO^+ with all contributions possible: plane wave + rescattering, $\text{SN} + 2\text{N}$, $2\text{NF} + 3\text{NF}$. Each panel present predictions obtained with different chiral orders: from N^2LO (upper left) to N^4LO^+ (lower right). Nucleon 1 is a proton.

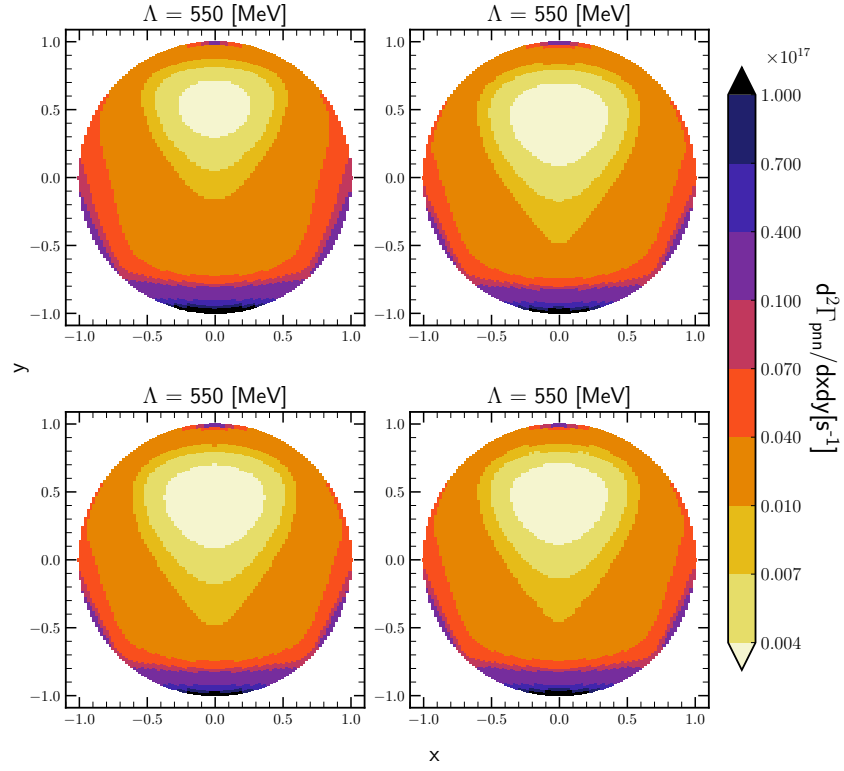


Figure 3.50: The same as in Fig. 3.49 but for the double differential absorption rates $d^2\Gamma_{pnn}/dxdy$.

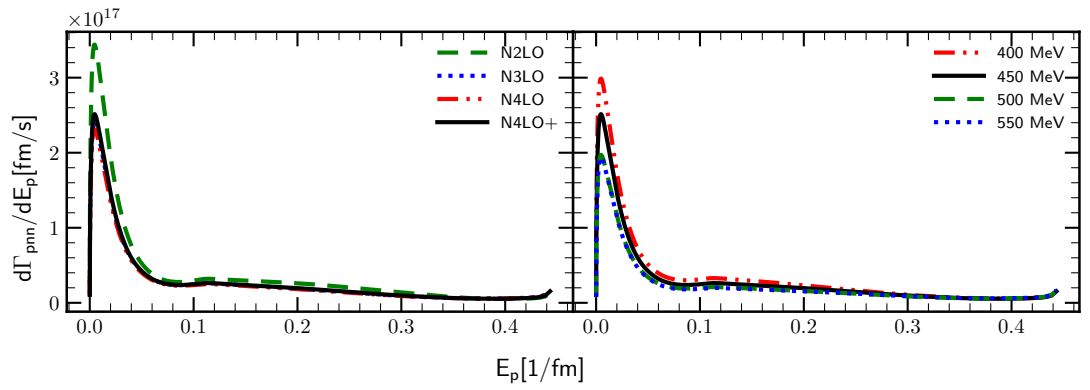


Figure 3.51

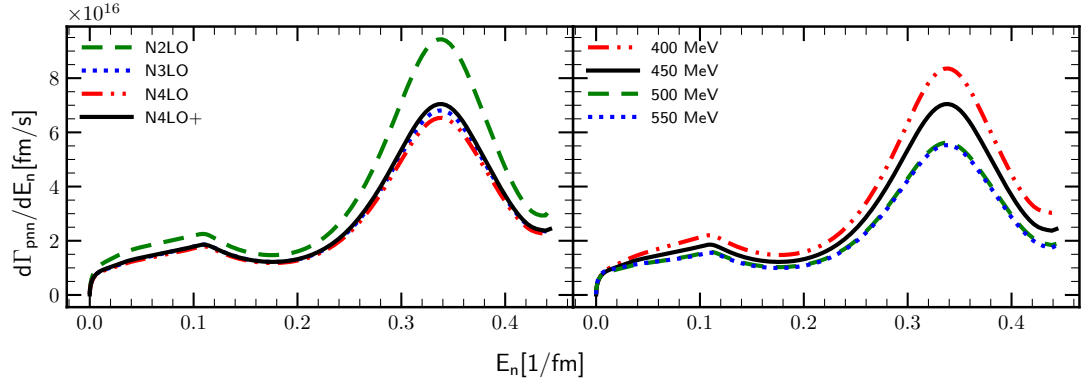


Figure 3.52

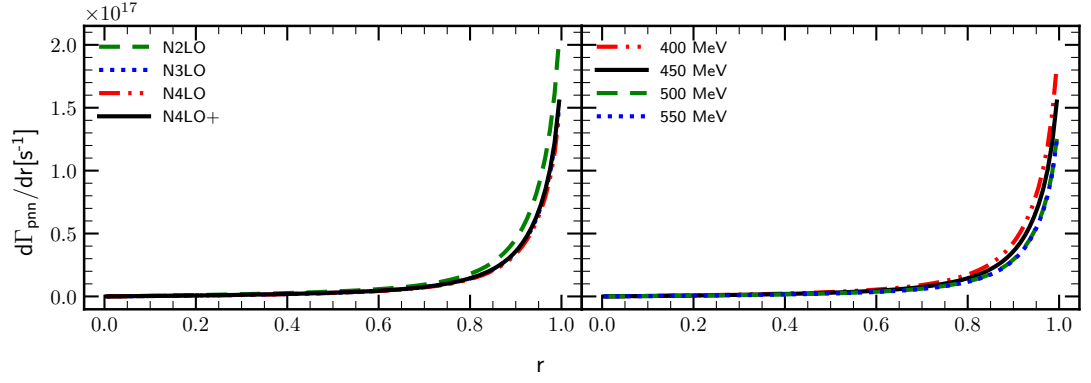


Figure 3.53

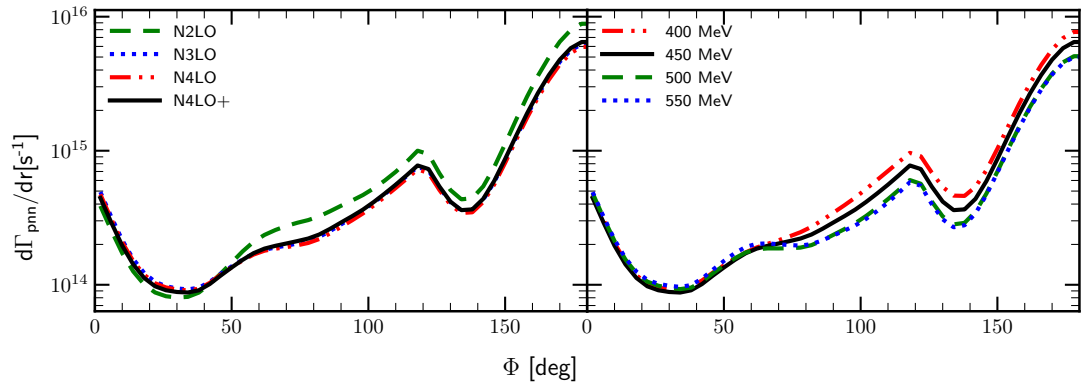


Figure 3.54

3.3.2 $\pi^- + {}^3\text{H} \rightarrow n + n + n$

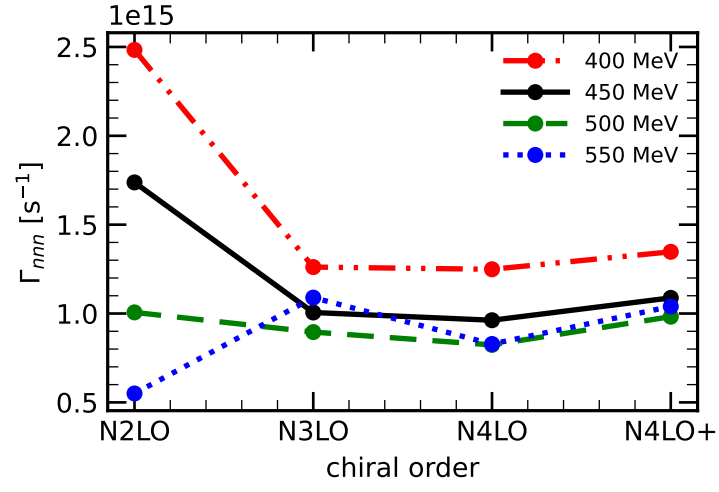


Figure 3.55

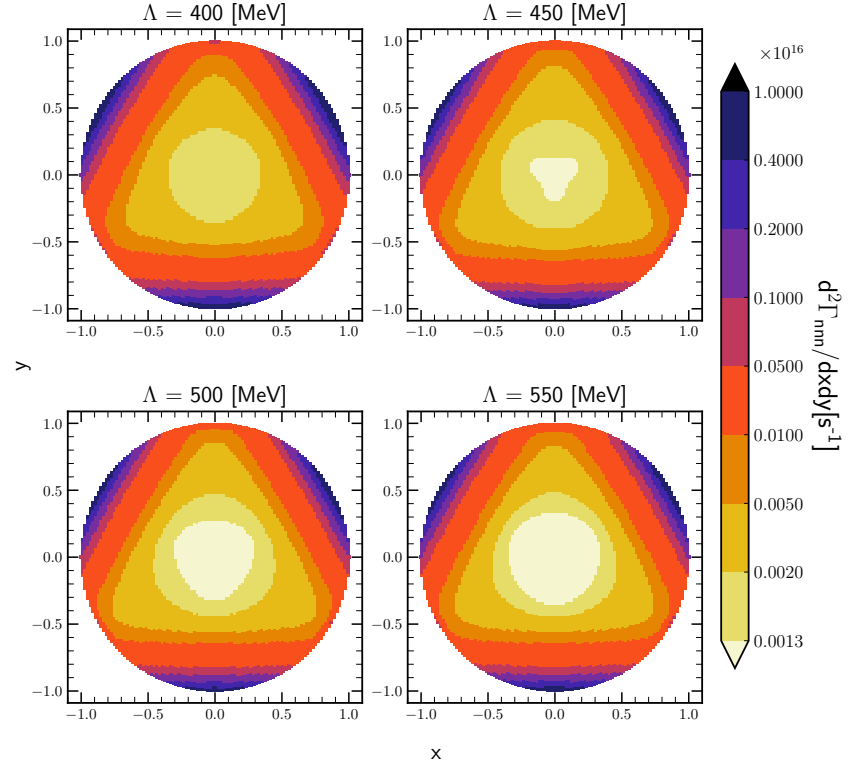


Figure 3.56

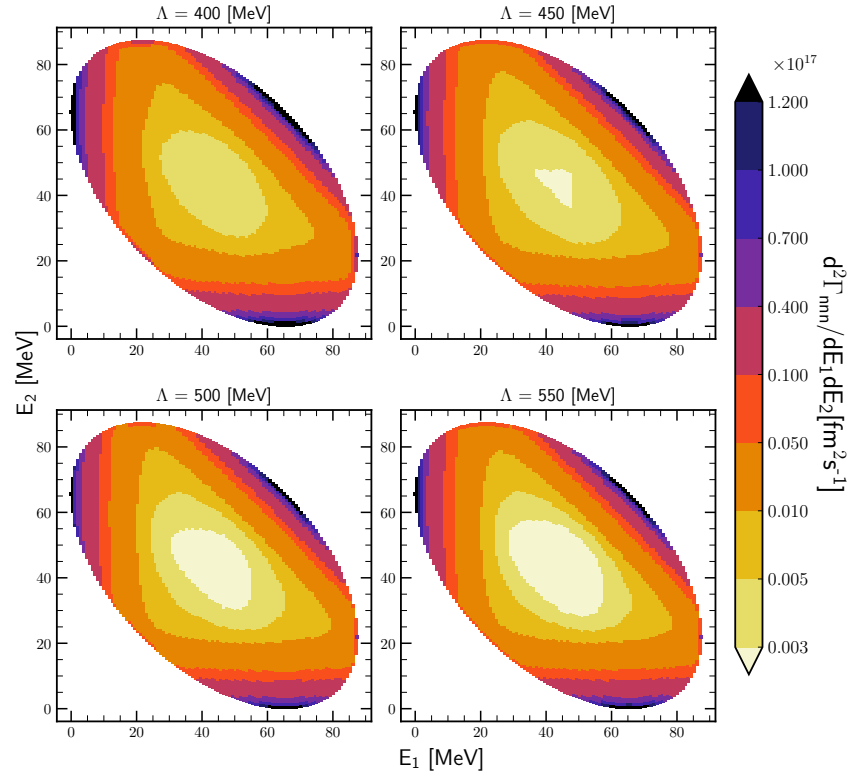


Figure 3.57

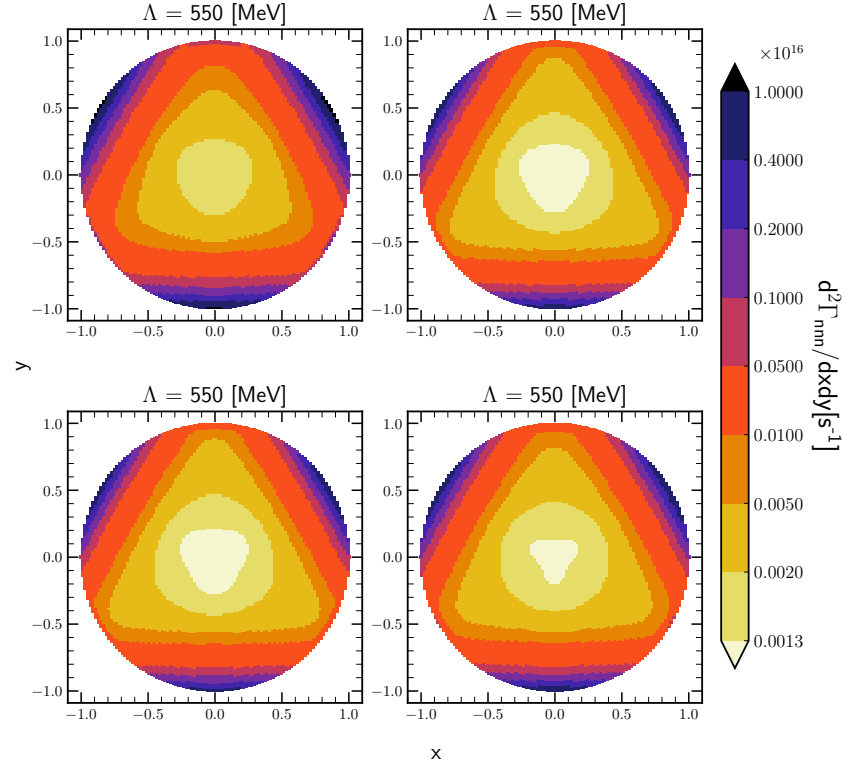


Figure 3.58

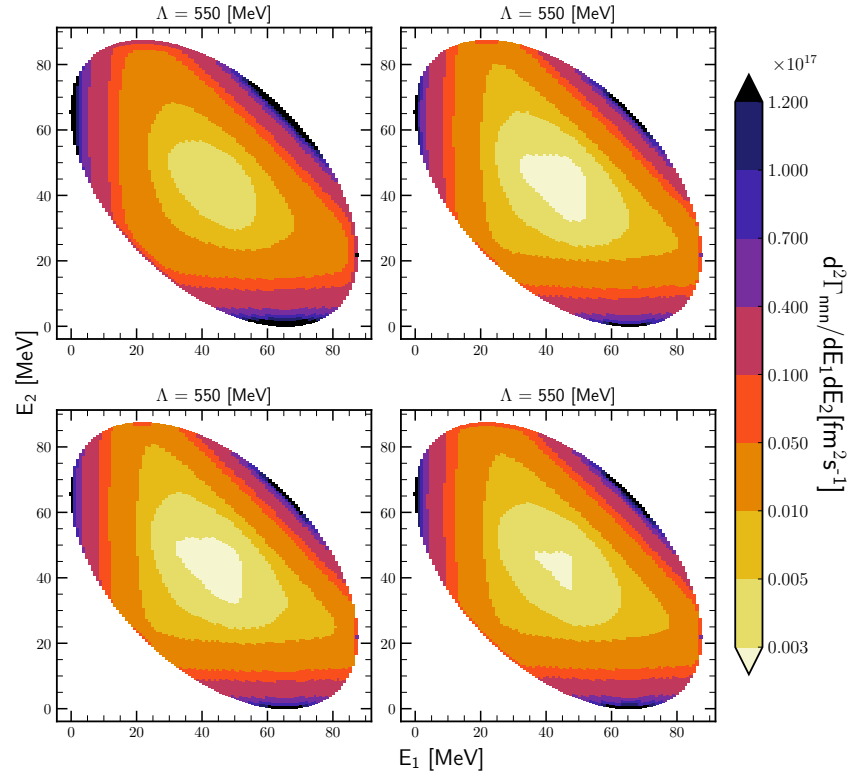


Figure 3.59

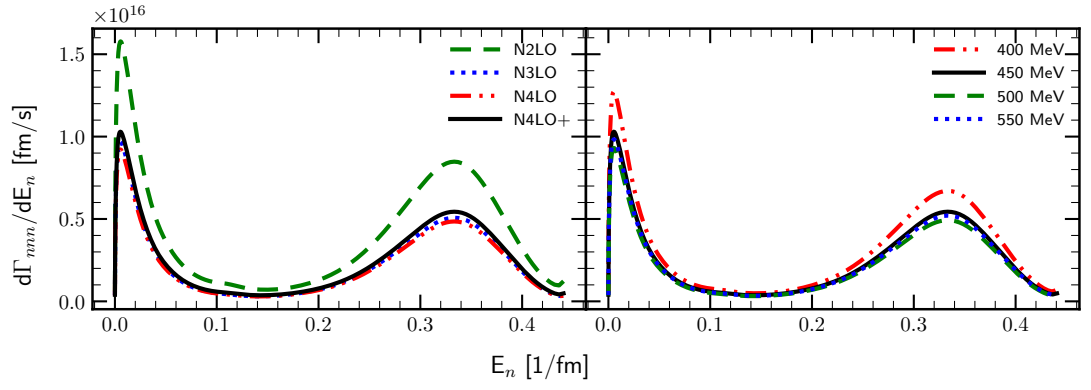


Figure 3.60

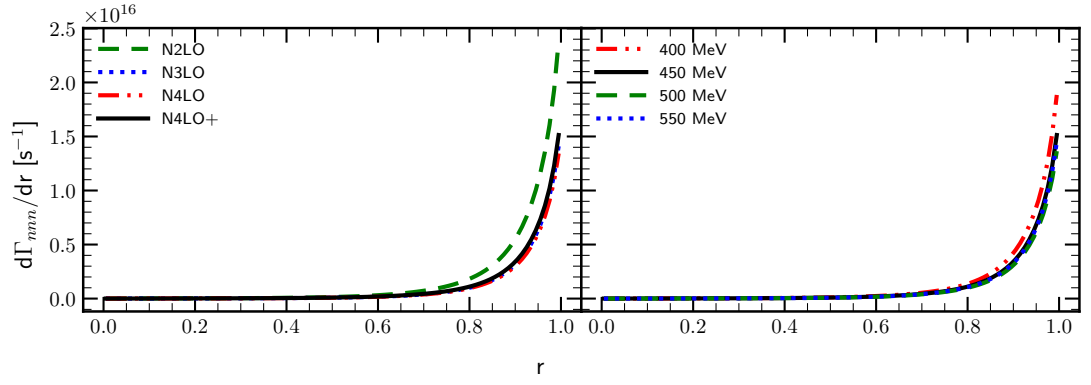


Figure 3.61

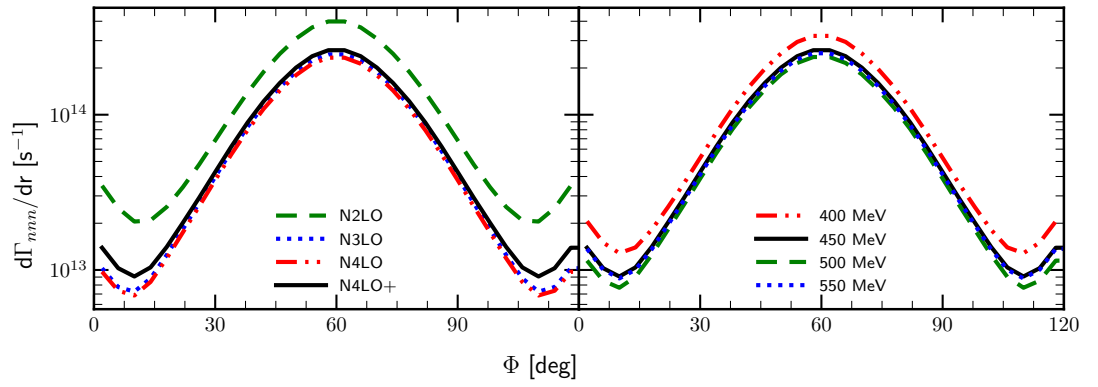


Figure 3.62